A STM Study of the Self-Assembly Phenomenon and Mechanism of Cobalt-C_{60} Clusters on Au(111) Surfaces

By Haoyu Zhao

A thesis submitted to The University of Birmingham for the degree of Doctor of Philosophy

Nanoscale Physics Research Laboratory

School of Physics and Astronomy

University of Birmingham

February 2023

Abstract

In 2013, Self-assembled Au-C_{60} magic number clusters on Au (111) surfaces were successfully manufactured by the NPRL laboratory of the University of Birmingham. This work has important significance for the surface self-assembly of carbon nanostructures. However, this work has two key issues that can't be solved: the Au cluster is too stable to be characterized and can't expect further structure evolution. So, in the further work, the similar cobalt-C_{60} clusters were attempted to be prepared. However, the C_{60} on Au (111) substrate show the phase separation although the interaction between cobalt and C_{60} is much stronger than gold and C_{60}. In this thesis, a reasonable explanation for the formation mechanism of Cobalt-C_{60} clusters is given based on the STM technique.

Due to the 14% lattice mismatch between cobalt and gold, the cobalt clusters on Au (111) are irregular and rugged. Therefore, although the cobalt atoms have a good affinity for C_{60}, the cobalt clusters on the gold surface cannot form Cobalt-C_{60} clusters, due to inefficient contact with C_{60}. Only at high temperature, the thermal motion of cobalt atoms is enhanced. Cobalt atoms refine themselves to be in complete contact with C_{60} molecules, thus adsorbing C_{60} to form Cobalt-C_{60} clusters. As cobalt clusters at high temperature will gradually sink into the gold surface, if the order of annealing and C_{60} deposition is exchanged, the pre-annealed cobalt clusters will partially sink into the gold surface resulting in a lack of C_{60} adsorption sites. So, the Cobalt-C_{60} clusters will not be able to form. In a common heating treatment for both, cobalt cluster will be wrapped by C_{60} molecules in advance to prevent it from sinking. Further experimental evidences suggest that the opening of the carbon cage and the formation of the cobalt-carbon bond may also have occurred at higher temperatures.

Abbreviation

AES	Auger electron spectroscopy
CPC	Connector Plate Cryostat
DLs	Discommensuration Lines
EELS	Electron-Energy-Loss Spectroscopy
FCC	Face Centered Cubic
FEL	Fast Entry Lock
FFT	Fast Fourier transform
HAS	Helium Atom Scattering
HCP	Hexagonal Closed Packed
HOMO	Highest Occupied Molecular Orbitals
HOPG	Highly Oriented Pyrolytic Graphite
HRHAS	High Resolution Helium Atom Scattering
K cell	Knudsen Cells
LDOS	Local Density of State
LEED	Low Energy Electron Diffraction
LM	Lateral Manipulation
LUMO	Lowest Unoccupied Molecular Orbitals
MEIS	Medium energy ion scattering
ML	Monolayer
MoS_2	Molybdenum Disulfide
PBN	Pyrolytic Boron Nitride
PVD	Physics Vapor Deposition
RHEED	Reflection High Energy Electron Diffraction
RT	Room Temperature
SC	Simple Cubic
SP-STM	Spin-polarized scanning tunneling microscopy
SQUID	Superconducting Quantum Interference Device
STM	Scanning Tunnelling Microscopy

STS	Scanning Tunneling Spectroscopy
TEAS	Thermal Energy Helium-Atom Scattering
TEM	Transmission Electron Microscopy
TSP	Titanium Sublimation Pump
UHV	Ultra-High Vacuum
UPS	Ultraviolet photoelectron spectroscopy
VM	Vertical Manipulation
VT-STM	Variable Temperature Scanning Tunnelling Microscopy
XPS	X-ray photoelectron spectroscopy
XRD	X-Ray Diffraction

Acknowledgement

I would like to express my deepest gratitude to all those who have helped and supported me during my PhD studies. Firstly, I would like to express my sincere gratitude to my supervisor, Dr Quanmin Guo. I would like to thank him for providing me with the opportunity to research two-dimensional nanomaterials science for my PhD studies. I have benefited greatly from his extensive experience and understanding of physical experiments, his keen intuition of physical phenomena, and his foresight in choosing topics. Without his guidance and assistance, I would not have been able to complete my PhD. I would also like to express my gratitude to my second supervisor, Dr Wolfgang Theis, whose guidance and assistance have also greatly help to me in my PhD studies. I would also like to express my sincere gratitude to Dr. Yitao Wang, without his unfailing help with high vacuum technology, STM equipment, NPRL laboratory's operations and knowledge of 2D nanomaterials, I would not have been able to reach the level of competence required for my PhD in such a short time as a newcomer in the field. His support has been an important part of my ability to complete my PhD. I would also like to thank Mr. Haoxuan Ding for all the help he has given me about living in the UK, which has been a great help to me as a first-time international student abroad, as well as Ms. Megan Grose, Mr. Chunqiu Xia, Ms. Hualin Yang, Mr. Bosheng Li and Ms. Ying Gao from the NPRL lab, who have all been of great help to me in my PhD studies and campus life at the University of Birmingham.

I would also like to thank Ms. Qun Luo in London, who welcomed me on my first day in the UK and whose help I will never forget. I would also like to thank my housemate and friend, Mr. Rui Mei, for his help in my life and our friendship, which I will always remember. I would also like to thank my friends in China, Mr. Jianze Li, Mr. Zijian Zhang, Mr. Han Li, Mr. Puxuan Ning, Mr. Rui Li, Mr. Junan Mou and the friends I have made through the internet: the " Monogatari Circle ". During the hard times when I lacked social life due to the Covid-19 pandemic, it was your

communication with me through the internet that soothed my lonely soul.

Finally, I need to express my greatest gratitude to my parents. They have supported me in every way, not only financially and materially, but also spiritually. Their encouragement, trust and love have seen me through many difficult times. They are always the one who support and love me the most, and the ones I want to thank the most.

Publications

Ding, H., Gao, J., **Zhao, H.**, Xia, C., Grose, M., Li, F. S., & Guo, Q. (2020). Perturbational Imaging of Molecules with the Scanning Tunneling Microscope. *The Journal of Physical Chemistry C*, *124*(47), 25892-25897.

Contents

Chapter 1. Introduction

Since Gerd Binnig and Heinrich Rohrer invented the Scanning Tunneling Microscopy (STM) in 1981 at IBM Zürich [1], scientists have got a powerful tool to observe the atomic scale structure of surfaces with real space imaging. STM also provides a chance to manipulate molecules as well as atoms. Therein, the first and most famous instance is the "IBM" written by the IBM scientists using 35 individual xenon atoms on a substrate of nickel [2]. However, the atom manipulator technique is not always as simple as it looks. When we want to get a larger and more complex structure, the atom manipulator technique will show its limitation. Because of that, scientists want to find some more efficient techniques to cope with possible mass production. What's more, with the high-speed development of chips, the need for atomic scale electrical components is becoming more and more urgent. Since that, self-assembly technique which can manufacture nanostructures in bulk receives a lot of attention. Applying the self-assembly technique, scientists have successfully prepared nanoscale electrical components like field-effect transistors (FET) based on the ZnO network [3] or Single Electron Transistors (SET) [4].

Au (111) surface has been intensively studied by STM [5-8]. Because of its inertness and easily accessible large-area atomically flat surface, the Au (111) surface is a frequently used metal substrate in UHV-STM systems [9-19]. At the same time, the $22\times\sqrt{3}$ reconstructions of Au (111), especially the elbow sites, provide important adsorption sites for molecules [20]. Therefore, the Au (111) surface has become a commonly used substrate in surface physics and STM research.

Fullerene is a typical carbon atom nanostructure and C_{60} molecule is one of the earliest discovered and the most famous one. The band gap of C_{60} molecule is 1.6 eV [21], which is semiconductive. However, due to the complexity of the crystal structure, the actual band gap of solid C_{60} is higher than the theoretical value, probably around 2.3eV. [22][23] Even so, C_{60} still receive attention as a new type of semiconductor

material. For example, there have been some researches about the applications of C_{60} in inorganic solar cells. [24] Therefore, the various properties of thin film C_{60} have been extensively investigated. [9-12][25][26] In these, as the only FCC (111) surface with a reconstruction, the growth of C_{60} on the Au (111) surface is an important branch. What's more, the combination of fullerene and metal atoms, including endohedral fullerene [27] (atoms are wrapped within the fullerene cage), exohedral fullerene [28] (atoms are linked at the outer side of the fullerene cage) and hetero fullerene [29] (fullerene with carbon atoms replaced by other atoms) have been widely studied. Metallofullerene derivatives play an important role in nonlinear optics [30], thin-film photovoltaic materials [24], molecular magnetic switches [31], etc. Meanwhile, the deposition of metals on the Au (111) surface, especially the clustering of metals around the elbow sites, has also been studied a lot [13-16]. Based on these backgrounds, metal-C_{60} complexes on Au (111) surfaces have become a worthwhile subject of research.

The self-assembly magic number $(C_{60})_m$-$(Au)_n$ complexes on Au(111) surfaces have been observed since 2013 by the Nanophysics Research Laboratory (NPRL) at the University of Birmingham. [17] Similarly, magic number $(C_{70})_m$–$(Au)_n$ clusters can also be manufactured on Au(111) substrates.[18] This metal-fullerene complex exhibits good self-stability below 400 K [19][32] and can realize the self-assembly transformation from high magic number to low magic number by probe manipulation [33]. Meanwhile, because of the lower symmetry of the C_{70} molecule than the C_{60} molecule, the small-scale $(C_{70})_m$–$(Au)_n$ clusters also undergo spontaneous Stick-Sudden-Rotation at room temperature. [18] However, due to the extremely stable chemical property of gold, it is difficult to expect more structure evolution of gold-fullerene complexes. Therefore, people turned their attention to other metals in anticipation of obtaining metal-fullerene complexes where the metal involved is more reactive than gold.

As a member of ferromagnetic metals, cobalt is more reactive than gold. The binding between cobalt and C_{60} molecules has been studied in many articles, including Cobalt-C_{60} units [34-36], C_{60} molecules doped with cobalt [37], and C_{60} cages encapsulating cobalt atoms [38]. In addition to this, there are also studies reporting on the evolution of the C_{60} molecular structure evolution catalyzed by cobalt. [39] These articles reveal the affinity of cobalt atoms with C_{60} and demonstrate the feasibility of cobalt atoms to catalyze the structure evolution of C_{60}, which compensates for the lack of subsequent structure evolution of gold-C_{60} clusters. These evidences provide supports for the necessity of cobalt-C_{60} cluster preparation. At the same time, due to its magnetic properties, it can be well measured by techniques such as SP-STM [40][41], which is sensitive to magnetic field information and compatible with STM. This provides a characterization method for metal clusters covered by C_{60} molecules which is not possible for Au-C_{60} clusters. Both the studies of electron transfer between C_{60} and cobalt thin film [26] and the cobalt-catalyzed C_{60} structure evolution [39][42] show that the self-assembly of Cobalt-C_{60} complexes is worth looking into.

In this thesis, the research on Cobalt-C_{60} self-assembly clusters on Au (111) surfaces will be presented. In experiments, it has been found that if C_{60} molecules are deposited on an untreated Co/Au (111) sample, the C_{60} molecules will prefer to form large C_{60} islands rather than bond to the cobalt clusters. When this sample is annealed at 320 °C for half an hour, the C_{60} islands will disappear and all the C_{60} molecules will be adsorbed by the cobalt clusters, forming Cobalt-C_{60} clusters. The question then is, why is cobalt at room temperature not a C_{60} adsorbing site and what role does annealing play in the self-assembly of the Cobalt-C_{60} cluster? In this thesis, several models are presented to explain this phenomenon and design further experiments to test these conjectures. Further, if anneal the cobalt clusters firstly and deposit the C_{60} molecules after that, different results are observed in the experiments. Pre-annealing did not assist the formation of Cobalt-C_{60} clusters, while C_{60} still form large C_{60} islands. In contrast, for the pre-annealed Co-C_{60}/Au (111) sample, even annealing it

again at 320 °C or above, there are no similar Cobalt-C_{60} clusters founded. These indicate that annealing causes multiple effects on the sample, including thermal motion of the cobalt clusters at high temperature, sinking of the cobalt clusters into the gold surface, diffusion of C_{60} molecules and the formation of cobalt-carbon bonds between cobalt and C_{60}. The self-assembly of the Cobalt-C_{60} cluster is shaped by the mutual balance of these different effects.

Chapter 2 will review the relevant literatures and research background in detail, including the quantum tunneling effect, STM technology and atomic manipulation technology. It will also include surface reconstructions and related properties of Au (111) surfaces. There are also the properties of metal cobalt and C_{60} molecules, the behavior of cobalt on metal surfaces, and the interaction and structure evolution between cobalt and C_{60}.

Chapter 3 will introduce the various experimental equipment and techniques used in this experiment, represented by the STM system. This will include VT-STM equipment, ultra-high vacuum technology and its realization, manufacturing of Au (111) substrates, electrochemical etching of STM probes, and cleaning of both in the UHV-STM chamber, as well as the in-situ deposition of cobalt and C_{60}.

Chapter 4 exhibits experimental results of the self-assembly Cobalt-C_{60} clusters. It includes the structure of the cobalt clusters on the Au (111) surface and the arrangement of C_{60} molecules on the Co/Au (111) surface. The C_{60} molecules form islands independently with the small cobalt clusters show a phase separation to C_{60}. Only large-size cobalt clusters adsorb some single C_{60} molecules. After annealing at 320 °C for 30 minutes, the disappearance of the large C_{60} islands and the formation of Co-C_{60} clusters are observed. In this chapter, the reproducibility and stability of this self-assembly structure are demonstrated with repeated experiments. At the end of this chapter, I will analyze these phenomena and suggest several possible models to

explain them.

Chapter 5 will focus on the effect of annealing on the Cobalt-C_{60} clusters self-assembly. The evolution of the cobalt clusters with temperature can be seen through the segmented annealing of Co/Au (111) sample. At temperature below 200 °C, the cobalt clusters change from disordered to flattened bilayer clusters. Whereas at temperature above 200 °C, a gradual decrease of the surface cobalt coverage can be seen. Considering that 320 °C is not sufficient to desorb the cobalt atoms, it is believable that the cobalt clusters sink into the surface of the gold. Then, after depositing C_{60} on the sample that was pre-annealed at 320 °C, it can be seen that the Co-C_{60} clusters do not appear on it. Even until it is re-annealed to 320 °C or above, there are still no expected clusters found on the surface. At 380 °C, the binding of individual C_{60} to cobalt clusters can be observed as well as the diffusion of cobalt clusters and the collapse of the edges of C_{60} islands. By comparing these experimental results obtained in this chapter with the contents of Chapter 4, various models proposed in Chapter 4 are considered and get the final explanation. Due to the lattice mismatch between gold and cobalt, the cobalt clusters on the gold surface at room temperature are irregular, and this irregularity greatly reduces the C_{60} adsorption capacity of the cobalt clusters. In annealing, the thermal motion of the cobalt clusters enhances the C_{60} adsorption capacity. Then, at higher temperature, chemical bonds are formed between the cobalt and C_{60} molecules, resulting in the formation of stable Cobalt-C_{60} clusters. For pre-annealed samples, almost all of the cobalt clusters sink into the Au (111) surface due to the lack of protection for the C_{60} molecules, which greatly reduces the adsorption capacity for the C_{60} molecules. Therefore, the C_{60} molecules can only be adsorbed through Co-C bond at high temperature.

Chapter 6 will provide some conjectural explanations for some parts of the above chapters which have not been well explained. Due to the limited time available for the experiments, these conjectures have not been experimentally verified. In Chapter 6,

there will be some experiment designs to test these conjectures based on the available experimental conditions and make predictions about the experimental results. The conjectures will include the specific mechanism of how annealing enhances the C_{60} adsorption capacity of cobalt clusters, the multiple adsorption effects of cobalt clusters on C_{60}, the protection of sinking cobalt clusters by C_{60} molecules and the migration of cobalt clusters.

Chapter 7 gives an overall summary of the research conducted and suggests possible future work.

References

[1] Scanning Tunneling Microscopy—Methods and Variations. In *Scanning Tunneling Microscopy and Related Methods* (pp. 1-25). Springer, Dordrecht.

[2] "IBM's 35 atoms and the rise of nanotech". *https://www.cnet.com/news/ibms-35-atoms-and-the-rise-of-nanotech/*

[3] Zhenqing, D., Changxin, C., Yaozhong, Z., Liangming, W., Jing, Z., Dong, X., & Yafei, Z. (2012). ZnO nanowire network transistors based on a self-assembly method. *Journal of Semiconductors*, *33*(8), 084003-6.

[4] Feldheim, D., & Keating, C. (1998). Self-assembly of single electron transistors and related devices. *Chemical Society Reviews, 27*(1), 1-12.

[5] Barth, J. V., Brune, H., Ertl, G., & Behm, R. J. (1990). Scanning tunneling microscopy observations on the reconstructed Au (111) surface: Atomic structure, long-range superstructure, rotational domains, and surface defects. *Physical Review B*, *42*(15), 9307.

[6] Wöll, C., Chiang, S., Wilson, R. J., & Lippel, P. H. (1989). Determination of atom positions at stacking-fault dislocations on Au (111) by scanning tunneling microscopy. *Physical Review B*, *39*(11), 7988.

[7] Narasimhan, S., & Vanderbilt, D. (1992). Elastic stress domains and the herringbone reconstruction on Au (111). *Physical review letters*, *69*(10), 1564.

[8] Takeuchi, N., Chan, C. T., & Ho, K. M. (1991). Au (111): A theoretical study of the surface reconstruction and the surface electronic structure. *Physical Review B*, *43*(17), 13899.

[9] Altman, E. I., & Colton, R. J. (1994). Interaction of C60 with the Au (111) $23\times\sqrt{3}$ reconstruction. *Journal of Vacuum Science & Technology B: Microelectronics and Nanometer Structures Processing, Measurement, and Phenomena*, *12*(3), 1906-1909.

[10] Gardener, J. A., Briggs, G. A. D., & Castell, M. R. (2009). Scanning tunneling microscopy studies of c 60 monolayers on au (111). *Physical Review B*, *80*(23), 235434.

[11] Shin, H., Schwarze, A., Diehl, R. D., Pussi, K., Colombier, A., Gaudry, É., ... & Berndt, R. (2014). Structure and dynamics of C 60 molecules on Au (111). *Physical Review B*, *89*(24), 245428.

[12] Guo, S., Fogarty, D. P., Nagel, P. M., & Kandel, S. A. (2004). Thermal diffusion of C_{60} molecules and clusters on Au (111). *The Journal of Physical Chemistry B*, *108*(37), 14074-14081.

[13] Chambliss, D. D., Wilson, R. J., & Chiang, S. (1991). Nucleation of ordered Ni island arrays on Au (111) by surface-lattice dislocations. *Physical review letters*, *66*(13), 1721.

[14] Voigtländer, B., Meyer, G., & Amer, N. M. (1991). Epitaxial growth of thin magnetic cobalt films on Au (111) studied by scanning tunneling microscopy. *Physical Review B*, *44*(18), 10354.

[15] To, C., Zeppenfeld, P., Krzyzowski, M. A., David, R., & Comsa, G. (1997). Growth and stability of cobalt nanostructures on gold (111). *Surface science*, *394*(1-3), 170-184.

[16] *Hou, Q., Hou, M., Bardotti, L., Prével, B., Mélinon, P., & Perez, A. (2000). Deposition of Au_N clusters on Au (111) surfaces. I. Atomic-scale modeling. Physical Review B, 62(4), 2825.*

[17] Xie, Y. C., Tang, L., & Guo, Q. (2013). Cooperative assembly of magic number C 60-Au complexes. *Physical Review Letters, 111*(18), 186101.

[18] Wang, Y., Kaya, D., Gao, J., & Guo, Q. (2019). Stick-Sudden-Rotation and Structural Polymorphism of (C_{70}) m–(Au) n Hybrid Nanoclusters. *The Journal of Physical Chemistry*

C, 123(20), 12791-12796.
[19] Rokni-Fard, M., & Guo, Q. (2019). Stability of $(C_{60})_m$–Au $_n$ Magic Number Clusters. *The Journal of Physical Chemistry C, 123*(30), 18482-18487.
[20] Meyer, J. A., Baikie, I. D., Kopatzki, E., & Behm, R. J. (1996). Preferential island nucleation at the elbows of the Au (111) herringbone reconstruction through place exchange. *Surface science*, *365*(1), L647-L651.
[21] Saito, S., & Oshiyama, A. (1991). Cohesive mechanism and energy bands of solid C 60. *Physical Review Letters*, *66*(20), 2637.
[22] Lof, R. W., van Veenendaal, M. V., Koopmans, B., Jonkman, H. T., & Sawatzky, G. A. (1992). Band gap, excitons, and Coulomb interaction in solid C 60. *Physical review letters*, *68*(26), 3924.
[23] Mishori, B., Katz, E. A., Faiman, D., & Shapira, Y. (1997). Studies of electron structure of C60 thin films by surface photovoltage spectroscopy. *Solid state communications*, *102*(6), 489-492.
[24] Katz, E. A. (2006). Fullerene thin films as photovoltaic material. In *Nanostructured materials for solar energy conversion* (pp. 361-443). Elsevier.
[25] Klitgaard, S. K., Egeblad, K., Haahr, L. T., Hansen, M. K., Hansen, D., Svagin, J., & Christensen, C. H. (2007). Self-assembly of C60 into highly ordered chain-like structures on HOPG observed at ambient conditions. *Surface science*, *601*(9), L35-L38.
[26] Kollamana, J., Wei, Z., Laux, M., Stöckl, J., Stadtmüller, B., Cinchetti, M., & Aeschlimann, M. (2016). Scanning tunneling microscopy study of ordered C_{60} submonolayer films on Co/Au (111). *The Journal of Physical Chemistry C, 120*(14), 7568-7574.
[27] Shinohara, H., Takata, M., Sakata, M., Hashizume, T., & Sakurai, T. (1996). Metallofullerenes: their formation and characterization. In *Materials Science Forum* (Vol. 232, pp. 207-232). Trans Tech Publications Ltd.
[28] Wang, Y., Díaz-Tendero, S., Alcami, M., & Martin, F. (2017). Relative stability of empty exohedral fullerenes: π delocalization versus strain and steric hindrance. *Journal of the American Chemical Society*, *139*(4), 1609-1617.
[29] Hirsch, A., & Vostrowsky, O. (2001). C_{60} hexakisadducts with an octahedral addition pattern−a new structure motif in organic chemistry. *European Journal of Organic Chemistry*, *2001*(5), 829-848.
[30] Mateo-Alonso, A., Iliopoulos, K., Couris, S., & Prato, M. (2008). Efficient modulation of the third order nonlinear optical properties of fullerene derivatives. *Journal of the American Chemical Society*, *130*(5), 1534-1535.
[31] López-Moreno, A., & del Carmen Giménez-López, M. (2021). Metallic-based magnetic switches under confinement. In *Advances in Organometallic Chemistry* (Vol. 75, pp. 149-191). Academic Press.
[32] Kaya, D., Gao, J., Fard, M. R., Palmer, R. E., & Guo, Q. (2018). Controlled Manipulation of Magic Number Gold–Fullerene Clusters Using Scanning Tunneling Microscopy. *Langmuir, 34*(28), 8388-8392.
[33] Kaya, D., Bao, D., Palmer, R. E., Du, S., & Guo, Q. (2017). Tip-triggered thermal cascade manipulation of magic number gold–fullerene clusters in the scanning tunnelling microscope. *Nano Letters, 17*(10), 6171-6176.
[34] Kurikawa, T., Nagao, S., Miyajima, K., Nakajima, A., & Kaya, K. (1998). Formation of Cobalt− C_{60} Clusters: Tricapped Co (C_{60}) 3 Unit. *The Journal of Physical Chemistry A, 102*(10),

1743-1747.
[35] Avramov, P., Naramoto, H., Sakai, S., Narumi, K., Lavrentiev, V., & Maeda, Y. (2007). Quantum Chemical Study of Atomic Structure Evolution of Co x/C_{60} (x≤ 2.8) Composites. *The Journal of Physical Chemistry A, 111*(12), 2299-2306.
[36] Nagao, S., Kurikawa, T., Miyajima, K., Nakajima, A., & Kaya, K. (1998). Formation and Structures of Transition Metal− C_{60} Clusters. *The Journal of Physical Chemistry A, 102*(24), 4495-4500.
[37] Moorsom, T., Wheeler, M., Khan, T. M., Al Ma'Mari, F., Kinane, C., Langridge, S., ... & Cespedes, O. (2014). Spin-polarized electron transfer in ferromagnet/C_{60} interfaces. *Physical Review B, 90*(12), 125311.
[38] Javan, M. B., Tajabor, N., Rezaee-Roknabadi, M., & Behdani, M. (2011). First principles study of small cobalt clusters encapsulated in C_{60} and C82 spherical nanocages. *Applied surface science, 257*(17), 7586-7591.
[39] Lavrentiev, V., Naramoto, H., Abe, H., Yamamoto, S., Narumi, K., & Sakai, S. (2005). Chemically driven microstructure evolution in cobalt–fullerene mixed system. *Fullerenes, Nanotubes and Carbon Nanostructures, 12*(1-2), 519-528.
[40] Park, J., Park, C., Yoon, M., & Li, A. P. (2017). Surface magnetism of cobalt nanoislands controlled by atomic hydrogen. *Nano letters, 17*(1), 292-298.
[41] Decker, R., Brede, J., Atodiresei, N., Caciuc, V., Blügel, S., & Wiesendanger, R. (2013). Atomic-scale magnetism of cobalt-intercalated graphene. *Physical Review B, 87*(4), 041403.
[42] Sakai, S., Naramoto, H., Lavrentiev, V., Narumi, K., Maekawa, M., Kawasuso, A., ... & Baba, Y. (2005). Polymeric Co-C_{60} compound phase evolved in atomistically mixed thin films. *Materials transactions, 46*(4), 765-768.

Chapter 2. Literature Review

2.1 Scanning Tunneling Microscope

During the human history, the exploration of the micro world never stops. For a long time, Low-Energy Electron Diffraction (LEED), Reflected High-Energy Electron diffraction (RHEED) and X-Ray Diffraction (XRD) are the main methods to observe crystal structures. However, the above-mentioned techniques gather information from a large number of atoms based on the periodic structure of the material. They are not capable of probing local structures such as a single atomic vacancy. In 1981, the breakthrough appeared in IBM Research-Zurich, where Gerd Binnig and Heinrich Rohrer developed the first Scanning Tunneling Microscope (STM) in the world [1].

STM measures the tunneling current between a conductive sample and a metal probe to map the surface topography with atomic resolution. Apart from directly observing the surface structure, STM also has other applications. The atomically precise positioning makes the atom manipulator possible [2] which allows us to prepare some products that are difficult to obtain under normal conditions. Recently, some groups even managed to rotate a single molecule by the STM tip to control its electrical resistance as a molecule switch [3]. What's more, STM can also probe the determination of local density of state (LDOS). Through the determining of LDOS images, STM technique also has an extensive application in the research fields of catalysis and superconductivity.

2.1.1 Quantum Tunneling Effect

The quantum tunneling effect is a typical quantum phenomenon which is not only a thought experiment showing the difference between quantum mechanics and classical physics but an effect with extensive realistic significance and practical applications. It is the key part helping scanning tunneling microscope to realize its high resolution far

beyond optical microscopy.

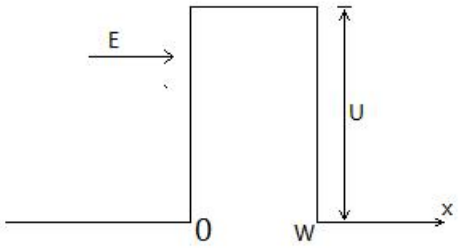

Fig. 2.1 A elementary model of one-dimensional finite height potential barrier. The height of the barrier is U and the width is W. An electron moves towards the barrier with the energy E. The electron's energy E is lower than the barrier's height U.

Fig. 2.1 shows a schematic diagram of a one-dimensional finite height potential barrier. In classical mechanics, if the potential barrier is higher than the energy of an electron, it is impossible for the electron to pass and the electron is totally reflected. However, in quantum mechanics, the wave-like behavior of the electron gives a finite probability that the electron can overcome the barrier. It is a different result with the classical mechanics. Because the energy of the electron is a constant, the electron is in a stationary state that the wave function can be written as $\psi(x,t) = \psi(x)e^{-iEt/\hbar}$, $\hbar$ is the reduced Planck constant. The spatial part of the wave function $\psi(x)$ satisfies the stationary Schrodinger equation.

$$-\frac{\hbar}{2m}\psi'' + V(x)\psi = E\psi \tag{2.1}$$

The $V(x)$ is the potential energy of the barrier as a function of x.

$$V(x) = \begin{cases} U & 0 < x < W \\ 0 & x < 0, x > W \end{cases} \tag{2.2}$$

Inside the barrier, $E < U$,the solution of equation (2.1) is $\psi(x) = \psi(0)e^{-\kappa x}$, in which $\kappa = \frac{\sqrt{2m(U-E)}}{\hbar}$ is real. It means that the wave function between barrier is decays exponentially and the probability of an electron penetrating through the

barrier is:

$$P = |\psi(0)|^2 e^{-2\kappa W} \tag{2.3}$$

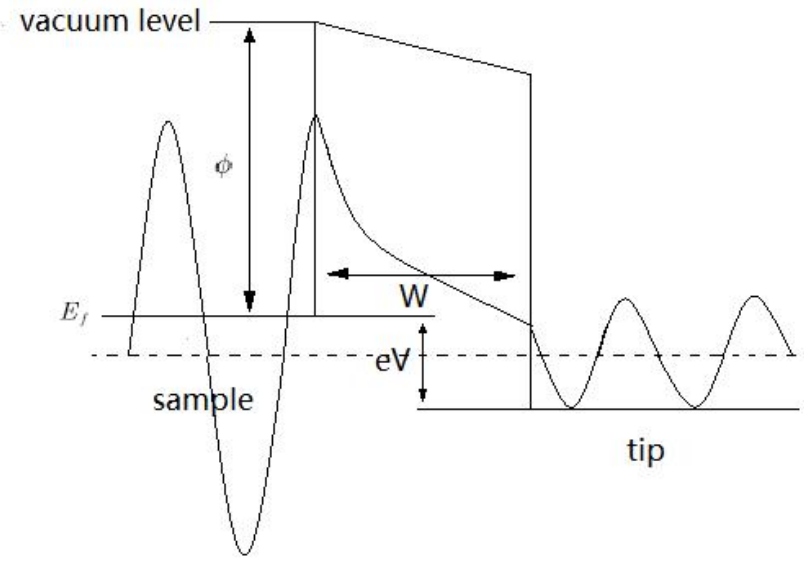

Fig. 2.2 An elementary model of the metal-vacuum-metal tunneling junction of STM. The work function of sample is Φ ,and the width between sample and tip is W. There is a bias V applied to the sample which break the symmetry. The probability of electrons tunneling from tip to sample through vacuum gap is larger than opposite direction and a current flow from sample to tip.

For scanning tunneling microscope, the metal tip and conductive sample build a metal-vacuum-metal tunneling junction which can be simplified to a one-dimensional finite high potential barrier as shown in Fig. 2.2. Here, the height of barrier is the work function Φ and the width of barrier W is equal to the gap between sample and tip. If there is no bias between sample and tip, the electron tunneling will be symmetrical of each direction. When a positive bias V is applied to the sample, the sample and tip's Fermi level will have a difference of eV and the electrons with energy between $E_f - e|V|$ and E_f will tunnel to sample from tip. The average energy of tunneling electron E_n is $E_f - \frac{e|V|}{2}$ and the height of barrier is the $E_f + \Phi$ in which Φ is the work function. So that, the equation (2.3) can be written

in:

$$P = |\psi(0)|^2 \exp\left(-2W\sqrt{\frac{2m}{\hbar^2}\left(\Phi + \frac{e|V|}{2}\right)}\right). \tag{2.4}$$

The electrons tunneling though vacuum gap is from $E_f - e|V|$ to E_f, so the current I from sample to tip has the following pattern:

$$I \propto \sum_{E_f - e|V|}^{E_f} |\psi(0)|^2 \exp\left(-2W\sqrt{\frac{2m}{\hbar^2}\left(\Phi + \frac{e|V|}{2}\right)}\right) \tag{2.5}$$

Which is a sum of electron states between Fermi level in the range eV. The local density of states (LDOS) near energy E [4] is given by

$$\rho(z,E) = \frac{1}{\epsilon}\sum_{E-\epsilon}^{E} |\Psi_n(z)|^2 \tag{2.6}$$

where the ϵ is the sufficiently small quantity of energy around E.

For the STM model, the local density of states near Fermi energy level is

$$\rho(0,E_f) = \frac{1}{eV}\sum_{E-eV}^{E} |\Psi_n(0)|^2 \tag{2.7}$$

where the eV acts as the small quantity ϵ. [4]

In equation (2.5), the exponential component is constant so it can be derived before the summation symbol. The summation part is highly similar in form to equation (2.7) except for a factor relating to the bias voltage V. Thereby, the relationship between tunneling current and bias, Fermi level, vacuum gap can be shown as

$$I \propto V\rho(0,E_f)e^{-2\kappa W} \propto f(V,E_f,W) \tag{2.8}$$

where $\kappa = \frac{\sqrt{2m(\Phi + e|V|)}}{\hbar}$

Although equation (2.8) is a conclusion based on the single-electron model, it is a

quite good approximation. In some models that consider the shape of the probe and the complex structure of the probe and the sample, such as the Bardeen model treating probe and sample as two independent regions [5] and the S-wave tip model that approximates the probe as a single atom on the basis of the Bardeen model [6], the relationship between tunneling current I and height W are still both in accordance with equation (2.8). [4-6]

As can be seen from equation (2.8), when the bias voltage V is determined, the tunneling current I will only be related to the distance W. If the $\Phi + \frac{e|V|}{2}$ is about $5eV$ and the width has a $1\mathring{A}$ difference, the current will have an about 10 times difference. This can be given by a simple calculation.

$$\frac{I'}{I} = \frac{\exp(2\kappa(W+\Delta W))}{\exp(2\kappa W)} = \exp(2\kappa\Delta W) = \exp\left(2\frac{\sqrt{2m_e \cdot 5eV}}{\hbar} \cdot 1\mathring{A}\right) \approx 9.89$$

Therefore, the tunneling current is very sensitive to the change in height which supports STM's $\mathring{A}$ scale resolution.

2.1.2 Two Scanning Modes of STM

In actual operation, the STM system has constant height mode and constant current mode. In constant height mode, the tip's height is stable and the STM measures the structure of surface but current difference. This mode strongly depends on the flatness of the surface so it's not common in experiments. The constant current mode is realized by the control unit which controls the tunneling current as a constant by negative feedback. The tip's movement is controlled by a rectangular piezo drive system (P_x, P_y, P_z) and P_z supports the movement of the tip in the z-axis direction vertical to the sample. By equation (2.8), if the tunneling current is a constant, the distance between tip and sample will always be a constant, so that the tip's height change directly corresponds to the height change of the sample surface. This mode

can keep the tip and sample always in a security distance so it's more common used in experiments.

2.1.3 Atom Manipulator

In STM scanning, the distance between sample surface and tip atoms reaches the nanometer scale to obtain tunneling current. So, the interaction between the surface and the tip atoms can't be ignored at this point. As the tip is constantly moving across the surface during scanning, the interaction between the sample and the tip will also cause perturbations to the surface atoms [7][8]. These perturbations are issues that need to be avoided when people want to obtain clear STM images, but at the same time, these interactions can be used. Thanks to the atomic-scale resolution of the STM probe, it is possible to apply the interaction to a specific atom. On this basis, an STM application called "atomic manipulation" has been developed. From 1986, many experiments relying on atomic manipulation techniques were carried out [9], and in 1990 the first explicit single-atom manipulation experiment was reported [10].

In general, atom manipulation techniques are considered to have two branches: lateral manipulation (LM) as well as vertical manipulation (VM) [11][12]. For lateral manipulation, surface atom is dragged from one position on the surface to another by the tip, while for vertical manipulation, atomic migration occurs between the sample surface and the tip. However, some papers have proposed another manipulation independent of lateral and vertical manipulations [13]. When not individual atom but molecules with internal structures are manipulated, atom manipulation techniques can lead to the evolution of molecular structures, including the dissociation of molecular structures as well as the catalysis of molecular synthesis. [14][15]

Lateral manipulation (LM) was the first atomic manipulation technique to be studied. The first successful lateral manipulation experiment was carried out on the Ni (110) surface by Xe atoms [10]. The main driving force for lateral manipulation is the

extremely distance-sensitive interaction between the surface atom and the tip atoms. The interacting potential between two particles can be expressed by Lennard-Jones potential function which is a semi-empirical formula. As Fig. 2.3, it shows a tendency to fall and then rise. The force between the particles is the derivative of the potential and therefore behaves as a repulsive force at $r<r_m$ and as a gravitational force at $r>r_m$. In the LM, the distance between the surface atom and the tip is kept within the range of mutual attraction. At this point, the wave functions of the two atoms' electrons overlap partially due to their proximity and can thus be seen as a temporary formed chemical bond. For the LM, the atom dragged needs to pass through the surface potential barrier in order to leave its original position under the interaction. At the same time, however, the manipulated atoms cannot completely move away from the surface. So, this requires a high accuracy of interaction strength.

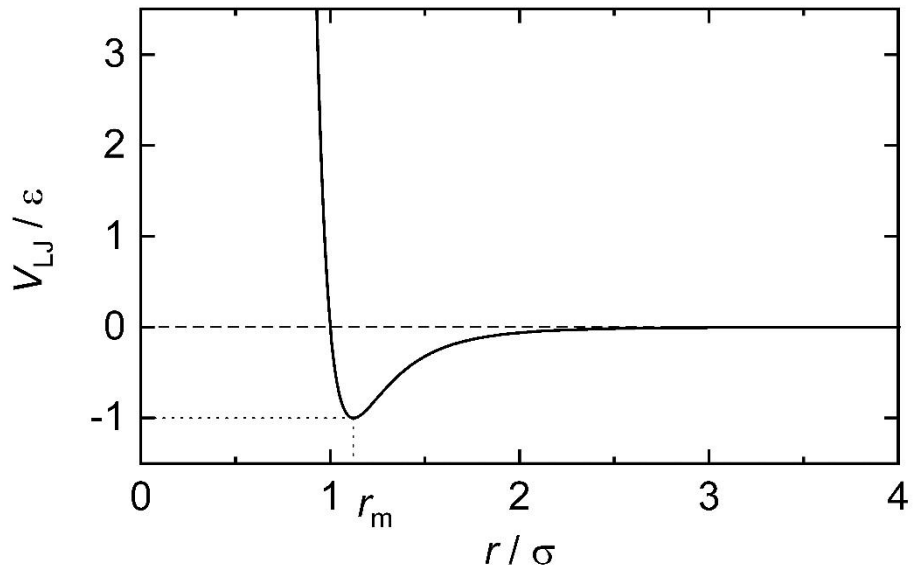

Fig. 2.3 Graph of the Lennard-Jones potential function. The Lennard-Jones potential function is a semi-empirical formula for a neutral interatomic or molecular interaction potential. ε is the depth of the potential well, r is the distance between two interacting particles, and σ is the distance at which the particle-particle potential energy V is zero. [16]

The lateral manipulation has three main steps: 1) Bring the tip close to the sample surface. 2) Drag the tip laterally. 3) Raise the tip back to scanning height. Of these

three steps, step 2 is the most important. The interaction between the surface atom and the tip atoms increases dramatically when the tip is close to the surface, and when the interaction F_L is greater than the surface friction F_S, the surface atom can be dragged. As shown in Fig. 2.4 (b), the interaction between the tip atoms and the surface atom is simplified to the action F_T, and its horizontal component is:

$$F_L = F_T \cos\phi = \frac{dU(r)}{dr}\cos\phi \tag{2.9}$$

Where ϕ is the angle between the direction of interaction F_T and the surface, and U(r) is the Lennard-Jones potential. As the tip moves laterally in constant current mode, the relative distance between the tip and the surface atoms does not change, but the horizontal component F_T gradually increases. When F_T is greater than the frictional force F_S, the surface atom will leave their original position and reach a new point. At this point, the relative distance between the tip atoms and the surface atom changes abruptly, while in constant current mode the tip also jumps abruptly to maintain a constant relative distance for the next lateral dragging.

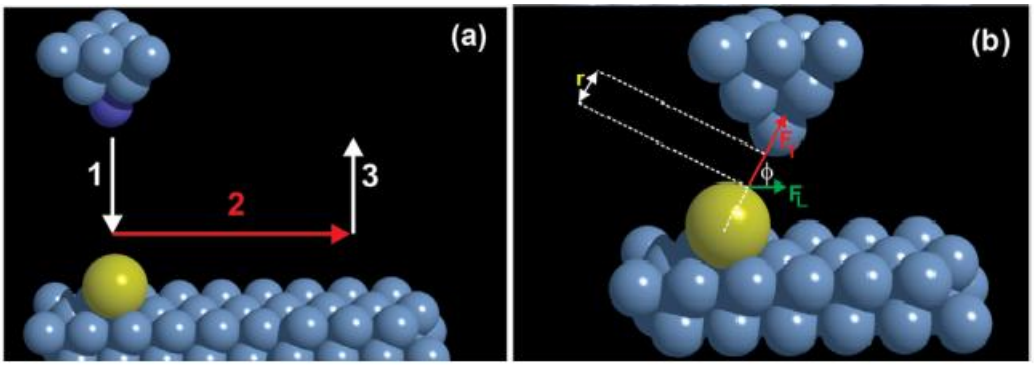

Fig. 2.4 (a) Ball model of LM procedure. The yellow ball is the manipulated atom. (b)Ball model of tip-atom relative position. [14]

In addition, for LM, the dragging route of the atom is also important. If the manipulated atom's size is close to the substrate atoms, the arrangement of the substrate atoms plays an important role in the lateral manipulation. As the atom moves in various routes, it encounters different potentials. The research about LM has mainly

focused on the (111) surface of the FCC crystal [17]. For the (111) surface, the most normal dragging route is the [110] direction. As shown in Fig. 2.5, migration along the [110] direction will take place in a zigzag route. For routes that deviate by 10° or 20° from the [110] direction, the migrations of atom include jumps between different rows in addition to zigzag routes. For migrations deviated from the [110] direction by 30° which is the [211] direction, the atom moves alternately between the shortest route and a semicircular route over the top of the surface atoms.

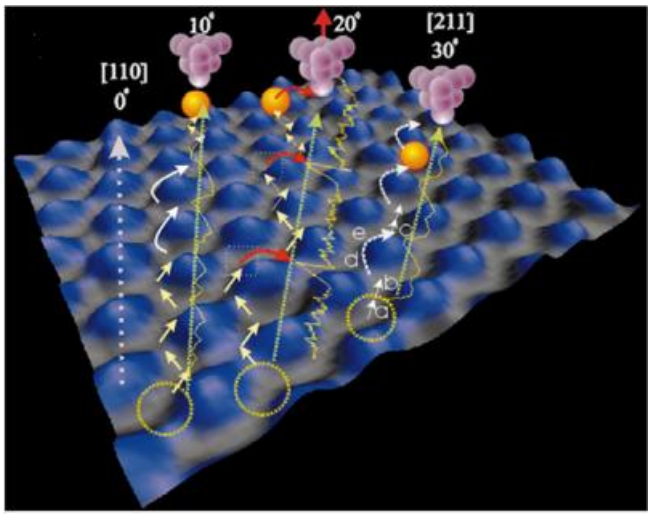

Fig. 2.5 Schematic diagram of the different orientations of the atomic manipulation on the Ag (1 1 1) substrate and each peak represent one atom. The diagram shows three different schemes of atomic manipulation with 10°, 20° and 30° deviation from the [110] direction. [17]

Another type of atomic manipulation besides lateral manipulation is vertical manipulation [19]. Atomic manipulations in which the manipulated atoms move between the surface and the tip are called vertical manipulations. Vertical manipulation is divided into two main branches, the movement from the tip to the sample surface and the movement from the sample surface to the tip. Since the manipulated atom at the sample surface is close to more atoms than at the tip, they will receive smaller interactions at the surface [12]. Therefore, the migration of atom from the surface to the tip is straightforward and only requires the tip to be lower. At that point, the tip is in mechanical contact with the sample surface atoms. When the

tip is raised, the atom is lifted from the sample surface by the tip. However, in contrast, it is much more difficult to get the atom to migrate from the tip to the sample surface because of the stronger interaction of the tip. Therefore, additional forces are required to make the atom migrate from the tip to the sample surface. The most common method to achieve desorption is to apply a tunneling current to the tip [19][20]. In addition to this, the inversion of the bias [18][21], the atomic tunneling effect [22], and the thermal effect [23][24] are all feasible for the desorption of atoms from the tip. In particular, for metals adsorbed on metal tips, they are bonded by more powerful metal bonds and therefore need to be desorbed by direct mechanical contact [25][26].

Another branch of atomic manipulation is the selective bonding of molecules. Through the precise localization of the molecular structure by STM, tip can inject tunneling electrons precisely into a specific chemical bond. The molecule will undergo vibrational relaxation [14][28] and the chemical bond will break when the energy of the transferred electrons is higher than the dissociation energy of the bond. This technique allows the selective separation of atoms from molecules without destroying the remaining parts [29]. A typical example of which is the separation of halogen atoms from organic molecules [15]. When a chemical bond is broken, the tunneling current pulses. So, the result of the selective separation can be monitored by the tunneling current.

For STM imaging, a tip of a few atomic widths may already provide sufficient resolution. But for atomic manipulation, the reliability of the atomic manipulation is highly dependent on the tip sharpness, which is not only related to the number of atoms at the tip of the probe, but also related to the tip's height and shape [27]. This atomic-scale precision requirement is difficult to achieve for conventional electrochemical etching. However, VM can be used to fit the tip to suit the sharpness requirements. For the electrochemically etched tungsten tip, a softer metal such as copper, silver or gold can be used to fit the tip for a more controlled tip shape. This

can also be considered as an atomic manipulation technique. In this operation, the tip is inserted into the metal surface, where it is in physical contact with the sample. So that, it is partially covered by the base metal and the heat generated in the process reshapes the tip to give it a more 'natural' appearance. At the same time, the tunneling current applied to the probe also reshapes the tip. Getting an atomic resolution image of the tip is difficult, so the quality of the tip should be judged by using it to perform an atomic resolution scanning. The brief condition of the tip can be determined by the image resolution. Checking and correcting the tip state should be the first step in all atomic manipulations.

2.2 The Au (111) Surface

As a kind of precious metal, gold shows good stability in both atmospheric and acidic solutions. At the same time, as an FCC metal, its lattice has a high atomic stacking efficiency. Gold crystal is also the only Face-Centered Cubic metal with HCP herringbone reconstruction on the (111) surface [30]. Thus, gold becomes a good substrate in surface physics, which combines the stability of substrate with the unique electronic structure of the reconstruction well.

Before STM techniques were invented, techniques such as High-Resolution Helium Atomic Scattering (HRHAS) [37], Low-Energy Electron Diffraction (LEED) [34][35], Reflected High-Energy Electron Diffraction (RHEED) [35][36] and Transmission Electron Microscopy (TEM) [31-33], were used to study the (111) and (100) surfaces or interfaces of gold in depth. And for the first time, atomic resolution images of gold surfaces were obtained with the advent of STM technique [38][39].

2.2.1 The Feature of the Au (111) Surface

Face-Centered Cubic (FCC) is one of the most stable crystal structures and also has the highest atomic packing density. Like silver, copper, iridium, platinum and nickel, gold is also a Face-Centered Cubic crystal. As shown in Fig. 2.6, in one unit cell,

these balls represent the gold atoms falling at all eight corners of the cube and the centers of the six faces. The three axes extending from it represent the [100], [010] and [001] crystal directions. The grey plane enclosed by the six red balls represents the (111) plane. The gold crystal has the lattice constant a = 407.89 pm [40] as the side length of the cube.

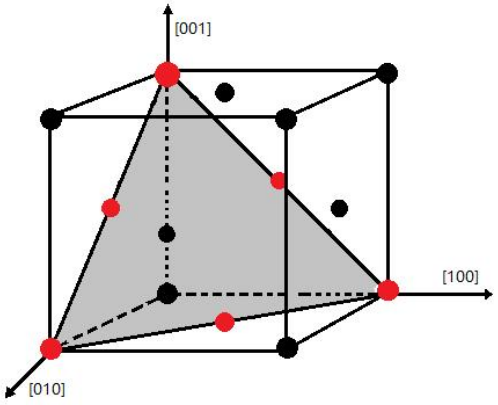

Fig. 2.6 Ball-stick model of an FCC lattice, with the black and red balls representing gold atoms. The red balls represent the gold atoms falling on the (111) plane which is represented by the grey balls.

As shown with Fig. 2.7, the (111) plane of gold is the close-packed plane of gold atoms, while the close-packed directions of gold atoms are these six directions: $[\bar{1}10]$ $[1\bar{1}0]$ $[\bar{1}01]$ $[10\bar{1}]$ $[0\bar{1}1]$ $[01\bar{1}]$. Considering the symmetry of the crystal, these six directions can be unified into one equivalent crystal direction <110>. In addition to this, another important equivalent crystal direction on the surface is <112>, which is vertical to the close-packed direction of the atoms.

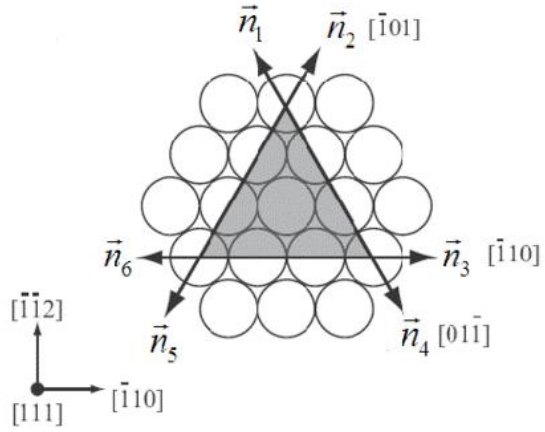

Fig. 2.7 The atom arrangement in (111) surface and the six close-packed directions. [41]

In addition to the FCC (111) plane, the (0001) plane of Hexagonal Closed Packed (HCP) crystal is also the close-packed plane. The difference between these two planes is reflected in the way atoms stacked between the different layers. As shown in Fig. 2.8 (b) and (d), FCC (111) and HCP (0001) are identical when only a single layer of atoms is considered. The difference is that the HCP (0001) surface adopts an ABA-type stacking, where the surface is stacked in 2-layer periodicity. The third layer atoms in HCP will return to the sites where the first layer of atoms is located. On the other hand, the FCC (111) surface has an ABC-type stacking, with a stacking periodicity of 3, and the fourth layer will return to the sites where the first layer of atoms is located. Since the Au (111) surface partially change to the HCP structure from FCC due to reconstruction, this structure difference should be noted for the study of Au (111) surface.

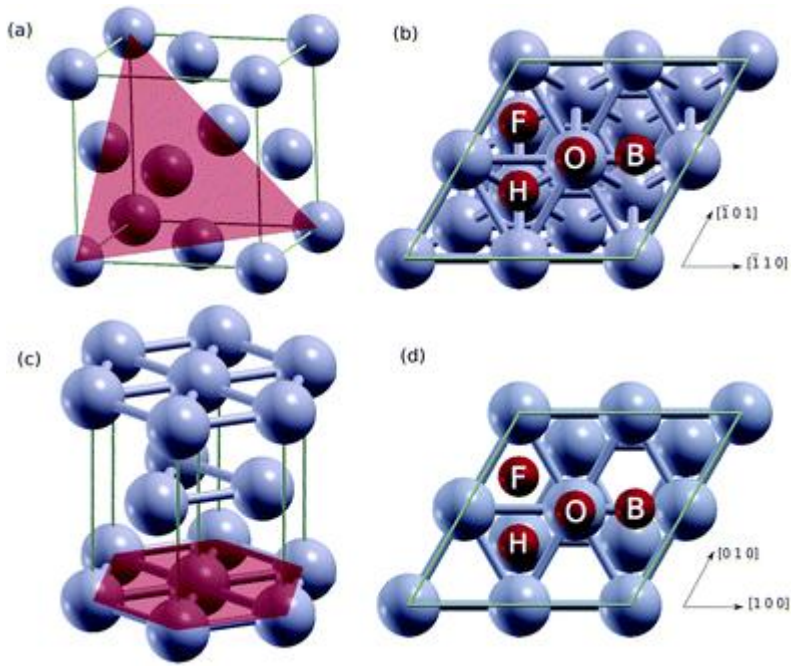

Fig. 2.8 (a) Ball-stick model of FCC structure. The red plane is (111) plane. (b) Ball-stick model top view of FCC (111) surface with the adsorption sites. (c) Ball model of HCP structure. The red plane is (0001) surface. (d) Ball-stick model top view of HCP (0001) surface with the adsorption sites. The adsorption sites 'B', 'F', 'H' and 'O' showing in (b) and (d) mean the Bridge, FCC, HCP and Ontop positions [42].

The ideal infinitely big flat monolayer Au (111) surface is difficult to obtain experimentally. So, steps on the gold surface are unavoidable in most Au (111) surface preparation methods. At the same time, the gold surface step is an important surface deposition site that is well studied. As shown in Fig. 2.9 (a), for unreconstructed (111) surfaces, there will be two types of steps, known as Type A steps and Type B steps. Type A steps represent the {100} microplanes and Type B steps represent the {111} microplanes. Type A steps have a higher atomic density so they will have a lower step energy than Type B steps [43]. For silver or copper (111) planes, since the A and B steps have close energies, growth along both types of steps have similar growth rates, as evidenced by the smoother edges of the islands growing on the surface [44]. For gold surfaces, the different step energies result in different growth rates, and therefore the steps of Au will be more linear or folded.

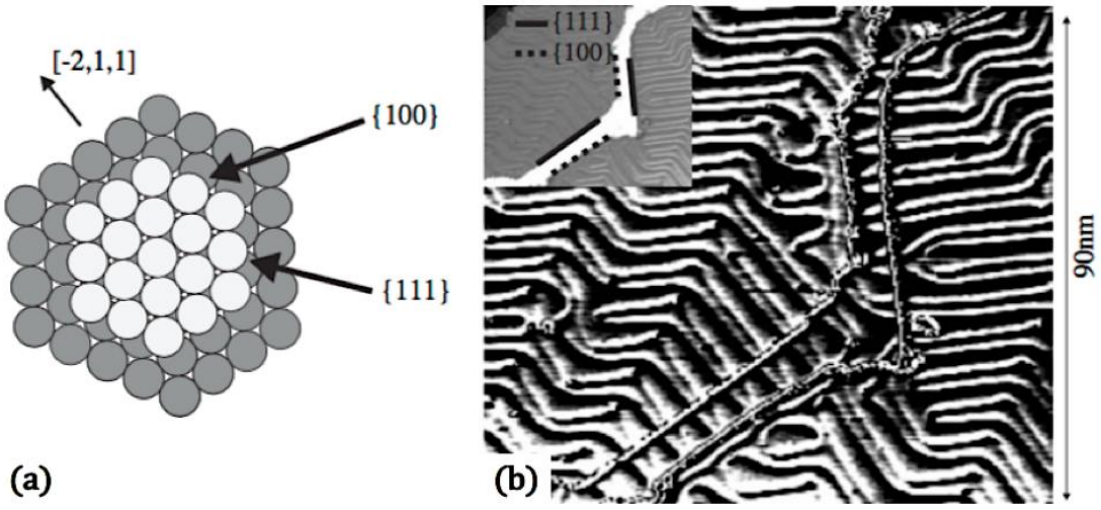

Fig. 2.9 (a) Schematic diagram of the (111) surface, showing two types of steps. One represents {100} microplane and the other represents {111} microplane. (b) STM image of the Au (111) surface. 100 nm × 90 nm, T=150 K. Steps {111} are marked with solid lines and steps {100} are marked with dashed lines. The direction of the steps is the same as in (a). [43]

The most intuitive difference between the two types of steps on Au (111) is the different pattern of Discommensuration Lines (DLs) on step edges, which are caused by the reconstruction [43][45][46]. As shown in Fig. 2.9(b), the DLs will pass through the Type B step and connect to the DLs below it. Whereas for the Type A step, the DLs will truncate and form a U-shaped end return. In simple terms, since the Type B step is a {111} microplane, it allows the atoms to be reconstructed into HCP structures on the step. Whereas for the {100} microplane, the atoms at the edge of the step can only remain as FCC structures and therefore the DLs have to be truncated.

2.2.2 Reconstruction and the 23×√3 Unit Cell

Surface reconstruction is the phenomenon in the finite-size periodically symmetrical crystal that crystal's surface assumes a different structure with the inside of the crystal, due to symmetry breakage. Reconstruction has been widely observed and studied on clean crystal surfaces. Among these, the (111) surface reconstruction of gold is distinctive because it's the only FCC (111) surface with a HCP reconstruction on it.

Since 1974, techniques like Helium Atom Scattering (HAS) [37], Reflection High Energy Electron Diffraction (RHEED) [36] and Low-Energy Electron Diffraction (LEED) [34] have confirmed the existence of (23×√3) unit reconstructions on gold surfaces. The images of Au (111) surface were obtained by Transmission electron microscope (TEM) in 1983 by studying gold islands growing on molybdenum disulfide surfaces [47], which establish a model for Au (111) surface reconstruction: alternating HCP region with FCC region. This was also confirmed by theoretical calculations [48]. By STM technique, atomic resolution images of the Au (111) surface are obtained and thus gaining a more in-depth understanding of the Au (111) surface reconstruction.

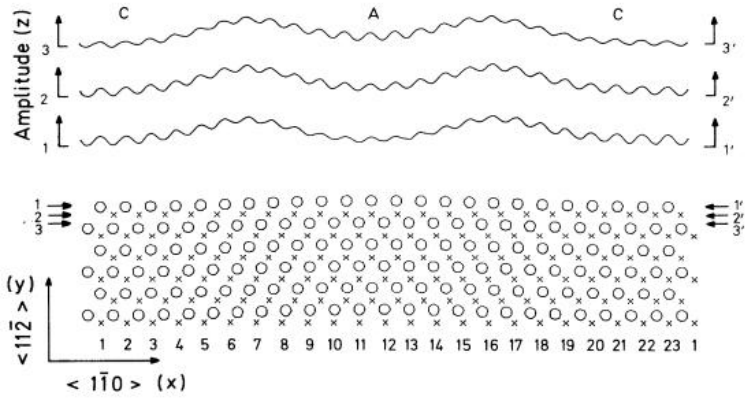

Fig. 2.10 Top: Schematic diagram of the surface undulations at three locations on Au (111) surface. The vertical scale is exaggerated. Bottom: Schematic diagram of the atomic arrangement. The circles represent the top layer atoms and the crosses represent the second layer atoms. [37]

The basic unit for the reconstruction of Au (111) surface is the (23×√3) unit. As shown in Fig. 2.10, the circles and crosses represent the atoms of the first and second layers of Au (111) surface, respectively. 23 atoms stuffed into the original 22 gold atom sites on the FCC (111) surface, which results in a 4.55 % uniaxial contraction of gold atoms along one of the <110> directions. In one unit, gold atoms gradually change from the FCC sites to the HCP sites and change to FCC again. While in the transition region, those gold atoms that are neither at the FCC sites nor at the HCP sites fall completely or partially on the bridges of the underlying gold atoms, so that they are vertically above the atoms located on the sites. Therefore, at the junction of

the FCC and HCP regions, a peak appears. As a result of the periodic repetition of the reconstruction units on the gold surface, these peaks form two prominent ridges on the surface, which are called DLs.

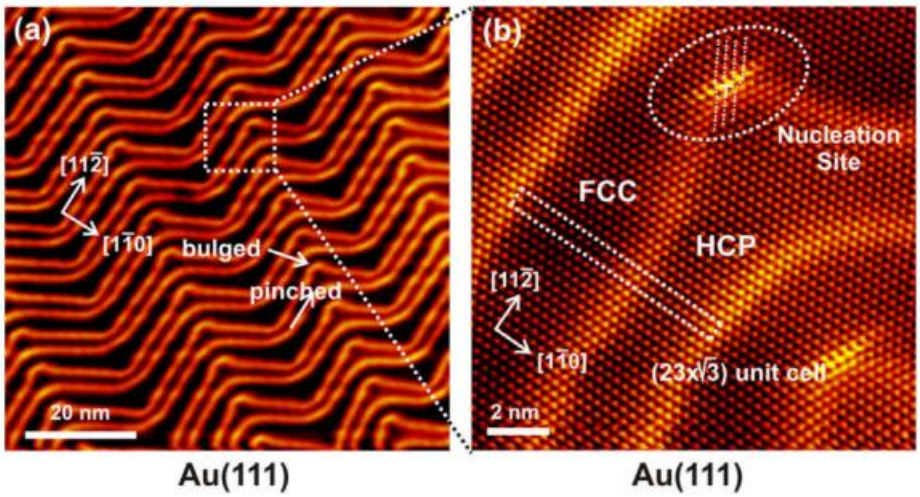

Fig. 2.11 (a) STM image of DLs on Au (111) surface. Pinched and bulged elbow sites are shown by arrows. (b) An additional row of atoms on the bulged elbow close to the FCC region, marked with an oval. [49]

As shown in Fig. 2.11, the DLs on the gold (111) face always occur in pairs, corresponding to the two peaks in the (23×√3) unit. The main part of which is the parallel DLs extending in the <112> direction, while the different DLs are arranged in parallel with each other in the <110> direction. After a certain distance, they also show a 120° reversal, showing a herringbone zigzag pattern. The other part of DLs is the elbow site that occurs at the inflection points of the DLs. There are three kinds of elbow sites. One of which is the bulged elbow site where the DLs protrude into the FCC region and another is pinched elbow site where the elbow is concave into the HCP region. Both of which sites appear on one of the two DLs and there is another kind of elbow site on the other DLs which is smoother.

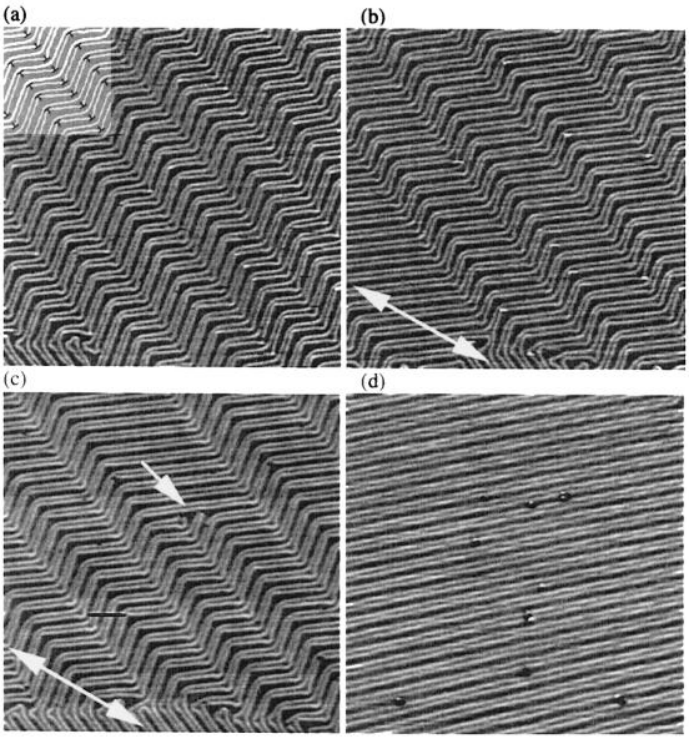

Fig. 2.12 STM images of Au (111) surface. 170 nm × 170 nm. Double headed arrows show the direction of applied stress on the mica substrate. (a) Non applied stress sample. (b) 0.17% uniaxial compressive stress is applied and the sample is annealed above 80°C. The irregular domain appears. (c) The stress increasing to 0.23% and anneal the sample again. The single arrow points to the new occurring site. (d) Another sample after annealing with 0.4% uniaxial compressive stress. [50]

Intuitively, the herringbone reconstructions of Au (111) appear because of the stress imbalance on the surface. Compared to the atoms inside the crystal, the Au atoms on the surface are only adjacent to the gold bulk on one side and have a smaller coordination number. Therefore, due to the atomic potential of the crystal, the surface gold atoms reduce the atomic distance by surface contraction. At the same time, the gold atoms between the FCC and HCP regions cannot fall on the lowest energy site but on the bridge due to the contraction of the gold atoms. The DLs bend periodically to make the gold surface anisotropic to release the stress [51][52]. Experiments have shown that the herringbone DLs of the Au (111) reconstruction can be manually removed by applying mechanical stress to the mica substrate of the gold surface.[50]

As shown in Fig. 2.12, (a)-(c) show the gradual evolution of the surface reconstruction of the same sample which has been annealed and the applied uniaxial compressive stress has been varied from 0% to 23%. Fig. 2.12(d) shows the area after annealing at 0.4% uniaxial compressive stress for different sample where only one large domain survives. Similarly, the defects created by tip contact to the gold surface can cause a change in the stress balance of the Au (111) surface, which also changes the arrangement of the gold surface reconstruction [53].

In addition to mechanical stresses, temperature [54-56] and surface adsorption [57-62] can also transform the reconstruction. In the range from 856 K to 879 K, the short distance disordered reconstruction can be observed [54] and above 1250 K, the gold surface will change into a different structure called discommensuration fluid phase [55]. All the reconstructions mentioned above are observed in UHV environment. For gold surfaces in atmospheric or solution environments, it has been experimentally demonstrated that the reconstruction of Au (111) surfaces will disappear in non-UHV environments [57], which may be related to the adsorption of air or solutions molecules. The electronegativity of the adsorbed molecules also has an effect on the reconstruction. If C_{60} molecules, which are less electronegative than gold (gold's electronegativity is 2.54 and C_{60} is 2.55 in Pauling scale [63]), are deposited on the Au (111) surface, there will be an electron transition from the substrate to the C_{60} molecule, resulting in a (1×1) structure transformation of the reconstructed part [58-60]. If, on the other hand, atoms with more electronegativity, such as K (electronegativity is 0.82 in Pauling scale) or Na (electronegativity is 0.93 in Pauling scale), are deposited, electrons will be transferred from the adsorbed atoms to the gold surface, resulting in an increased compression of the reconstruction [61][62].

The elbow site is the most stress concentrated region in the reconstruction and also the lowest energy site, making it the absorption site for many surface depositions. Many studies of Ni [64][66], Co [65], C_{60} [58- 60], MO and MoS_2 [49][75] have all demonstrated the

nucleation at the elbow sites of surface growth.

2.2.3 Metal Adsorption on Au (111)

Au (111) surface is received extensive attentions because of the unique properties of its herringbone reconstruction. Relying on the chemical inertness of gold and the long-range orderliness of the reconstruction, the Au (111) surface is an ideal substrate for the manufacturing of many nanoscale structures. The deposition of many metal atoms on Au (111) surfaces has been studied in detail in many experiments [64-75]. In this case, there are two different patterns of metal adsorption on Au (111) surfaces. For the first type, the metal atoms preferentially nucleate at the elbow sites of the DLs and then grow into nucleation-dependent three-dimensional clusters. For example, metals such as Fe [67], Co [65] and Ni [64][66] follow this pattern of adsorption growth. In contrast, for the second group of metals, such as Al [68], Ag [69], Cu [70], and Au itself [71], preferential nucleation is not observed experimentally. These metals mostly nucleate and grow along the steps of the surface irregularly. As the surface coverage gradually increases, the metal islands will be blocked by DLs.

The adsorption mechanism of preferential nucleation at the elbow sites was early on explained simply by having a higher metal binding energy at the elbow sites. However, this theory could not be used to explain the different behaviors exhibited in adsorption of metals such as Fe, Co, Ni versus Au, Ag, Cu. In 1996, JA Meyer et al. monitored the nickel deposition on the surface of gold (111) by using STM, which led to a completely new model for metal nucleation at elbow sites [73]. By controlling the amount of nickel deposited, at a very low coverage of 0.002 ML, it is seen that no clusters of nickel atoms are located at the elbow sites. Conversely, depressions which have not been observed on the clean Au (111) surface occur at the elbow sites. This is explained as nickel atoms replacing the gold atoms at the elbow sites and forming the nucleus embedded in Au (111) surface. The dimer first replaces the gold atoms at the elbow site and embeds into the Au (111) surface, as shown in Fig. 2.13. This is also

replicated in the surface deposition of cobalt.

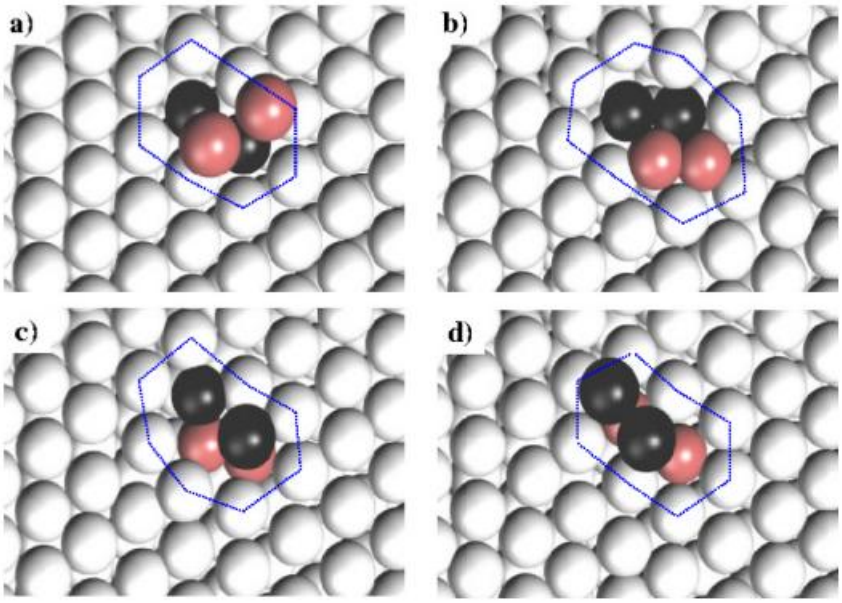

Fig. 2.13 Ball models of cobalt cluster nucleation on gold (111) surface simulated by molecular dynamics. It demonstrates the process of cobalt clusters replacing gold atoms and embedding into the Au (111) surface. The white balls represent the gold atoms, the red balls represent the cobalt atoms and the black balls represent the gold atoms replaced by the cobalt atoms. [72]

For the reason why this nucleation pattern does not occur in the adsorption of metals such as Au, Ag, Co and Al, JA Meyer gives an intuitive explanation in a simple way. As shown in Table 2.1, which lists the sublimation heat and surface free energy of a variety of metals. The sublimation heat and surface free energy of Au, Cu and Al are significantly less than those of Fe, Co and Ni, while Au is just right between the two types of metals. This intuitively suggests that the model of nucleation at the elbow site by replacing gold atoms requires the adsorbed metal having a higher surface free energy than gold substrate. Further, this theory also predicts that Pd nucleates at the elbow of the gold (111) surface, which is confirmed by experiment [74].

Table 1

Element	Surface free energy (eV)	Heat of sublimation (eV)
Ag	0.50	2.95
Al	0.56	3.39
Cu	0.69	3.51
Au	0.72	3.79
Ni	0.90	4.45
Co	0.94	4.40
Fe	0.96	4.32

Table 2.1 The surface free energy and sublimation heat for Ag, Al, Cu, Au, Ni, Co and Fe. [73]

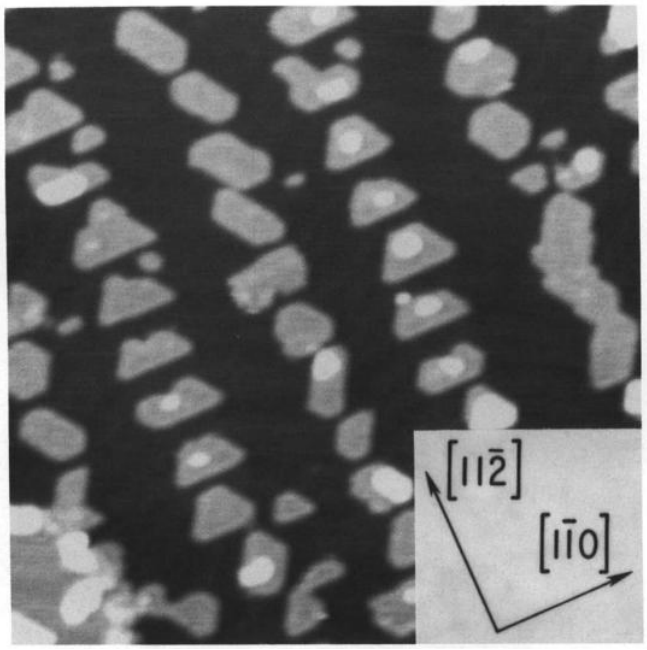

Fig. 2.14 STM image of 0.25 ML Fe on Au (111), 80 nm × 80 nm. Monolayer Fe islands nucleate at the elbow sites of DLs. [67]

As the coverage gradually increases, metal clusters at elbow sites will grow into clusters along the nucleation epitaxy. Due to the long-range orderliness of the herringbone structure, these clusters will form long-range ordered dot arrays on the Au (111) surface. For nickel and iron, the clusters will form regular islands of truncated triangles [66]. With further coverage increasing, as seen in Fig. 2.14, the

appearance of the second layer will be earlier than the complete aggregation of the first layer. While for cobalt, due to its lattice mismatch with gold, it is not possible to form compact and ordered clusters but shows an irregular shape. With coverage increasing, similar to nickel, this epitaxy of the same layer and stacking of layers will proceed simultaneously until forming a several layers film on the gold substrate [76].

2.3 Cobalt

As a magnetic metal, cobalt atoms preferentially nucleate on elbow sites of the Au (111) surface. This ordered nanostructure with magnetic anisotropy can play an important role in sensors for giant magnetoresistance, magnetic data storage and spin electronics [77][78]. Therefore, various experimental techniques have been all used to study the adsorption of cobalt on the Au (111) surface, such as X-Ray Diffraction [79][80], Ferromagnetic Resonance Measurements [81], Auger Electron Spectroscopy (AES) [82], STM [83], Reflection High-Energy Electron Diffraction [79], Helium Atom Scattering [84] or Scanning Electron Microscopy with polarization analysis [85].

Due to the 14% lattice mismatch between cobalt and gold, at RT, cobalt cannot grow layer by layer on the Au (111), but will preferentially form bilayer islands, which will then gradually epitaxially merge [83][84]. In the case of cobalt grown at low temperature, the growth of cobalt is more determined by kinetic and exhibits a layer-by-layer growth pattern [65]. Heating cobalt cluster samples results in the cobalt clusters sinking into the gold substrate [65] and the magnetic anisotropy of the cobalt clusters will be affected [86][87].

2.3.1 Co Cluster on Au (111)

Cobalt crystal is a HCP crystal with a lattice constant of 251 pm on the (0001) face and the lattice constant of Au (111) is 288 pm. 14% lattice mismatch between these two metals dictates that cobalt cannot be close-packed on the Au (111) surface. Therefore, the nucleation mechanism for cobalt clusters grown epitaxially on the Au

(111) surface, as described above, is an atomic displacement at the elbow site, and the displaced atoms will become the nucleation sites for the cobalt clusters. The lattice mismatch between cobalt and gold results in that the monolayer cobalt island on the Au (111) surface is rugged. [65][83][88][89] This can be simply explained that some cobalt atoms locate on the bottom sites of the Au (111) substrate and others on the on-top sites. As a result, the cobalt atoms preferentially form bilayer cobalt clusters compared to the epitaxial growth of a single cobalt film, as reported in many literatures. [65][83][88][89] This phenomenon has been explained as the bilayer structure attenuating the strain accumulation in cobalt clusters comparing to the monolayer cluster with same Co atoms in article by Bert Voigtlander et al.[83] In that article, the authors give a quantitative strain relaxation of 8%, but do not give the calculation method or reference.

Thus, for epitaxially grown cobalt clusters on the Au (111) surface, bilayer islands are the more stable structure. An intuitive relationship between the cluster structure and cobalt coverage has been obtained based on experiments based on the helium atom scattering technique (TEAS) by Christian Tölkes et al [82]. For islands below the size of 15-20 cobalt atoms, the cobalt cluster is monolayer. With size above that, the cobalt will grow to bilayer island. When the cobalt coverage reaches above 0.7 ML, the cobalt clusters will aggregate in the $[11\bar{2}]$ direction and aggregate in the $[1\bar{1}0]$ direction with 1.5 ML cobalt. When the coverage reaches 2.5 ML, the first and second layers of cobalt coalesce into a film and the layers 3 to 5 will grow in a quasi-two-dimensional structure.

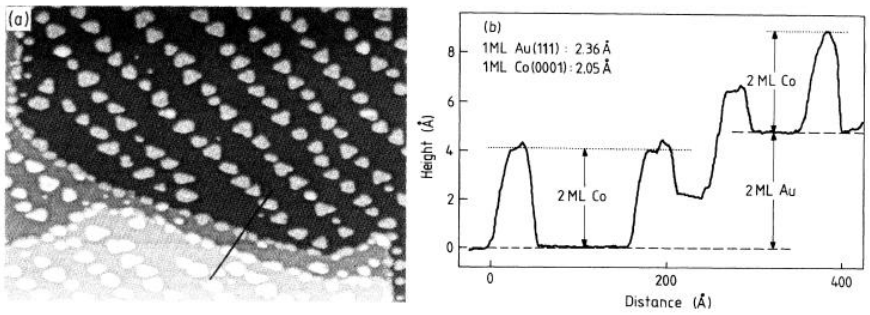

Fig. 2.15 (a) STM image of 0.3 ML Co on Au (111), 160 nm × 160 nm; bilayer Co clusters nucleate at the elbow sites. (b) Height information of the line shown in (a), the height difference between Co and Au is clear. [83]

In the STM image, the thickness of monolayer Au atoms is 2.36 Å, while for monolayer cobalt atoms is 2.05 Å, slightly less than gold. Therefore, it is possible to separate Co monolayers from Au monolayers and Co bilayers from Co monolayers on a single gold step in the STM image by height.

For higher coverage cobalt, according to a study made by N Haag et al. in 2016 [76], as shown in Fig. 2.16, with 8 ML coverage, cobalt film is still dependent on the gold substrate and exhibits highly symmetrical orientations and steps to the Au (111) surface, even after annealing. However, when the coverage reaches 20 ML, the cobalt behaves more like massive cobalt crystals rather than a thin film of cobalt on a gold substrate.

The growth of cobalt is mainly influenced by the reconstruction DLs of the Au (111) surface at room temperature. However, at low temperature, the growth of cobalt will be mainly influenced by kinetics [85]. Cobalt atoms on the Au (111) surface will have a lower surface free range at low temperature. In other words, it will be more difficult for cobalt atoms to diffuse across the diffusion energy barrier on the gold surface. Therefore, cobalt will nucleate extensively on the surface with a higher nucleation density. At a low temperature of 30 K, cobalt will form various small monolayer cobalt islands on the surface. These cobalt islands will grow to a size around 10 atoms

and then begin to grow layer by layer differently than at room temperature. The temperature boundary between these two different growth modes should be around 120 K, according to I. Chado et al. [85]

2.3.2 Temperature Control Evolution of Cobalt Clusters

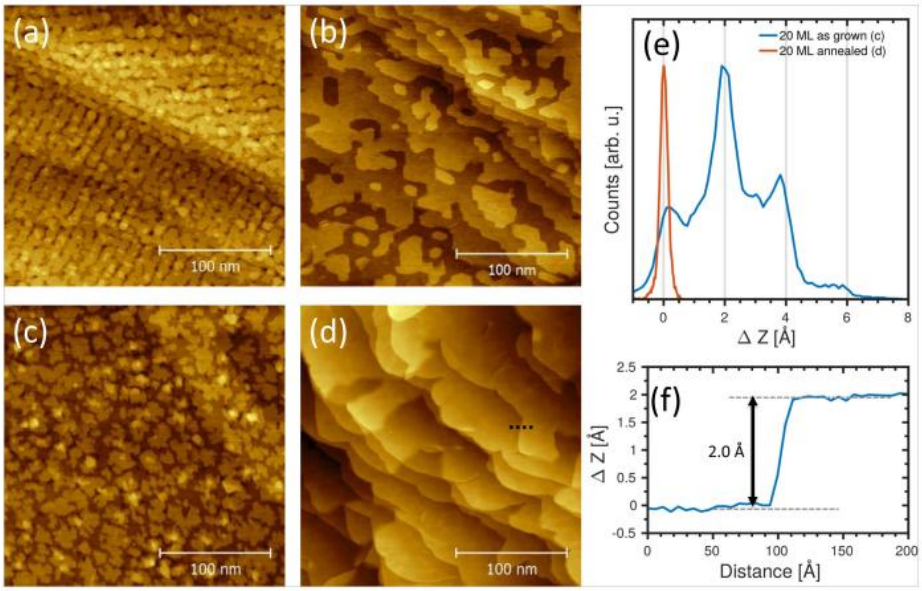

Fig. 2.16 STM images of cobalt on Au (111) substrate: (a) Cobalt coverage is 8 ML, non-annealing. (b) Sample(a) annealed at 300°C, 45 min. (c) Cobalt coverage is 8 ML, non-annealing. (d) Sample (c) annealed at 300°C, 5 min.(e) The distribution in relative height Co islands in samples (c) and (d) before and after annealing. (f) The height information of the line shown in (d). [76]

Annealing is a common treatment for epitaxially grown metals. As shown in Fig. 2.16, a clear structure transformation of the cobalt film on the gold substrate after annealing can be seen in the STM image. By Fig. 2.16 (e), the variance of the height of the 20ML cobalt film decreases significantly after annealing, indicating that the epitaxially grown cobalt films become flatter after annealing. At the same time, a moiré superstructure was observed on the annealed lower coverage cobalt film (4ML). As shown in Fig. 2.17, this is a hexagonal lattice of the moiré superstructure whose periodicity is 31.5 ± 2.7 Å and azimuthal orientation is similar to the close-packed

orientation of Au (111) surface. This superstructure is caused by the periodic undulation of the cobalt atoms due to a lattice mismatch between cobalt and gold. The symmetry of Au (111) in <110> directions also lead to the fact that this periodic undulation must be hexagonal. As shown in Fig. 2.17, the azimuthal orientation of the moiré superstructure is similar to <110> direction. This is consistent with the literature report [87].

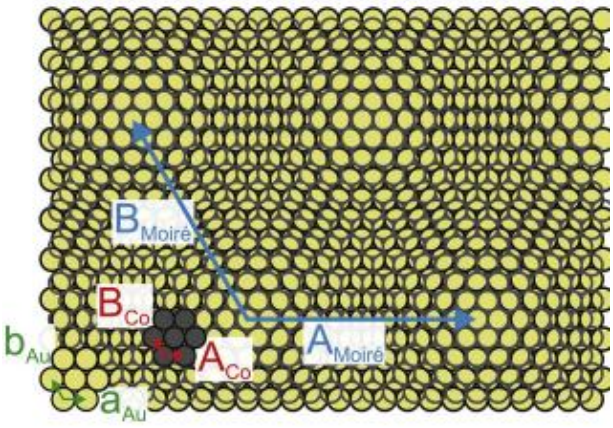

Fig. 2.17 Ball model of the Moiré mode of a cobalt film under 4 ML. The different colored vectors represent different lattices. Green represents Au (111) surface, red represents cobalt cluster and blue represents the Moiré superstructure. [76]

Similar phenomena have been observed for nickel, which also has preferential nucleation at elbow sites and is also magnetic, similar as cobalt [91]. As shown in Fig. 2.18, for the 8ML nickel film grown on the Au (111) substrate, after annealing at 500 K, the same aggregation and flattening of surface nickel islands was observed. After annealing at 550 K, the same moiré superstructure was observed. After annealing at 600 K, a triangular superstructure appeared on the surface of the sample, which is similar to the ultra-thin gold film on the Ni (111) or Ni (110) face after annealing with similar morphology [92][93]. These is due to the lattice mismatch between Ni and Au, similar to the Moiré superstructure of Co film on Au (111). After annealing at 650 K, the gold (111) surface reappeared on the sample surface. In the STM images, a typical herringbone reconstruction can be observed after annealing at 650 K. Medium Energy

Ion Scattering (MEIS) also demonstrates the reappearance of gold film on the surface from the annealed cobalt/gold sample [91]. This indicates that after annealing, a large number of Au atoms cross the nickel layer from the substrate of the sample to the surface of the Ni film. A similar phenomenon of gold atoms diffusion through the nickel layer to the surface was also reported in the work of Katona et al [94].

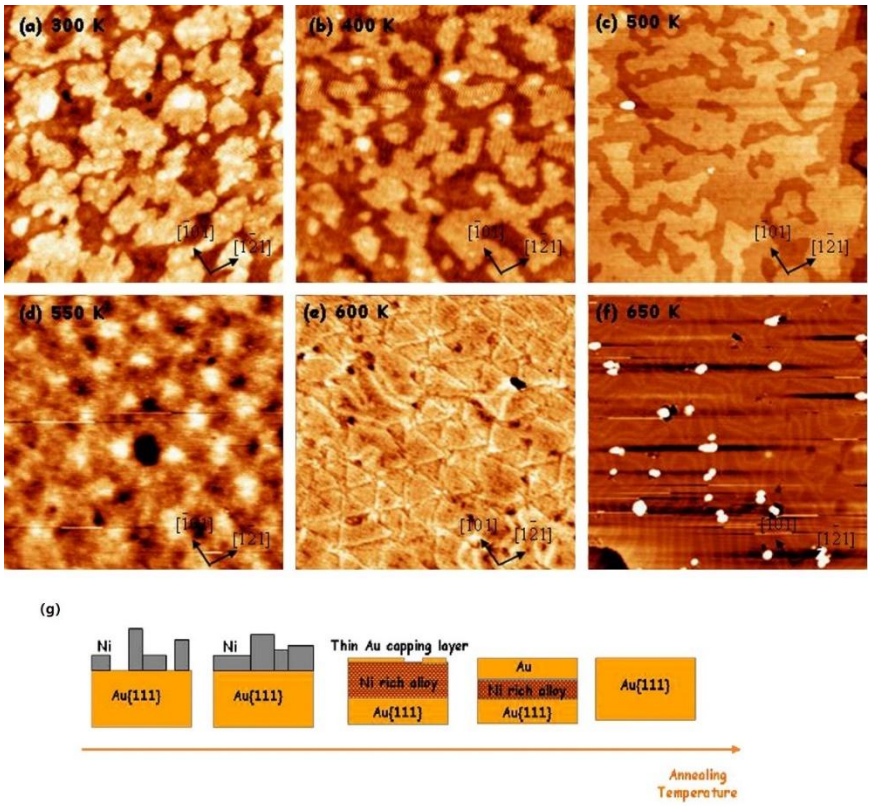

Fig. 2.18 (a) STM image of Ni film on Au (111) substrate, 4 ML, 52 nm × 52 nm. (b) STM image of Ni film on Au (111) substrate, 4 ML, 400 K annealing, 66 nm × 66 nm. (c) STM image of Ni film on Au (111) substrate, 4 ML, 500 K annealing, 180 nm × 180 nm. (d) STM image of Ni film on Au (111) substrate, 4 ML, 550 K annealing, 47 nm × 47 nm. Moiré structure is forming. (e) STM image of Ni film on Au (111) substrate, 4 ML, 600 K annealing, 70 nm × 70 nm. Triangular features are observed. (f) STM image of Ni film on Au (111) substrate, 4 ML, 650 K annealing, 74 nm × 74 nm. Ni disappeared and the reconstructions show again. (g) Diagram of the sinking of Ni during annealing on Au (111). [91]

For high temperature annealing of cobalt films, no gold re-covering cobalt films was

observed at 575 K [76], which is similar to the case for nickel at this temperature range [92]. There is a lack of relevant experiments for higher temperature annealing at 600 K or above to show what will happen. However, the sinking of cobalt clusters into the gold surface at high temperature has been reported in the study for low coverage cobalt clusters, rather than cobalt films [65].

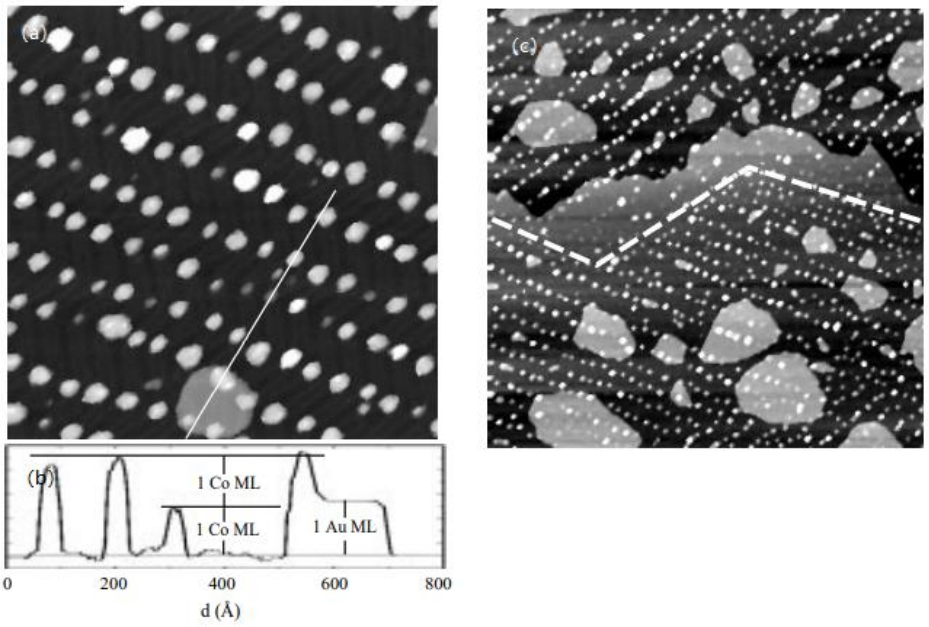

Fig. 2.19 (a) STM image of cobalt on Au (111), after annealing at 450 K for 1 minute, 0.3 ML, 100 nm × 100 nm. (b) Height information of cobalt cluster and Au step. (c) STM image of ejected gold atoms and sink Cobalt clusters. Annealing at 600 K, 1 min, 300 nm × 300 nm. [65]

For 0.3 ML ordered bilayer cobalt clusters on Au (111) surface, after 1 min 450 K annealing, cobalt clusters with monolayer height have been observed by STM, while some epitaxially grown monolayer gold islands appear around cobalt clusters. By tracking the number of gold atoms, it can be shown that the sinking of cobalt clusters at that time leads to the expulsion of gold atoms. For the same sample, after 1 min 600 K annealing, some of the cobalt clusters sink to the same height as the gold surface.[65] For higher temperature annealing, as shown in Fig. 2.20 (d), for 1.5 ML cobalt, the herringbone reconstructions are observed by STM images after 750 K annealing. It means that the cobalt clusters completely sink into the Au surface, which is similar to

the behavior of the nickel film [91]. Cobalt has a strong sticking coefficient to gold atoms. So, for additional Au deposition on Co/Au (111) sample, gold atoms' preferential nucleation at the edges of cobalt clusters can be observed [95]. This may also explain why the expulsed gold atoms surround the cobalt cluster. The gold surrounding the cobalt cluster significantly reduces the reactivity of the cobalt cluster and also increase the magnetic anisotropy of the cluster [96].

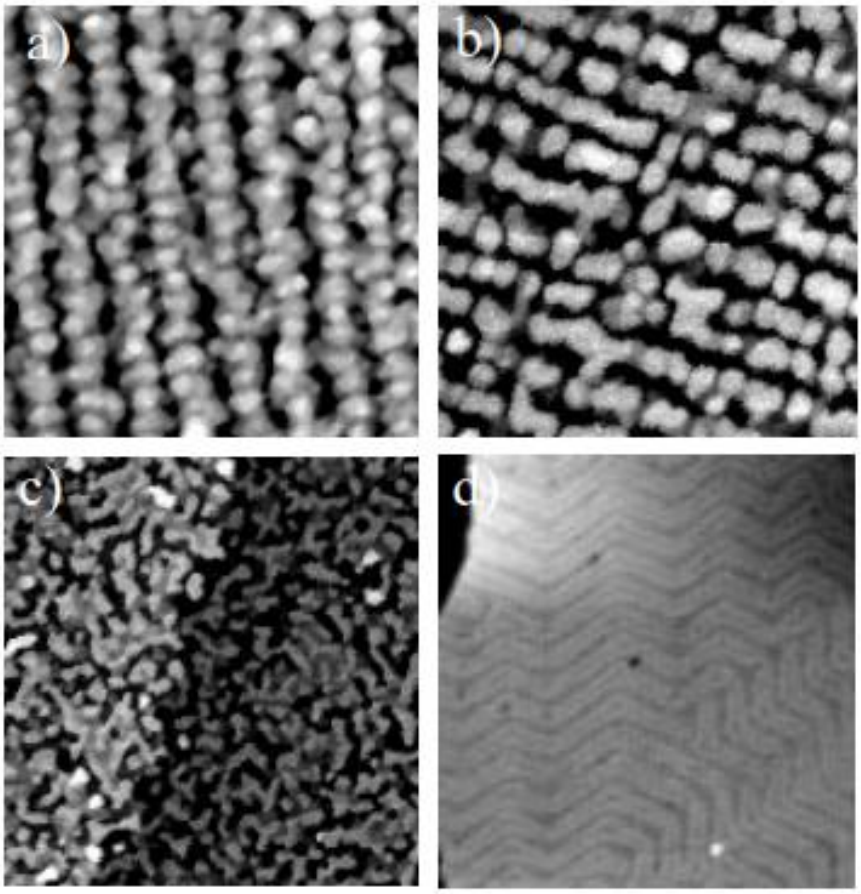

Fig. 2.20 STM image of cobalt on Au (111), 1.5 ML, 100 nm × 100 nm. The sample is prepared at 300 K, imaged at RT: (a) Unannealed samples. b) The samples were annealed at 550 K for 1min. (c) Anneal the sample at 600 K for 1min. (d) Anneal the sample at 750 K for 1min. [96]

2.4 Fullerene

Fullerene is a series of carbon isomers whose structure consists entirely of carbon atoms, with rings of 5 to 7 atoms, closed or partially closed, in a network-like

structure [97][98]. Fullerenes are usually spherical or ellipsoidal in shape. Fullerenes are often denoted as C_n, meaning molecules composed of n carbon atoms, such as C_{20}, C_{28}, C_{36}, C_{60}, C_{70}, C_{76} and C_{84}. What's more, multiple isomers of the same atom number may exist. Of these, the best known and most studied fullerene is C_{60}, also known as buckminsterfullerene, which is well studied in many fields, including surface science, because of its unique spherical cage shape and symmetry. In surface science, it is often used as a block of nanostructures in surface self-assembly [99-101].

2.4.1 C_{60} Molecules

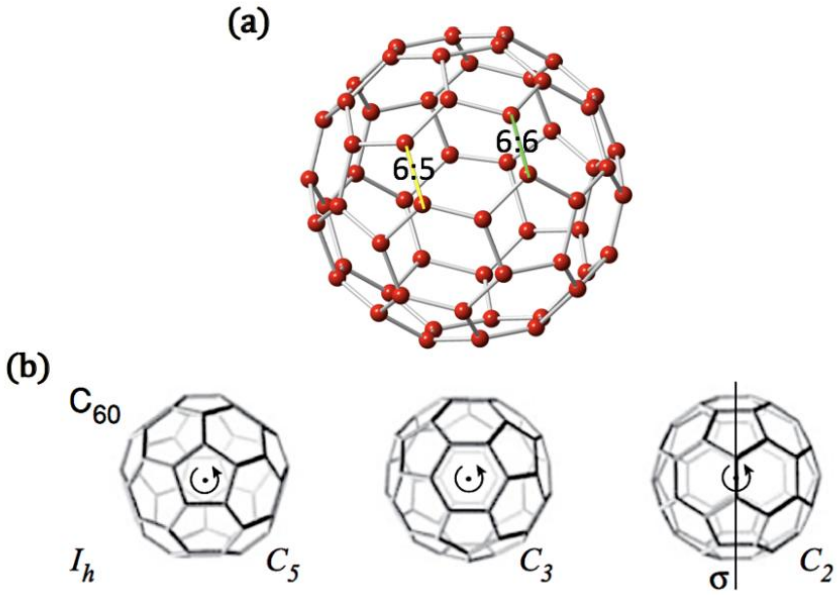

Fig. 2.21 (a) Ball-stick model of C_{60}. (b) Framework model of the C_{60} molecule, showing its symmetry. the C_{60} molecule belongs to Ih and has the symmetry operations C5, C3, C2 and the σ (inversion) which is not shown. [106]

C_{60} has the simplest molecular symmetry as the simplest fully closed fullerene. C_{60} has a spherical molecular cage consisting of 60 carbon atoms [102]. The molecule model of C_{60} is shown in Fig. 2.21(a) and consists of 20 hexagons (six atomic rings) and 12 pentagons (five atomic rings) [103]. C_{60} contains only two types of carbon-carbon bonds: a carbon-carbon double bond (denoted as a 6:6 bond) exists between two adjacent hexagons with an average bond length of 1.45 ± 0.015 Å and a

single carbon bond (denoted as a 6:5 bond) between the pentagonal and hexagonal rings. The single carbon bond is 0.05 Å longer than the double bond on average [104]. As shown in Fig. 2.21(b), C_{60} belongs to the full icosahedral point group in three dimensions, labelled Ih [105]. It has Ih symmetries that include the penta-, tri- and biaxial axes. For the C5 and C3 symmetries of the C_{60} molecule, a pentagonal and a hexagonal ring are observed along the rotation axis, respectively. For C2 symmetry, the C_{60} molecule rotates through a mirror that is vertical to the triple axis and divides the molecule to two equal parts.

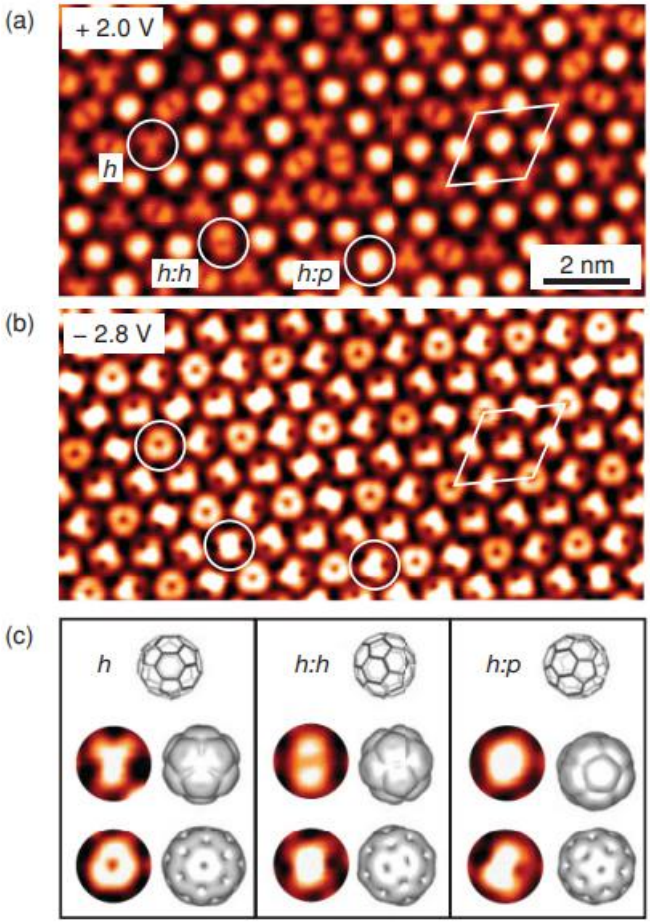

Fig. 2.22 High-resolution STM images of C_{60} on NaCl substrate. (a) Unoccupied molecular orbitals of C_{60}. (b) Occupied molecular orbitals of C_{60}. The white parallelogram in (a) and (b) shows a typical superstructure. (c)STM images and DFT calculated images of different C_{60} molecular orientations: h, h:h, h:p. The top images are lowest unoccupied (LUMO) and the bottom images are (HOMO). [106]

At RT, C_{60} molecules are able to display different orientations on HOPG substrates, with negligible changes in height during rotation [106]. On a metallic substrate, however, the C_{60} molecule shows three orientations, as shown in Fig. 2.22 (c), a hexagonal ring facing the scanning probe called h orientation, a 6:6 bond facing the probe called h:h orientation, and a 6:5 bond facing the probe called h:p orientation. As shown in Fig. 2.22 (a), the h:p orientation, h:h orientation and h orientation exhibit 1-fold, 2-fold and 3-fold symmetries respectively under high resolution STM imaging. HOMO-LUMO gap is the energy difference between a molecule's Highest energy Occupied Molecular Orbital (HOMO) and its Lowest energy Unoccupied Molecular Orbital (LUMO). The theoretical calculated value of this gap is 2.7eV [151]. In experiments, this value varies according to the different forms of C60 and various experimental equipment. The HOMO-LUMO gap of single C60 molecule in report is 2.7 eV by Scanning Tunneling Spectroscopy (STS) [107], and this value is of gas phase C_{60}^- in report is 2.5 eV by Ultraviolet Photoelectron Spectroscopy (UPS) [108], 2.3 eV of C_{60} film on Si (001) by ellipsometric measurements of the optical constants [109] and 1.9 eV of solid C_{60} by X-ray photoelectron spectroscopy (XPS) and Electron-Energy-Loss Spectroscopy (EELS) [110][111]. C_{60} deposited on precious metal substrates, such as Au (111) or Ag (111), is able to work as an electron acceptor. As a result, it results in a narrowing of the gap between HOMO and LUMO of the C_{60} molecule. Modesti et al. demonstrated that the fullerene films gradually change from metallic to semiconductor-like properties as the thickness increasing [112].

The physical diameter of C_{60} molecules in crystals is approximately 7.1 Å as measured by X-ray Photoelectron Spectroscopy (XPS) [111] and the van der Waals diameter of molecules in the gas phase is about 10.3 Å [102]. Solid C_{60} at room temperature usually exists as small dark crystals where the molecules are governed by van der Waals forces and the C_{60} crystals have an FCC structure. In contrast, the crystal structure of C_{60} changes with temperature. When they are at ultra-low

temperature of 5 K, the molecules have very low energy and lose their ability to change orientation by thermal motion. Each electron deficient phase in each C_{60} molecule is parallel to the electron rich bonding of its neighboring molecules and the C_{60} molecule is in an optimally stable structure. At this temperature, the C_{60} crystal is in a perfect simple cubic (SC) structure. The lattice constants of C_{60} crystals do not change significantly until they are heated to 90 K [114].

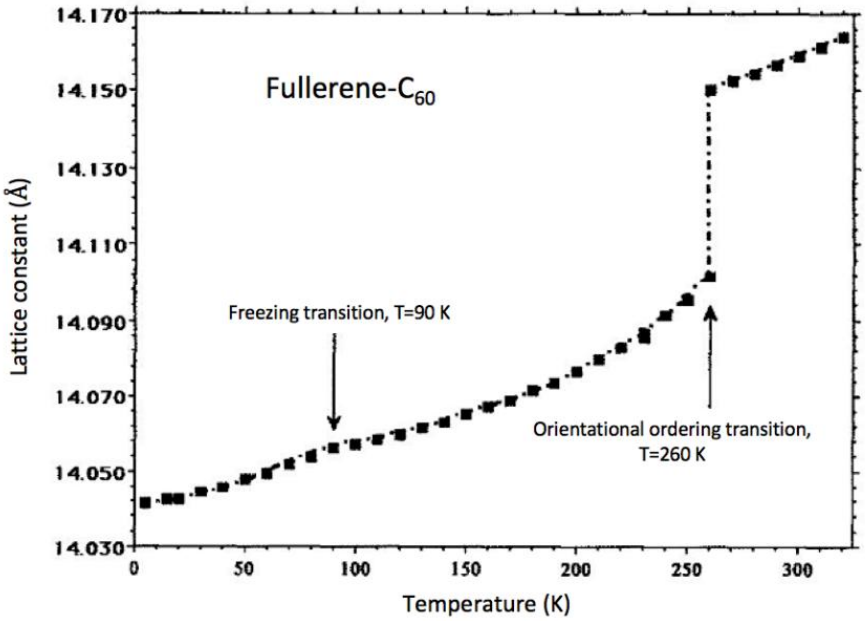

Fig. 2.24 Point profile showing the lattice constants of C_{60} crystal with respect to the temperature. Two phase transitions are indicated in the profile as the temperature increases from 5 K to 260 K. The freezing transitions happen at 90 K and there is an abrupt increase in the curve at 260 K as the phase changes from SC to FCC. [114]

As shown in Fig. 2.24, the freezing transition occurs when the temperature reaches 90 K. From 90 K to 260 K, the lattice constant of the C_{60} crystals increases slowly but remains below 14.110 Å. At this point, most of the C_{60} crystals still form a SC structure. When the lattice constant gradually increases with the temperature increases, C_{60} molecules can rotate in their positions, as the molecules gain thermal energy beyond their rotational barriers [114]. At 260 K, most molecules are able to rotate freely. The FCC and SC phases co-exist in C_{60} crystals. Abrupt jumps in lattice constants and

domain boundaries can be observed. C_{60} molecules will free to rotate and stack into FCC structures above 260 K.

2.4.2 Close-Packed C_{60} Islands on Au (111)

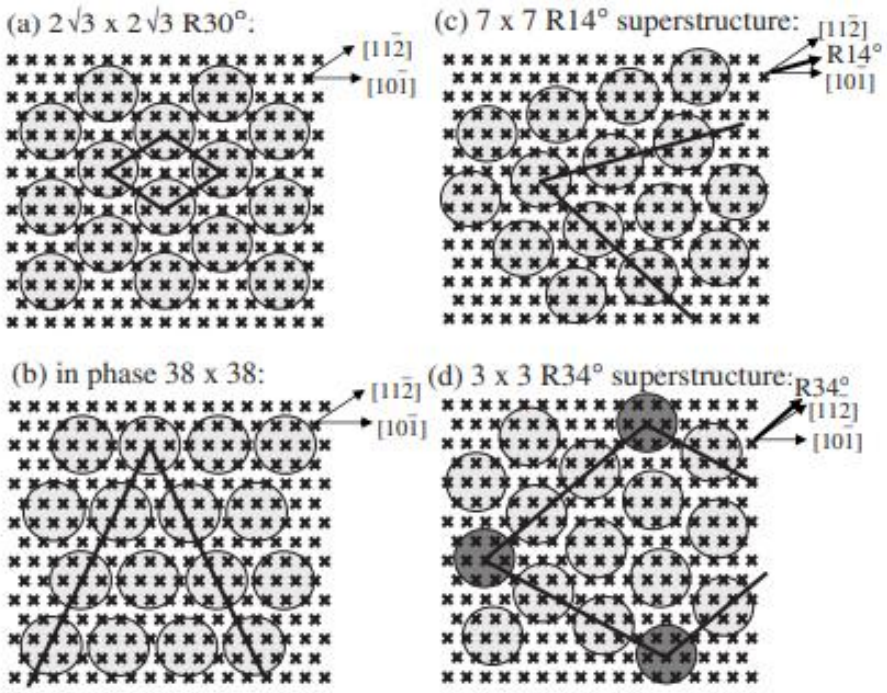

Fig. 2.25 Schematic diagram of C_{60} molecules in a close-packed arrangement on the surface of Au (111). The circles represent C_{60} and the crosses represent Au atoms. (a) (2√3 × 2√3) R30° phase. (b) (38 × 38) R0° phase. (c) Quasi-periodic (7 × 7) R14° phase. (d) (3 × 3) R34° superstructure with dark circles representing C_{60} that periodically occupy the same lattice sites. [60]

On Au (111) surface, C_{60} molecules nucleate at elbow sites and grow into large monolayer island. Theoretical calculations on the C_{60} form on Au (111) point to a covalent-like bonding at the interface between C_{60} and Au (111) with an ionic feature. [90][115] At RT, C60 are trapped by seven-atom pits at elbow sites. The adsorption energy of C60 at elbow sites is 2.56 eV by DFT calculation. [116] The adsorption energy of C60 on non-elbow sites is lower, the value by DFT calculation is 2.3 eV [117] and the experimental value by annealing desorption experiment is 1.9eV [118].

There are four different arrangements of C_{60} on Au (111). According to molecular

dynamics, C_{60} on gold surface will nucleate in {111} steps and grow into large domains along the step direction at room temperature. This phase is called 0 ° phase, because the C_{60} and gold atoms have the same arrangement orientations. As Fig. 2.25 (b) shown, the different sizes between the gold atoms and C_{60} results in a lattice mismatch, with 11 C_{60} molecules or 38 gold atoms in the close-packed direction as a cycle. Therefore, the phase is called (38×38) R0° or (38×38) in-phase structure. Such closely packed structures are also observed when C_{60} is deposited on other metal surfaces such as copper or nickel [119].

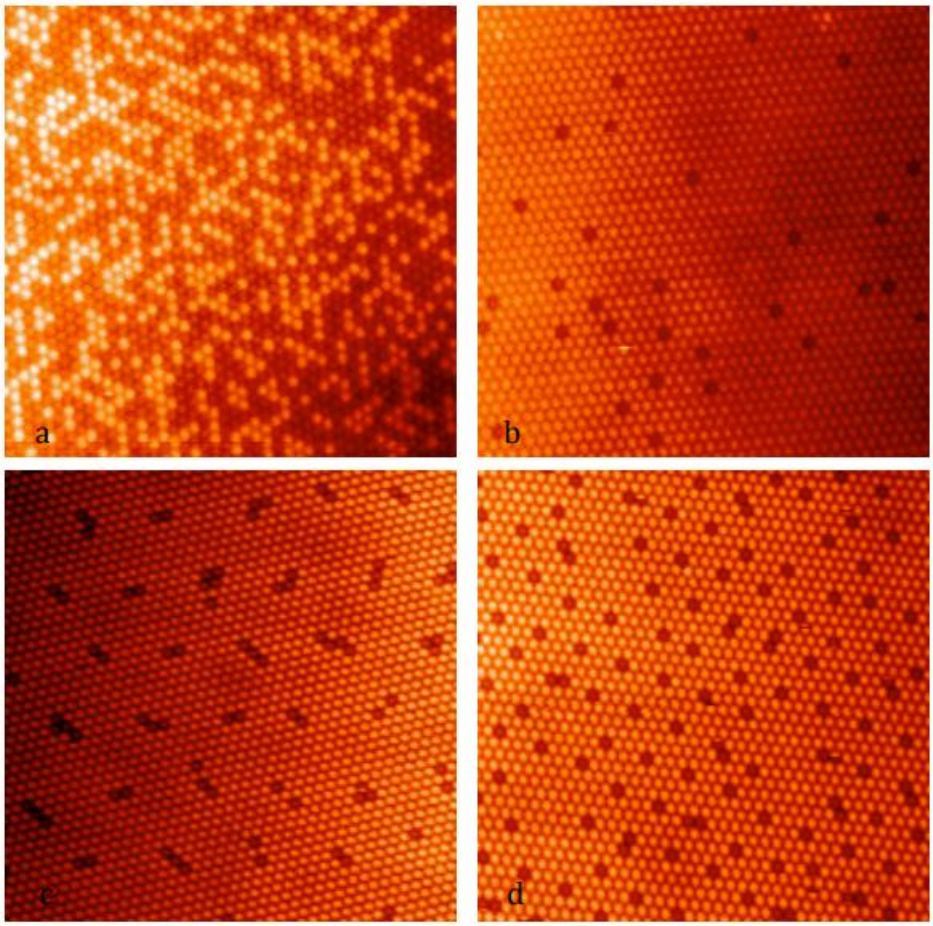

Fig. 2.26 Various C_{60} phases on the Au (111) surface. (a) The STM image of the (2√3 × 2√3) R30° phase, the light and dark of the C_{60} molecule alternate in a disordered and random arrangement. (b) The in-phase is both the R0° phase and the C_{60} monolayer has random independent dim molecules. (c) R14° phase with certain quasi-periodicity with (7 × 7) superstructure. (d) (3×3) R34° quasi-periodic phase. [120]

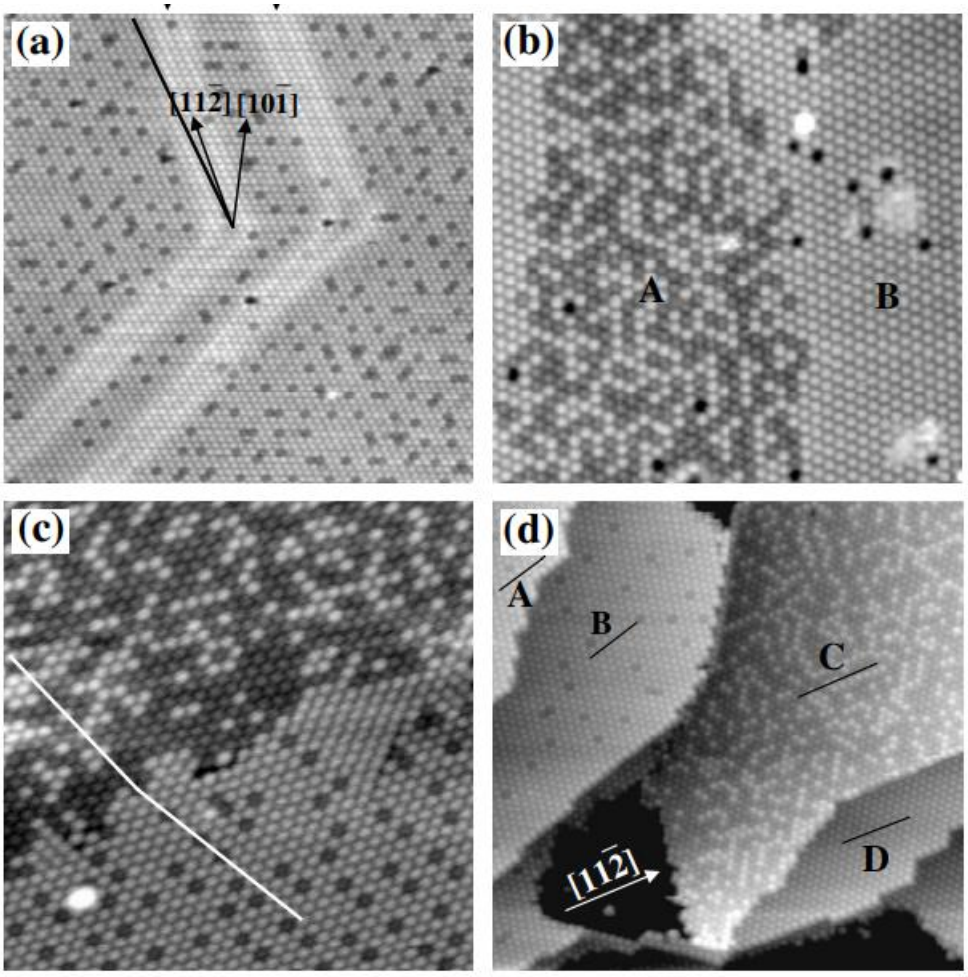

Fig. 2.27 STM images of various C_{60} monolayer phases, room temperature. (a) Quasi-periodic (3 × 3) R34° superstructure, unannealed. Black lines indicate C_{60} close-packed orientations. (b) Disordered domain A of the unannealed sample and uniform height domain B. (c) Two adjacent domains. The upper part is the disordered domain and the lower part is the quasi-periodic C_{60} array. 420 °C annealed. (d) A region of multiple Au terraces with their own distinct C_{60} structure domains, after annealing at 300 °C. The black line shows the close-packed orientation of the C_{60}. [60]

At high temperature, C_{60} prefer to fall at lower energy sites, both in the triple hollow site. It leads to a phase transition from R0° to (2√3 × 2√3) R30° [121]. In Fig. 2.25 (a), C_{60} molecules all occupy FCC or HCP sites on the Au (111) substrate, and stronger interactions are established between the C_{60} layer and the gold atoms. The

close-packed orientation of C_{60} is oriented at an angle of 30° to the gold atoms below, and the distance of the molecules is $2\sqrt{3}$ times of the gold atoms. Thus, the C_{60} molecule prefers the R30° structure to the R0° structure on thermodynamic. However, C_{60} covering the Au (111) can alter the gold surface. As shown in Fig. 2.26 (a), there are a large amount of irregular bright and dark molecules in the $(2\sqrt{3} \times 2\sqrt{3})$ R30° structure, so the $(2\sqrt{3} \times 2\sqrt{3})$ R30° phase is also called disordered phase. These dark molecules are caused by the nano-pits on the Au surface, because of some C_{60} being lower other molecules. This arrangement is beneficial for the transfer of charge from the Au (111) surface to the C60 molecules [60]. This close-packed structure is also observed when C_{60} are deposited on the other metal surfaces such as Cu or Ni. [119]

The (7×7) R14° superstructure, which was first discovered by R. Berendt et al. [122], has a 7×7 unit, as shown in Fig. 2.25(c), with the (7×7) R14° molecules rotated by 15° in the close-packed orientation of the Au atoms. The (3×3) R34° structure was first discovered by J. A. Gardener et al [60] and has a smaller 3×3 cell with a period of every three C_{60} molecules in the close-packed orientation and the first molecule will sit on the same gold atomic site as the fourth molecule. As shown in Fig. 2.26, the (7×7) R14° structure exhibits some quasi-periodicity, which is further enhanced by the (3×3) R34° structure. As shown in Fig. 2.27, several different phases of the C_{60} monolayer transform into each other mainly by annealing, but this transformation is not absolute. Multiple phases of gold can co-exist, they can be in the same gold plane, but also in different gold planes. [60]

2.4.3 Growth and Diffusion of C_{60} on Au (111)

There are two modes of C_{60} growth on Au (111): nucleation at the elbow sites and the formation of finger-like shapes at the steps. At room temperature, C_{60} molecules firstly form single molecule chains at the steps, which then widen, join and eventually form large islands. This was demonstrated in the work of Eric I. Altman by increasing the coverage of C_{60} [123]. And at low temperature, single C_{60} molecule is adsorbed at

the elbow sites under 30K, according to Fujita's work [124]. Whereas for multi-molecule C_{60} clusters, a study by Xin Zhang et al. demonstrated the nucleation and growth pattern of C_{60} molecules at elbow sites at low temperature [125]. For low temperature, C_{60} molecules' kinetic energy is not sufficient to pass through the potential barrier at the elbow sites. So, unlike at room temperature, they are trapped at the elbow sites and can't reach the step. Fig. 2.28 shows that on a sample scanning at 46 K with 0.01 ML C_{60} deposited, C_{60} clusters is observed in three different growth orientations: R0°, R14° and R30° phases. It is worth noting that small-size clusters are unstable and can change between three possible orientations under STM scanning. It's probably because, at low temperature, surface diffusion is inhibited and therefore the C_{60} molecules are not fully in the thermodynamically optimal position.

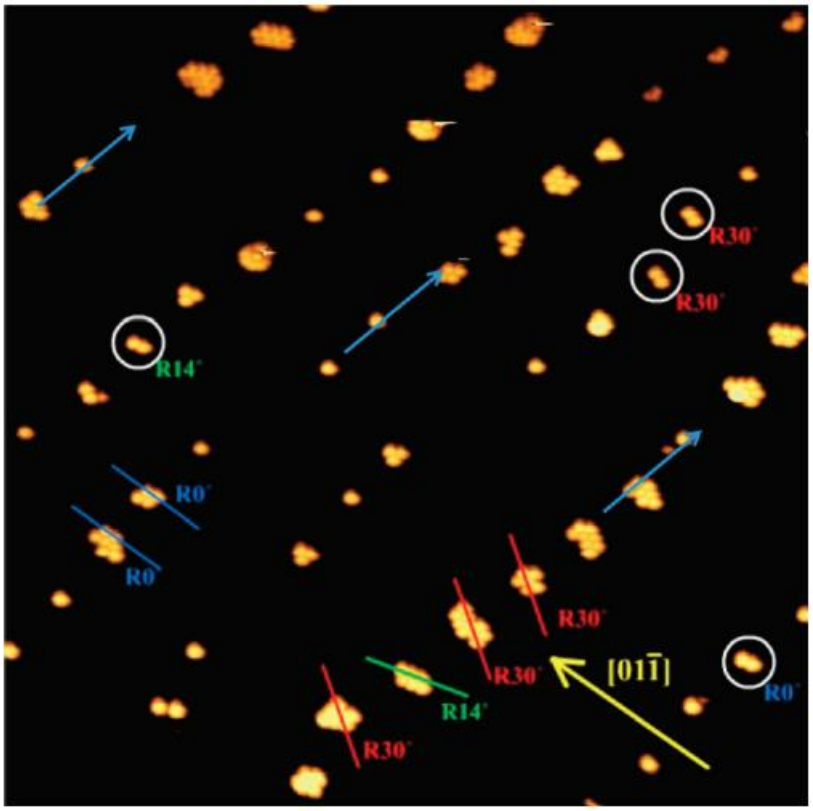

Fig. 2.28 STM image of 0.01 ML C_{60} deposited at 46 K on Au (111) surface, 80 nm × 80 nm. It is imaged at room temperature. The phase of each C_{60} cluster has been shown. Blue arrows indicate the orientation of the C_{60} clusters lined up at the elbow and yellow arrows indicate the DLs orientation. [125]

Also, for elbow sites, the C_{60} prefers to stay on the bulged elbow instead of the pinched elbow, and at 180 K this difference was amplified as the molecular capture rate at the bulged elbow increased. [125] As shown in Fig. 2.29, at 190 K, large monolayer islands of C_{60} were observed on the surface where 0.15 ML of C_{60} had been silenced. These islands arrange similarly to C_{60} islands at room temperature [126], but unlike at room temperature, these islands are not adjacent to any steps. Each bulged elbow has C_{60} molecules deposited on it, some as individual molecules and others as clusters. However, as shown in Fig. 2.29 (C), there is almost no molecular adsorption in the pinched elbow. All the clusters in Fig. 2.29 (A) are located at bulged elbow sites, which are fully R30° oriented.

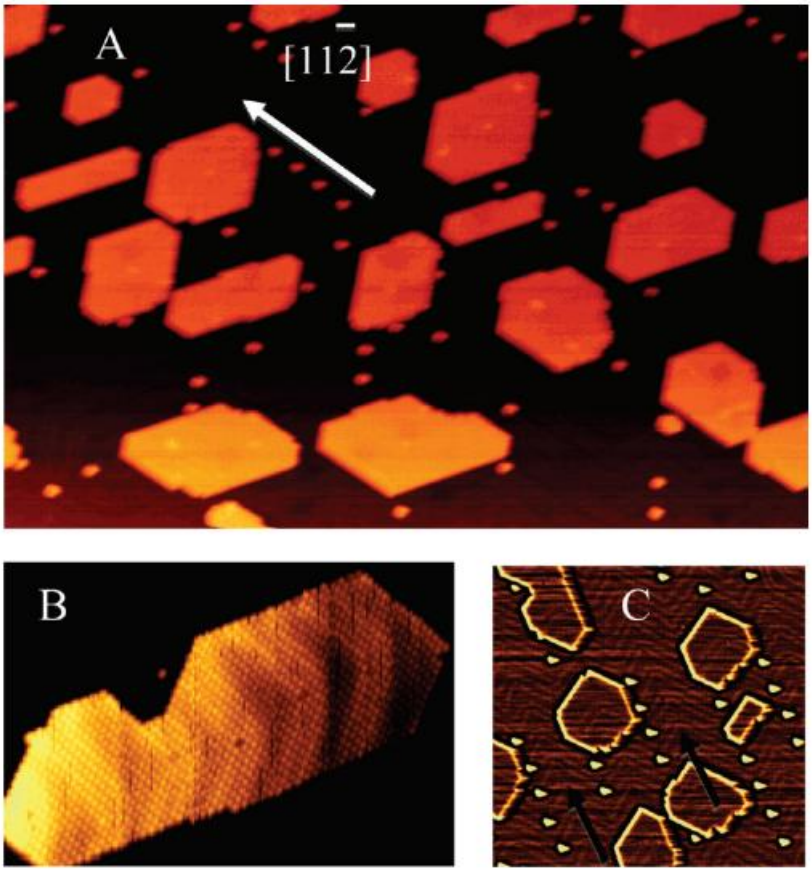

Fig. 2.29 (A) STM image of 0.15 ML C_{60} on Au (111) deposited at 190 K, 117 nm × 113 nm. (B) STM image of R30° orientation C_{60} cluster, 60 nm × 40 nm. The DLs can be seen through the monolayer. (C) STM image of C_{60} clusters scanning at 170 K. Clusters are all located at the

pinched elbows and bulged elbows are all empty. [125]

At room temperature, a single C_{60} molecule is extremely unstable on a gold surface [123], and slow diffusion of C_{60} molecules at the edges of C_{60} islands can be observed experimentally [127], contrary to C_{60} molecules at the center of the C_{60} islands which are very stable. This is because the C_{60}-C_{60} interaction belongs to the van der Waals potential and therefore the strength of the interaction between molecules depends on the neighboring C_{60} molecules [128-132]. More closely wrapped the C_{60} molecule is, more stable it will be. Thus, the center of an island with more neighboring molecules would also be more stable than those at the edge of the island. When the sample is heated, desorption will begin with the molecule at the farthest edge of the island, which is called the anchor molecule in Song Guo et al.'s study [127]. Once the anchor molecule leaves the edge, all its previous neighbors will become unstable due to the loss of neighbors. Further diffusion of unstable neighboring molecules will result in more unstable sites, and this C_{60} diffusion caused by the departure of the anchor molecule will develop exponentially. Conversely, the departing anchor molecule plays the role of a C_{60} island limiter. At the same time, due to the lattice mismatch between the C_{60} molecule and the substrate, C_{60} may fall on top, bridge and triplet site of the Au (111) substrate. Thus, the interaction of C_{60} with the gold atoms is anisotropic. For the 7×7 superstructure, the molecules are located at unequal surface positions, which may lead to additional maxima and minima potential enhancing diffusion. Whereas for the (2√3×2√3) R30° phase, all C_{60} are located at the equal sites and therefore it will show less diffusion.

2.5 Metal-C_{60} Complexes

The metal-organics combination, such as porphyrins or metals-C_{60} complexes, is an important object in surface science. In the NPRL laboratory from the University of Birmingham, surface self-assembly Au-C_{60} magic number clusters has been achieved at low temperature [133][134]. However, due to the features of STM, it is difficult to

characterize the interface of gold clusters wrapped by C_{60} by STM. At the same time, the stable chemical property of gold makes it difficult to expect further structure evolution of such clusters. In contrast, cobalt, as a ferromagnetic metal, is more easily detected than gold, by SQUID equipment [86]. Also, studies on the diffusion of C_{60} on cobalt surfaces have shown that the adsorption and diffusion of C_{60} on cobalt surfaces is the similar covalent-like bonding with an ionic features like C_{60} on gold surfaces [115], but stronger [135][136].

The presence of Cobalt-C_{60} units has been experimentally demonstrated in mixed Cobalt-C_{60} films manufactured by laser vaporization and molecular beam epitaxy methods [137-139]. There are also corresponding theoretical studies on the structure of Cobalt-C_{60} clusters [140]. The evolution of the C_{60} structure under cobalt catalysis is also an interesting phenomenon. On the Cobalt-C_{60} mixed films after annealing, the structure of graphene and diamond have been observed by Raman spectroscopy [141], which indirectly demonstrates the important role played by cobalt atoms in the structure evolution of the C_{60} cage.

2.5.1 Magic Number $(C_{60})_m$-$(Au)_n$ Clusters

At a low temperature of 110 K, the gold atoms deposited onto the Au (111) surface will form small-size clusters on the elbow sites, which are unstable compared to other metals. As the surface temperature rises to room temperature, the clusters will gradually disintegrate [133]. However, if the C_{60} molecules and gold atoms are deposited onto the gold surface in a 1:2 ratio at a temperature of 110 K, the gold clusters located at the elbow sites will be wrapped by C_{60} molecules. As the temperature gradually increases to room temperature, the gold clusters will stay at the elbow sites dues to the protection of the C_{60} molecules, and the excess C_{60} molecules will leave, leaving only a series of well-defined $(C_{60})_m$-$(Au)_n$ magic number clusters with a specific number of molecule/atom combinations[130]. As shown in Fig 2.30 (a), at 110 K, both gold atoms and C_{60} molecules appear at the elbow sites. However, at

this point, they are disordered arranged. At room temperature, the structure of the Au-C_{60} cluster is reordered to the cluster shown in Fig. 2.30 (b) which is a close-packed hexagonal C_{60} cluster with seven molecules. However, the center molecule is brighter than the others. According to the height information shown in Fig. 2.30 (c), there is a 0.21 nm height difference between the center molecule and the six surrounding molecules, which is approximate the height of monolayer gold cluster, pointing to an image of a regularized monolayer Au cluster, perfectly wrapped by seven C_{60} molecules.

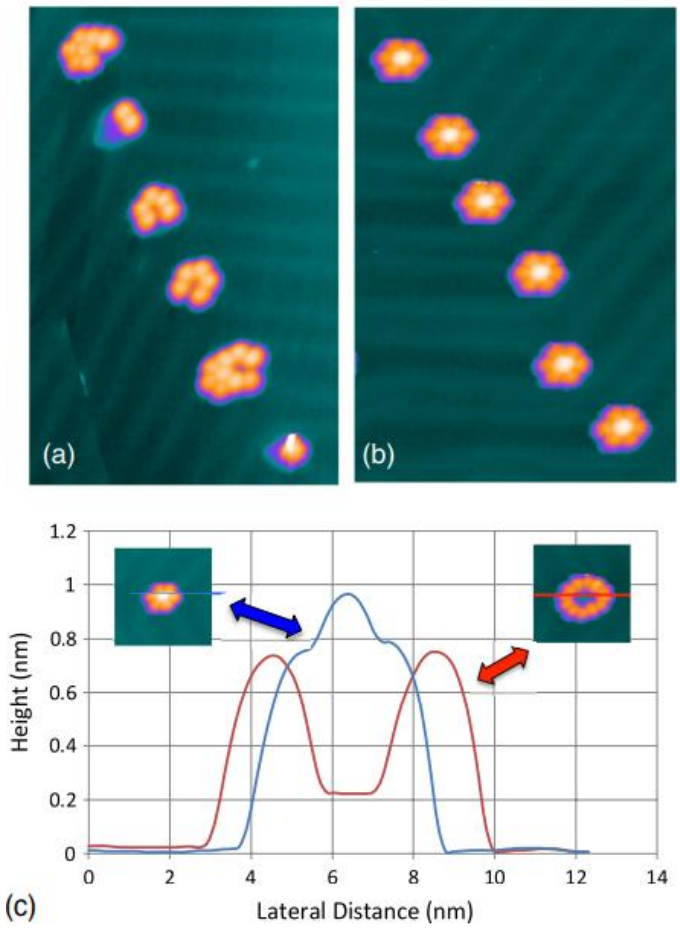

Fig. 2.30: (a) STM image of irregular Au-C_{60} clusters at 110 K, 25 nm × 40 nm. (b) Self-assembly $(C_{60})_7$-$(Au)_{19}$ clusters with a uniform orientation at room temperature. The image (b) is a different scanning region with (a). (c) Blue curve: height information of a $(C_{60})_7$-$(Au)_{19}$ cluster. Red curve: height information of a larger, C_{60} surrounding Au cluster. [134]

The most basic $(C_{60})_m$-$(Au)_n$ magic number cluster consists of seven C_{60} molecules with nineteen gold atoms as shown in Fig. 2.31(a) and (b). The six molecules surrounding the gold islands occupy three FCC sites. The mid molecule occupies the top position covering 19 Au atoms. The parallel distance of the Au cluster and C_{60} molecule is close to the calculated value of the Au-C distance of C_{60} on Au (111) [142]. The uniform contrast and height of these molecules all suggest that the six surrounding molecules sit on the substrate and do not involve atomic vacancies at the interface. Fig. 2.31 (c) and (d) then show the two larger magic number clusters of $(C_{60})_{10}$-$(Au)_{35}$ versus $(C_{60})_{12}$-$(Au)_{49}$.

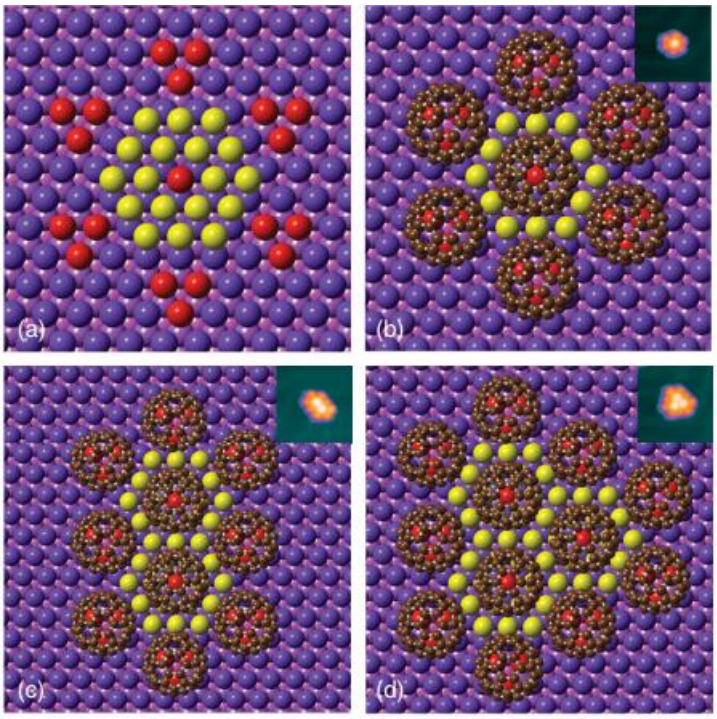

Fig. 2.31: (a) Ball model of the $(C_{60})_7$-$(Au)_{19}$ magic number cluster on Au (111) substrate. The red ball represents the gold atoms in contact with C_{60}, the yellow ball represents the gold atoms in contact with the gold cluster and the purple ball is the substrate. (b) A model of the C_{60} molecules has been added to (a). (c) Ball model of the $(C_{60})_{10}$-$(Au)_{35}$ magic number cluster. (d) Ball model of the $(C_{60})_{12}$-$(Au)_{49}$ magic number cluster. (b)-(d) The STM images of the corresponding structures are shown in the upper right corner. [134]

A 19-atom gold island located at the elbow site is already extremely unstable at 200 K. However, $(C_{60})_7$-$(Au)_{19}$ can remain stable at 400 K [134]. At the same time, the $(C_{60})_7$-$(Au)_{19}$ cluster is also very self-refining. Self-refinement, as used here, refers to the self-organized transition from a labile to a stable phase in the presence of thermal motion. Fig. 2.32 illustrates the gradual self-refinement of three Au-C_{60} clusters from completely different size, composition and orientation into three identical magic number clusters as the temperature increases. The upper cluster is surrounded by seven C_{60} molecules, which should contain more gold atoms. But at 310 K, one C_{60} comes to the top of the cluster and the extra gold atoms leave. For the central cluster, it has additional C_{60} molecules, but at 308 K these also depart. Only the magic number cluster below remains stable at all times. Eventually, at 310 K, three clusters of identical size, arrangement and orientation appear on the image, which demonstrates the $(C_{60})_7$-$(Au)_{19}$ magic number cluster's thermal stability. This stability is from the additional interaction between the C_{60} and the Au cluster. The wrapping C_{60} act as a protection layer for the covered Au cluster, and the Au cluster also prevents the molecules from escaping. This type of interaction is similar to metal-ligand coordination [143]. However, the interaction is not localized between a single metal atom and a specific ligand but a global optimization process involving all the molecules and the Au atoms in the cluster. Global optimization allows particles to refine their position to achieve the most stable state.

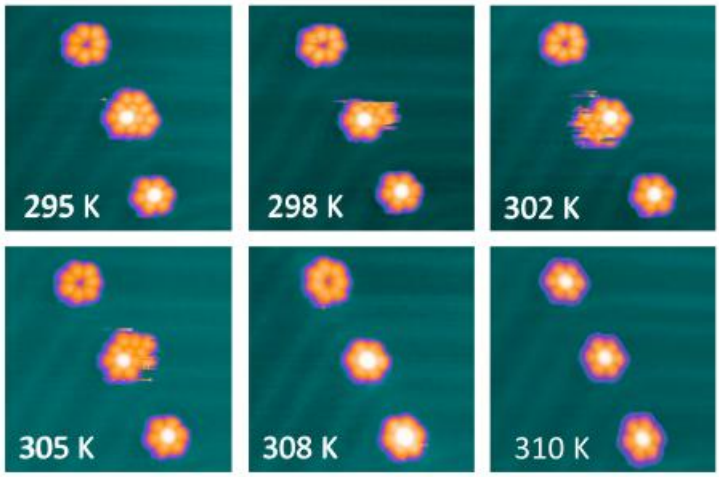

Fig. 2.32: Six STM images show the self-refinement towards the C_{60}-Au clusters. These six images are from the same region that are continuously imaging for 6 hours as the temperature is increased from 295 K to 310 K. [134]

However, the binding conditions between Au atoms and C_{60} molecules in the larger-size clusters are more complex than in the $(C_{60})_7$-$(Au)_{19}$ clusters. For example, in a $(C_{60})_{12}$-$(Au)_{49}$ cluster, there are three C_{60} molecules interacting with the V-step edge rather than in a straight line [134]. As a result, the stability of these larger size magic number clusters is weaker.

2.5.2 Cobalt-C_{60} Combination

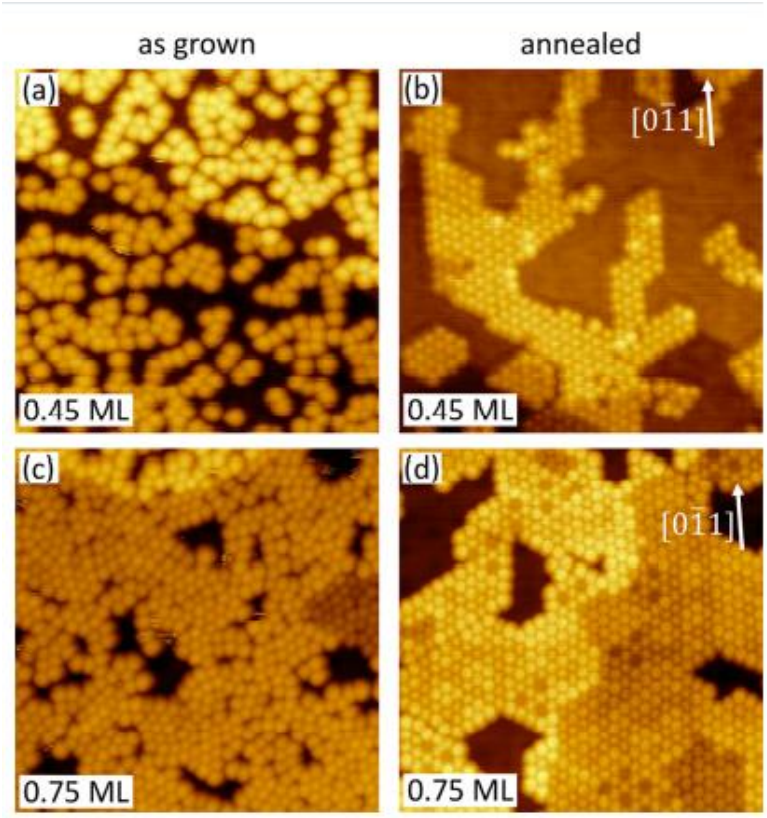

Fig. 2.33 RT STM images of C_{60} films with different coverage (0.45 ML and 0.75 ML) on Co/Au (111) before and after annealing 30 nm × 30 nm. Left images are unannealed sample and right images are annealed at 350°C 30 min. [135]

Unlike gold and C_{60} which can only be connected by van der Waals interactions, the

bond between cobalt and C_{60} is much stronger. For the C_{60} molecules deposited on the cobalt film, as shown in Fig. 2.33, the C_{60} molecules deposited on the cobalt film at room temperature show a more random arrangement, which indicates that the diffusion potential of C_{60} on cobalt is greater than that on the gold surface. Thus, C_{60} can hardly diffuse on the cobalt surface at RT. After 350°C annealing, C_{60} molecules will reorganize and show a close-packed phase. Unlike the unstable edges of the C_{60} islands on Au (111) surface [127], the C_{60} islands' edges on cobalt film are clear and stable.

The arrangement of the C_{60} molecules deposited on the cobalt surface shows several different surface arrangements [132]. As shown in Fig. 2.34 (a), most of the C_{60} molecules on the cobalt surface are in the R0° domain, another part is in the R15° domain, and a little C_{60} molecules are in the R30° domain. Fig. 2.34 (b) and (c) show the R0° and R15° domain layout models for the C_{60} molecule and the corresponding fast Fourier transform (FFT) images. The angular deflection in FFT images confirm the 15° relative angular relationship between the two domains on another hand. If the surface lattice constant of the cobalt film is a constant value (2.51 Å), then the R15° and R30° domains should not exist. It is inferred from the experimental data that a surface structure with lattice constants of 2.77 and 2.88 Å should exist on the Co film at the same time. This can be explained by the moiré-like reconstruction of the cobalt film after annealing. Similar phenomenon was observed when C_{60} was deposited on cobalt films on Ru (0001) substrates [136].

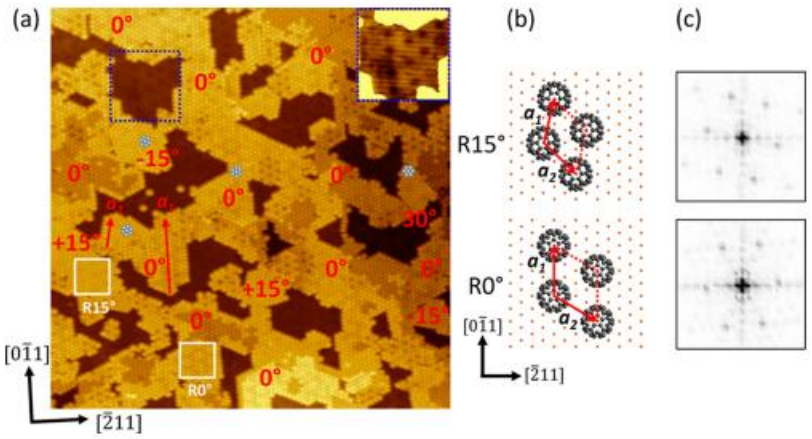

Fig. 2.34 (a) STM image of 0.75 ML C_{60} film on a cobalt substrate, 80 nm × 80 nm. The figure shows three domains of C_{60}, R0°, R15° and R30°. The blue boxed area on the top right corner (13 nm × 13 nm) shows the bare Co surface with the moiré-like superstructure. (b) Model of the molecular arrangement of R0° versus R15°. (c) FFT image corresponding to R0° and R15°. [135]

For more thorough contact of the cobalt atoms and C_{60} molecules, the situation is different again. Much effort has long been spent on modifying the structure of the fullerene cage by additional atoms [144-146]. Amongst these, the outer body transition metal-C_{60} is a widely studied classification, such as the Cobalt-C_{60} structure. A time-of-flight mass spectrometry study of cobalt-C_{60} mixtures manufactured by molecular beam methods and laser vaporization was investigated by Tsuyoshi Kurikawa et al [138], resulting in a ratio of C_{60} to cobalt in Co-C_{60} units. The cobalt-C60 mixtures consist of several major components such as (1,1), which represents a unit consisting of one cobalt atom with three C_{60} molecules, and (1,2) (1,3) (2,4) (3,4) (4,4), (1,3) and so on. Tsuyoshi Kurikawa et al have thus given a possible structure model for a Cobalt-C_{60} unit as in Fig. 2.35 and suggest that the (4, 4) tetrahedral structure in Fig. 2.35 (d) is a stable state. However, by Hoffmann et al's calculation [147], there is another possibility of the (4,4) cluster: the triangular pyramidal Co_4 is the stability of Co clusters in C_{60} bulk and is inside of the triangular cone of $(C_{60})_4$ where the Co_4 cluster's 4 vertices point to the 4 outer vertices of the triangular cone of $(C_{60})_4$. This theory predates the work of Tsuyoshi Kurikawa et al. However, this tetrahedral structure is not compatible with the large number of (1,3)

units and non (3,3) units are observed experimentally. Therefore, this structure is not adopted by Tsuyoshi Kurikawa et al.

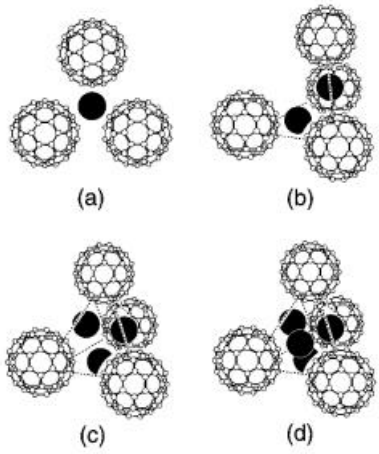

Fig. 2.35 Possible structures of Cobalt-C_{60} units. (a) $Co_1(C_{60})_3^+$, (b) $Co_2(C_{60})_4^+$, (c) $Co_3(C_{60})_4^+$, (d) $Co_4(C_{60})_4^+$. [138]

Although C_{60} consists of pentagons and hexagons rings, there is much evidence that C_{60} does not shown as an η5- or η6- ligand in Co-C_{60} complexes [138][140]. The η is usually used to indicate the number of carbon atoms are bound to metal atoms in the ring. The η2 and η'2 ligands are most common in the Co-C_{60} units, as demonstrated by calculations by Pavel Avramov et al [140]. Where η2 means that the cobalt atom is bound to two carbon atoms on (6:6) side of the C_{60} cage, and η'2 means that the cobalt atom is bound to two carbon atoms on (6:5) side of the C_{60} cage. During chemical synthesis, η′2 and η5 type structures or hybrid structures can be realized as high energy isomers and intermediate states in complex Co_x/C_{60} mixtures [140].

2.5.3 C_{60} Structure Evolution

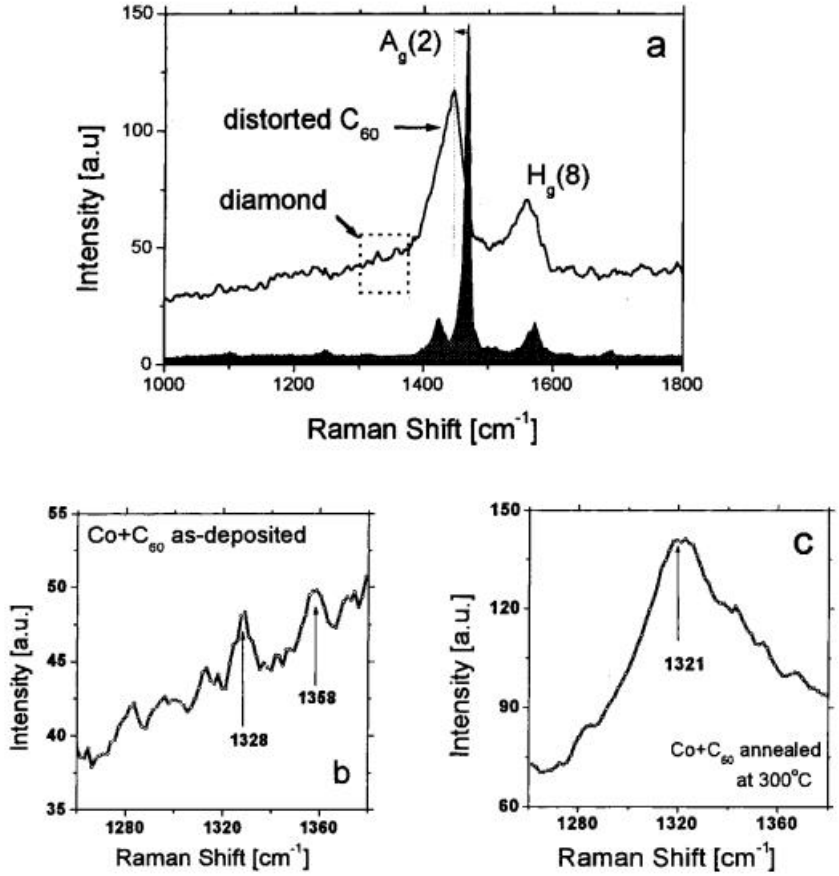

Fig. 2.36 (a) Raman spectrum of Co-C_{60} mixtures and C_{60} film both deposited on (0001) α-Al_2O_3 at RT. The black spectrum represents pure C60 film. (b) Spectrum of unannealed sample near the diamond peak. (c) Spectrum of the sample after 300°C annealing for 2 hours.[141]

Experiments have shown that the significant chemical relationship between Co and C_{60} may lead to the fragmentation of C_{60} molecules. In the study by V. Lavrentiev et al [141], there are not only C_{60} molecules but other carbon phase of peaks in the Raman spectra of Co-C_{60} mixtures film at UHV. Fig. 2.36 (a) shows the Raman spectrum of the Co-C_{60} mixtures film. C_{60} film's Raman spectrum is also given as control. The dominant C_{60} vibrational modes (Ag (2) and Hg (8)) in the spectra prepared from the blends confirm that C_{60} molecules are still the most dominant carbon structure in the mixed films. The widening of the C_{60} peak suggests that the molecules in the mixture may be deformed by the polymerization of C_{60} [148]. The downward shift of the C_{60}

peak (~24 cm^{-1}) signifies that electrons transfer from C_{60} to the cobalt cluster [102].

As shown in Fig. 2.36 (b), a detailed investigation of the Raman spectra of the mixture showed that there is a small peak at 1328 cm^{-1} close to the position of diamond peak (1333 cm^{-1}). This peak is point to a nanoscale fragment of diamond-structured carbon [149]. The concomitant peak at 1358 cm^{-1} reflects the possible stretching of the diamond crystals [150]. In contrast, after 300 °C annealing for 2 hours, the intensity of the diamond peak increased greatly and shifted to the 1321 cm^{-1}, indicating the apparent appearance of new diamond phase, as shown in Fig. 2.36 (c). The appearance of the diamond phase was interpreted as broken C fragments thermodynamically aggregated into diamond layers by the proper crystallographic arrangement of Co crystals around the cobalt clusters. Eventually, these form Co nanocrystals encapsulated by diamond. This experiment reveals the possibility of the evolution of C_{60} molecules into other carbon structures catalyzed by cobalt.

References

[1] Rohrer, H. (1990). Scanning Tunneling Microscopy—Methods and Variations. In *Scanning Tunneling Microscopy and Related Methods* (pp. 1-25). Springer, Dordrecht.

[2] Uchida, H., Huang, D. H., Yoshinobu, J., & Aono, M. (1993). Single-atom manipulation on the Si (111) 7× 7 surface by the scanning tunneling microscope (STM). *Surface science*, *287*, 1056-1061.

[3] Stipe, B. C., Rezaei, M. A., & Ho, W. (1998). Single-molecule vibrational spectroscopy and microscopy. *Science*, *280*(5370), 1732-1735.

[4] https://refubium.fu-berlin.de/bitstream/handle/fub188/7983/01_chapter1.pdf?sequence=2&isAllowed=y

[5] Bardeen, J. (1961). Tunnelling from a many-particle point of view. *Physical review letters*, *6*(2), 57.

[6] Tersoff, J., & Hamann, D. R. (1985). Theory of the scanning tunneling microscope. *Physical Review B*, *31*(2), 805.

[7] Coombs, J. H., & Pethica, J. B. (1986). Properties of vacuum tunneling currents: anomalous barrier heights. *IBM journal of research and development*, *30*(5), 455-459.

[8] Gomer, R. (1986). Possible mechanisms of atom transfer in scanning tunneling microscopy. *IBM journal of research and development*, *30*(4), 428-430.

[9] Quate, C. F. (1990). Surface modification with the STM and the AFM. *In Scanning Tunneling Microscopy and related methods* (pp. 281-297). Springer, Dordrecht.

[10] Eigler, D. M., & Schweizer, E. K. (1990). Positioning single atoms with a scanning tunnelling microscope. *Nature*, *344*(6266), 524-526.

[11] Stroscio, J. A., & Eigler, D. M. (1991). Atomic and molecular manipulation with the scanning tunneling microscope. *Science, 254*(5036), 1319-1326.

[12] Hla, S. W. (2014). Atom-by-atom assembly. *Reports on Progress in Physics*, 77(5), 056502.

[13] Gauthier, S. (2000). Atomic and molecular manipulations of individual adsorbates by STM. *Applied Surface Science, 164*(1-4), 84-90.

[14] Stipe, B. C., Rezaei, M. A., Ho, W., Gao, S., Persson, M., & Lundqvist, B. I. (1997). Single-molecule dissociation by tunneling electrons. *Physical review letters, 78*(23), 4410.

[15] Hla, S. W., Meyer, G., & Rieder, K. H. (2003). Selective bond breaking of single iodobenzene molecules with a scanning tunneling microscope tip. *Chemical physics letters, 370*(3-4), 431-436.

[16] https://en.wikipedia.org/wiki/Lennard-Jones_potential

[17] Hla, S. W., Braun, K. F., & Rieder, K. H. (2003). Single-atom manipulation mechanisms during a quantum corral construction. *Physical Review B, 67*(20), 201402.

[18] Eigler, D. M., Lutz, C. P., & Rudge, W. E. (1991). An atomic switch realized with the scanning tunnelling microscope. *Nature, 352*(6336), 600-603.

[19] Bartels, L., Meyer, G., & Rieder, K. H. (1997). Controlled vertical manipulation of single CO molecules with the scanning tunneling microscope: A route to chemical contrast. *Applied Physics Letters, 71*(2), 213-215.

[20] Bartels, L., Meyer, G., Rieder, K. H., Velic, D., Knoesel, E., Hotzel, A., ... & Ertl, G. (1998). Dynamics of electron-induced manipulation of individual CO molecules on Cu (111). *Physical*

Review Letters, 80(9), 2004.
[21]Tsong, T. T. (1991). Effects of an electric field in atomic manipulations. *Physical Review* B, 44(24), 13703.
[22]Saenz, J. J., & Garcia, N. (1993). Quantum atom switch: Tunneling of Xe atoms. *In Nanosources and Manipulation of Atoms Under High Fields and Temperatures: Applications* (pp. 229-237). Springer, Dordrecht.
[23]Salam, G. P., Persson, M., & Palmer, R. E. (1994). Possibility of coherent multiple excitation in atom transfer with a scanning tunneling microscope. *Physical Review B, 49*(15), 10655.
[24] Walkup, R. E., Newns, D. M., & Avouris, P. (1993). Role of multiple inelastic transitions in atom transfer with the scanning tunneling microscope. *Physical Review B, 48*(3), 1858.
[25] Koetter, E., Drakova, D., & Doyen, G. (1996). Role of the tip atom in STM and AFM: Theory of atom transfer. *Physical Review B, 53*(24), 16595.
[26] Hla, S. W., Meyer, G., & Rieder, K. H. (2001). Inducing single-molecule chemical reactions with a UHV-STM: A new dimension for nano-science and technology. *ChemPhysChem*, *2*(6), 361-366.
[27] Xie, Y., Liu, Q., Zhang, P., Zhang, W., Wang, S., Zhuang, M., ... & Zhuang, J. (2008). Reliable lateral and vertical manipulations of a single Cu adatom on a Cu (111) surface with multi-atom apex tip: semiempirical and first-principles simulations. *Nanotechnology, 19*(33), 335710.
[28] Gadzuk, J. W. (1995). Resonance-assisted, hot-electron-induced desorption. *Surface science, 342*(1-3), 345-358.
[29] Deshpande, A., Felix Braun, K., & Hla, S. W. (2011). Determination of chemical specific atomic interaction with scanning tunneling microscope. *Applied Physics Letters, 99*(22), 221902.
[30] Haiss, W., Lackey, D., Sass, J. K., & Besocke, K. H. (1991). Atomic resolution scanning tunneling microscopy images of Au (111) surfaces in air and polar organic solvents. *The Journal of chemical physics, 95*(3), 2193-2196.
[31] Tanishiro, Y., Kanamori, H., Takayanagi, K., Yagi, K., & Honjo, G. (1981). UHV transmission electron microscopy on the reconstructed surface of (111) gold: I. General features. *Surface Science, 111*(3), 395-413.
[32] Heyraud, J. C., & Metois, J. J. (1980). Anomalous 13 422 diffraction spots from {111} flat gold crystallites:(111) surface reconstruction and moiré fringes between the surface and the bulk. *Surface Science, 100*(3), 519-528.
[33] Yagi, K., Takayanagi, K., Kobayashi, K., Osakabe, N., Tanishiro, Y., & Honjo, G. (1979). Surface study by an UHV electron microscope. *Surface Science, 86*, 174-181.
[34] Perdereau, J., Biberian, J. P., & Rhead, G. E. (1974). Adsorption and surface alloying of lead monolayers on (111) and (110) faces of gold. *Journal of Physics F: Metal Physics, 4*(5), 798.
[35] Nakai, Y., Zei, M. S., Kolb, D. M., & Lehmpfuhl, G. (1984). A LEED and RHEED investigation of Cu on Au (111) in the underpotential region. *Berichte der Bunsengesellschaft für physikalische Chemie, 88*(4), 340-345.
[36] Melle, H., & Menzel, E. (1978). Superstructures on spherical gold crystals. *Zeitschrift für Naturforschung A, 33*(3), 282-289.
[37] Harten, U., Lahee, A. M., Toennies, J. P., & Wöll, C. (1985). Observation of a soliton reconstruction of Au (111) by high-resolution helium-atom diffraction. *Physical Review Letters, 54*(24), 2619.

[38] Wöll, C., Chiang, S., Wilson, R. J., & Lippel, P. H. (1989). Determination of atom positions at stacking-fault dislocations on Au (111) by scanning tunneling microscopy. *Physical Review B, 39*(11), 7988.
[39] Barth, J. V., Brune, H., Ertl, G., & Behm, R. J. (1990). Scanning tunneling microscopy observations on the reconstructed Au (111) surface: Atomic structure, long-range superstructure, rotational domains, and surface defects. *Physical Review B, 42*(15), 9307.
[40] "Crystal Structure of Gold" *https://www.webelements.com/gold/*
[41] Gao, Y. J., Deng, Q. Q., Huang, L. L., Ye, L., Wen, Z. C., & Luo, Z. R. (2017). Atomistic modeling for mechanism of crack cleavage extension on nano-scale. *Computational Materials Science, 130*, 64-75.
[42] Martínez-Alonso, C., Guevara-Vela, J. M., & LLorca, J. (2021). The effect of elastic strains on the adsorption energy of H, O, and OH in transition metals. *Physical Chemistry Chemical Physics, 23*(37), 21295-21306.
[43] Rousset, S., Repain, V., Baudot, G., Garreau, Y., & Lecoeur, J. (2003). Self-ordering of Au (111) vicinal surfaces and application to nanostructure organized growth. *Journal of Physics: Condense*d Matter, 15(47), S3363.
[44] Giesen, M., Steimer, C., & Ibach, H. (2001). What does one learn from equilibrium shapes of two-dimensional islands on surfaces?. *Surface Science, 471*(1-3), 80-100.
[45] Repain, V., Berroir, J. M., Rousset, S., & Lecoeur, J. (1999). Interaction between steps and reconstruction on Au (111). *EPL (Europhysics Letters), 47*(4), 435.
[46] Repain, V., Berroir, J. M., Rousset, S., & Lecoeur, J. (2000). Reconstruction, step edges and self-organization on the Au (111) surface. *Applied surface science, 162*, 30-36.
[47] Takayanagi, K., & Yagi, K. (1983). Monatom-high level electron microscopy of metal surfaces. *Transactions of the Japan institute of metals, 24*(6), 337-348.
[48] Takeuchi, N., Chan, C. T., & Ho, K. M. (1991). Au (111): A theoretical study of the surface reconstruction and the surface electronic structure. *Physical Review B*, *43*(17), 13899.
[49] Besenbacher, F., Lauritsen, J. V., Linderoth, T. R., Lægsgaard, E., Vang, R. T., & Wendt, S. (2009). Atomic-scale surface science phenomena studied by scanning tunneling microscopy. *Surface Science, 603*(10-12), 1315-1327.
[50] Schaff, O., Schmid, A. K., Bartelt, N. C., de la Figuera, J., & Hwang, R. Q. (2001). In-situ STM studies of strain-stabilized thin-film dislocation networks under applied stress. *Materials Science and Engineering: A, 319*, 914-918.
[51] Narasimhan, S., & Vanderbilt, D. (1992). Elastic stress domains and the herringbone reconstruction on Au (111). *Physical review letters, 69*(10), 1564.
[52] Tartaglino, U., Tosatti, E., Passerone, D., & Ercolessi, F. (2002). Bending strain-driven modification of surface reconstructions: Au (111). *Physical Review B, 65*(24), 241406.
[53] Hasegawa, Y., & Avouris, P. (1992). Manipulation of the reconstruction of the Au (111) surface with the STM. *Science, 258*(5089), 1763-1765.
[54] Huang, K. G., Gibbs, D., Zehner, D. M., Sandy, A. R., & Mochrie, S. G. J. (1990). Phase behavior of the Au (111) surface: Discommensurations and kinks. *Physical review letters, 65*(26), 3313.
[55] Sandy, A. R., Mochrie, S. G. J., Zehner, D. M., Huang, K. G., & Gibbs, D. (1991). Structure and phases of the Au (111) surface: X-ray-scattering measurements. *Physical Review B, 43*(6), 4667.

[56] Kowalczyk, P., Kozlowski, W., Klusek, Z., Olejniczak, W., & Datta, P. K. (2007). STM studies of the reconstructed Au (1 1 1) thin-film at elevated temperatures. *Applied surface science, 253*(10), 4715-4720.
[57] Tao, N. J., & Lindsay, S. M. (1991). Observations of the 22×√ 3 reconstruction of Au (111) under aqueous solutions using scanning tunneling microscopy. *Journal of applied physics, 70*(9), 5141-5143.
[58] Gimzewski, J. K., Modesti, S., Gerber, C., & Schlittler, R. R. (1993). Observation of a new Au (111) reconstruction at the interface of an adsorbed C_{60} overlayer. *Chemical physics letters, 213*(3-4), 401-406.
[59] Altman, E. I., & Colton, R. J. (1993). The interaction of C_{60} with noble metal surfaces. *Surface science, 295*(1-2), 13-33.
[60] Gardener, J. A., Briggs, G. A. D., & Castell, M. R. (2009). Scanning tunneling microscopy studies of c 60 monolayers on au (111). *Physical Review B, 80*(23), 235434.
[61] Barth, J. V., Behm, R. J., & Ertl, G. (1994). Mesoscopic structural transformations of the Au (111) surface induced by alkali metal adsorption. *Surface science, 302*(3), L319-L324.
[62] Corso, M., Verstraete, M. J., Schiller, F., Ormaza, M., Fernández, L., Greber, T., ... & Ortega, J. E. (2010). Rare-earth surface alloying: a new phase for GdAu 2. *Physical review letters, 105*(1), 016101.
[63] Electronegativities of the elements (data page) Electronegativities of the elements (data page) - Wikipedia
[64] Chambliss, D. D., Wilson, R. J., & Chiang, S. (1991). Ordered nucleation of Ni and Au islands on Au (111) studied by scanning tunneling microscopy. *Journal of Vacuum Science & Technology B: Microelectronics and Nanometer Structures Processing, Measurement, and Phenomena, 9*(2), 933-937.
[65] Padovani, S., Scheurer, F., & Bucher, J. P. (1999). Burrowing self-organized cobalt clusters into a gold substrate. *EPL (Europhysics Letters), 45*(3), 327.
[66] Cullen, W. G., & First, P. N. (1999). Island shapes and intermixing for submonolayer nickel on Au (111). *Surface science, 420*(1), 53-64.
[67] Voigtländer, B., Meyer, G., & Amer, N. M. (1991). Epitaxial growth of Fe on Au (111): a scanning tunneling microscopy investigation. *Surface Science Letters, 255*(3), L529-L535.
[68] Fischer, B., Barth, J. V., Fricke, A., Nedelmann, L., & Kern, K. (1997). Growth and surface alloying of Al on Au (111) at room temperature. *Surface science, 389*(1-3), 366-374.
[69] Dovek, M. M., Lang, C. A., Nogami, J., & Quate, C. F. (1989). Epitaxial growth of Ag on Au (111) studied by scanning tunneling microscopy. *Physical Review B, 40*(17), 11973.
[70] Ullmann, R., Will, T., & Kolb, D. M. (1993). Nanoscale decoration of Au (111) electrodes with Cu clusters by an STM. *Chemical physics letters, 209*(3), 238-242.
[71] Lang, C. A., Dovek, M. M., Nogami, J., & Quate, C. F. (1989). Au (111) autoepitaxy studied by scanning tunneling microscopy. *Surface Science Letters, 224*(1-3), L947-L955.
[72] Oviedo, O. A., Leiva, E. P. M., & Mariscal, M. M. (2008). Diffusion mechanisms taking place at the early stages of cobalt deposition on Au (111). *Journal of Physics: Condensed Matter, 20*(26), 265010.
[73] Meyer, J. A., Baikie, I. D., Kopatzki, E., & Behm, R. J. (1996). Preferential island nucleation at the elbows of the Au (111) herringbone reconstruction through place exchange. *Surface science, 365*(1), L647-L651.

[74] Casari, C. S., Foglio, S., Siviero, F., Bassi, A. L., Passoni, M., & Bottani, C. E. (2009). Direct observation of the basic mechanisms of Pd island nucleation on Au (111). *Physical Review B, 79(*19), 195402
[75] Helveg, S., Lauritsen, J. V., Lægsgaard, E., Stensgaard, I., Nørskov, J. K., Clausen, B. S., ... & Besenbacher, F. (2000). Atomic-scale structure of single-layer MoS 2 nanoclusters. *Physical review letters, 84*(5), 951.
[76] Haag, N., Laux, M., Stöckl, J., Kollamana, J., Seidel, J., Großmann, N., ... & Aeschlimann, M. (2016). Epitaxial growth of thermally stable cobalt films on Au (111). *New Journal of Physics, 18*(10), 103054.
[77] de Boeck, J., & Borghs, G. (1999). Magnetoelectronics. *Physics World, 12*(4), 27.
[78] Doudin, B., & Ansermet, J. P. (1997). Nanostructuring materials for spin electronics. *Europhysics news, 28*(1), 14-17.
[79] Kingetsu, T., & Sakai, K. (1993). Growth-temperature dependence of Co layer strain and magnetic anisotropy in epitaxial Co/Au superlattices. *Journal of applied physics, 74*(10), 6308-6312.
[80] Renard, D., & Nihoul, G. (1987). Crystal structure of a magnetic cobalt layer deposited on a (111) gold surface determined by transmission electron microscopy. *Philosophical Magazine B, 55*(1), 75-86.
[81] Chappert, C., Le Dang, K., Beauvillain, P., Hurdequint, H., & Renard, D. (1986). Ferromagnetic resonance studies of very thin cobalt films on a gold substrate. *Physical Review B, 34*(5), 3192.
[82] Tölkes, C., Zeppenfeld, P., Krzyzowski, M. A., David, R., & Comsa, G. (1997). Preparation of well-ordered cobalt nanostructures on Au (111). *Physical Review B, 55*(20), 13932.
[83] Voigtländer, B., Meyer, G., & Amer, N. M. (1991). Epitaxial growth of thin magnetic cobalt films on Au (111) studied by scanning tunneling microscopy. *Physical Review B, 44*(18), 10354.
[84] Speckmann, M., Oepen, H. P., & Ibach, H. (1995). Magnetic domain structures in ultrathin Co/Au (111): on the influence of film morphology. *Physical review letters, 75*(10), 2035.
[85] Chado, I., Padovani, S., Scheurer, F., & Bucher, J. P. (2000). Controlled nucleation of Co clusters on Au (111): towards spin engineering. *Applied surface science, 164*(1-4), 42-47.
[86] Padovani, S., Chado, I., Scheurer, F., & Bucher, J. P. (1999). Transition from zero-dimensional superparamagnetism to two-dimensional ferromagnetism of Co clusters on Au (111). *Physical Review B, 59*(18), 11887.
[87] Cagnon, L., Devolder, T., Cortès, R., Morrone, A., Schmidt, J. E., Chappert, C., & Allongue, P. (2001). Enhanced interface perpendicular magnetic anisotropy in electrodeposited Co/Au (111) layers. *Physical Review B, 63*(10), 104419.
[88] Repain, V., Berroir, J. M., Rousset, S., & Lecoeur, J. (2000). Growth of self-organized cobalt nanostructures on Au (111) vicinal surfaces. *Surface science*, *447*(1-3), L152-L156.
[89] Wollschläger, J., & Amer, N. M. (1992). Heterogeneous nucleation and epitaxial growth of Au on the Co decorated Au (111) surface investigated by scanning tunneling microscopy. *Surface science*, *277*(1-2), 1-7.
[90] Wang, L. L., & Cheng, H. P. (2004). Density functional study of the adsorption of a C 60 monolayer on Ag (111) and Au (111) surfaces. *Physical Review B*, *69*(16), 165417.
[91] Trant, A. G., Jones, T. E., Gustafson, J., Noakes, T. C. Q., Bailey, P., & Baddeley, C. J. (2009). Alloy formation in the Au {1 1 1}/Ni system–An investigation with scanning tunnelling

microscopy and medium energy ion scattering. *Surface scien*ce, *603*(3), 571-579.
[92] Nielsen, L. P., Besenbacher, F., Stensgaard, I., Laegsgaard, E., Engdahl, C., Stoltze, P., ... & Nørskov, J. K. (1993). Initial growth of Au on Ni (110): Surface alloying of immiscible metals. *Physical review letters*, *71*(5), 754.
[93] Jones, T. E., Noakes, T. C., Bailey, P., & Baddeley, C. J. (2004). Adsorbate-induced segregation in the Ni {111}/Au/(R, R)-tartaric acid system. *The Journal of Physical Chemistry B, 108*(15), 4759-4766.
[94] Katona, G. L., Erdélyi, Z., Beke, D. L., Dietrich, C., Weigl, F., Boyen, H. G., ... & Ziemann, P. (2005). Experimental evidence for a nonparabolic nanoscale interface shift during the dissolution of Ni into bulk Au (111). *Physical Review B*, *71*(11), 115432.
[95] Wollschläger, J., & Amer, N. M. (1992). Heterogeneous nucleation and epitaxial growth of Au on the Co decorated Au (111) surface investigated by scanning tunneling microscopy. *Surface science, 277*(1-2), 1-7.
[96] To, C., Zeppenfeld, P., Krzyzowski, M. A., David, R., & Comsa, G. (1997). Growth and stability of cobalt nanostructures on gold (111). *Surface science, 394*(1-3), 170-184.
[97] Cotton, F. A. (1991). *Chemical applications of group theory*. John Wiley & Sons.
[98] Bodner, M., Patera, J., & Szajewska, M. (2014). Breaking of icosahedral symmetry: C 60 to C 70. *PloS one, 9(*3), e84079.
[99] Lu, F., Neal, E. A., & Nakanishi, T. (2019). Self-assembled and nonassembled alkylated-fullerene materials. *Accounts of chemical research, 52*(7), 1834-1843.
[100] Gimzewski, J. K., Modesti, S., & Schlittler, R. R. (1994). Cooperative self-assembly of Au atoms and C 60 on Au (110) surfaces. *Physical review letters, 72*(7), 1036.
[101] D'Souza, F., Deviprasad, G. R., Rahman, M. S., & Choi, J. P. (1999). Self-Assembled Porphyrin− C_{60} and Porphycene− C_{60} Complexes via Metal Axial Coordination. *Inorganic chemistry, 38*(9), 2157-2160.
[102] Dresselhaus, M. S., Dresselhaus, G., & Eklund, P. C. (1996). *Science of fullerenes and carbon nanotubes: their properties and applications.* Elsevier.
[103] Yannoni, C. S., Johnson, R. D., Meijer, G., Bethune, D. S., & Salem, J. R. (1991). Carbon-13 NMR study of the C_{60} cluster in the solid state: molecular motion and carbon chemical shift anisotropy. *The Journal of Physical Chemistry, 95*(1), 9-10.
[104] Curl, R. F., & Smalley, R. E. (1991). Fullerenes: the third form of pure carbon. S*ci. Am*, 265, 54.
[105] Altmann, S. L., & Herzig, P. (1994). Point-group theory tables. Oxford University Press.
[106] Rossel, F., Pivetta, M., Patthey, F., Ćavar, E., Seitsonen, A. P., & Schneider, W. D. (2011). Growth and characterization of fullerene nanocrystals on NaCl/Au (111). *Physical Review B, 84*(7), 075426.
[107] Schiller, F., Ruiz-Osés, M., Ortega, J. E., Segovia, P., Martínez-Blanco, J., Doyle, B. P., ... & Kröger, J. (2006). Electronic structure of C 60 on Au (887). *The Journal of chemical physics*, *125*(14), 144719.
[108] Kroto, H. (1988). Space, stars, C60, and soot. *Science*, *242*(4882), 1139-1145.
[109] Ren, S. L., & Wang, Y. Rao, a. *E. M ae. JM Holden, T. Hager, K. A. Wag, W. T. Lee*.
[110] Weaver, J. H., Martins, J. L., Komeda, T., Chen, Y., Ohno, T. R., Kroll, G. H., ... & Smalley, R. E. (1991). Electronic structure of solid C 60: Experiment and theory. *Physical review letters*, *66*(13), 1741.

[111] Hansen, P. L., Fallon, P. J., & Krätschmer, W. (1991). An EELS study of fullerite—C60/C70. *Chemical physics letters*, *181*(4), 367-372.
[112] Modesti, S., Cerasari, S., & Rudolf, P. (1993). Determination of charge states of C 60 adsorbed on metal surfaces. *Physical review letters, 71*(15), 2469.
[113] Hedberg, K., Hedberg, L., Bethune, D. S., Brown, C. A., Dorn, H. C., Johnson, R. D., & De Vries, M. (1991). Bond lengths in free molecules of buckminsterfullerene, C_{60}, from gas-phase electron diffraction. *Science, 254*(5030), 410-412.
[114] Prassides, K., Kroto, H. W., Taylor, R., Walton, D. R. M., David, W. I. F., Tomkinson, J., ... & Murphy, D. W. (1992). Fullerenes and fullerides in the solid state: Neutron scattering studies. *Carbon*, 30(8), 1277-1286.
[115] Hamada, I., & Tsukada, M. (2011). Adsorption of C 60 on Au (111) revisited: A van der Waals density functional study. *Physical Review B*, *83*(24), 245437.
[116] Altman, E. I., & Colton, R. J. (1993). Determination of the orientation of C 60 adsorbed on Au (111) and Ag (111). *Physical Review B*, *48*(24), 18244.
[117] Villagomez, C. J., Garzon, I. L., & Paz-Borbón, L. O. (2020). A first-principles dft dispersion-corrected c60/au (111) raman study. *Computational Materials Science*, *171*, 109208.
[118] Tzeng, C. T., Lo, W. S., Yuh, J. Y., Chu, R. Y., & Tsuei, K. D. (2000). Photoemission, near-edge x-ray-absorption spectroscopy, and low-energy electron-diffraction study of C 60 on Au (111) surfaces. *Physical Review B*, *61*(3), 2263.
[119] Murray, P. W., Pedersen, M. Ø., Lægsgaard, E., Stensgaard, I., & Besenbacher, F. (1997). Growth of C 60 on Cu (110) and Ni (110) surfaces: C 60-induced interfacial roughening. *Physical Review B*, *55*(15), 9360.
[120] Xie, Y. (2014). *An STM study of C_{60} molecule on Au (111): close-packed single layer and magic number clusters* (Doctoral dissertation, University of Birmingham).
[121] McKenzie, D. R., Davis, C. A., Cockayne, D. J. H., Muller, D. A., & Vassallo, A. M. (1992). The structure of the C_{70} molecule. *Nature, 355*(6361), 622-624.
[122] Schull, G., & Berndt, R. (2007). Orientationally ordered (7× 7) superstructure of C 60 on Au (111). *Physical review letters*, *99*(22), 226105.
[123] Altman, E. I., & Colton, R. J. (1992). Nucleation, growth, and structure of fullerene films on Au (111). *Surface science, 279*(1-2), 49-67.
[124] Fujita, D., Yakabe, T., Nejoh, H., Sato, T., & Iwatsuki, M. (1996). Scanning tunneling microscopy study on the initial adsorption behavior of C_{60} molecules on a reconstructed Au (111)-(23×$\sqrt{3}$) surface at various temperatures. *Surface science, 366*(1), 93-98.
[125] Zhang, X., Tang, L., & Guo, Q. (2010). Low-temperature growth of C_{60} monolayers on Au (111): island orientation control with site-selective nucleation. *The Journal of Physical Chemistry C, 114*(14), 6433-6439.
[126] Zhang, X., Yin, F., Palmer, R. E., & Guo, Q. (2008). The C_{60}/Au (1 1 1) interface at room temperature: A scanning tunnelling microscopy study. *Surface science, 602*(4), 885-892.
[127] Guo, S., Fogarty, D. P., Nagel, P. M., & Kandel, S. A. (2004). Thermal diffusion of C_{60} molecules and clusters on Au (111). *The Journal of Physical Chemistry B, 108*(37), 14074-14081.
[128] Saito, S., & Oshiyama, A. (1991). Cohesive mechanism and energy bands of solid C 60. *Physical Review Letters, 66*(20), 2637.
[129] Girifalco, L. A. (1991). Interaction potential for carbon (C_{60}) molecules. *The Journal of Physical Chemistry, 95*(14), 5370-5371.

[130] Wales, D. J. (1994). Clusters of C 60 molecules. Journal of the Chemical Society, *Faraday Transactions, 90*(8), 1061-1063.
[131] Hasegawa, M., Nishidate, K., Katayama, M., & Inaoka, T. (2003). Intermolecular potential and the equation of state of solid C 60. *The Journal of chemical physics, 119*(3), 1386-1396.
[132] Girifalco, L. A., Hodak, M., & Lee, R. S. (2000). Carbon nanotubes, buckyballs, ropes, and a universal graphitic potential. *Physical Review B, 62*(19), 13104.
[133] Kaya, D., Gao, J., Fard, M. R., Palmer, R. E., & Guo, Q. (2018). Controlled Manipulation of Magic Number Gold–Fullerene Clusters Using Scanning Tunneling *Microscopy. Langmuir, 34*(28), 8388-8392.
[134] Xie, Y. C., Tang, L., & Guo, Q. (2013). Cooperative assembly of magic number C 60-Au complexes. *Physical Review Letters, 111*(18), 186101.
[135] Kollamana, J., Wei, Z., Laux, M., Stöckl, J., Stadtmüller, B., Cinchetti, M., & Aeschlimann, M. (2016). Scanning tunneling microscopy study of ordered C_{60} submonolayer films on Co/Au (111). *The Journal of Physical Chemistry C, 120*(14), 7568-7574.
[136] Cummings, M., Gliga, S., Lukanov, B., Altman, E. I., Bode, M., & Barrera, E. V. (2011). Surface interactions of molecular C_{60} and impact on Ni (100) and Co (0001) film growth: A scanning tunneling microscopy study. *Surface science, 605*(1-2), 72-80.
[137] Sakai, S., Naramoto, H., Lavrentiev, V., Narumi, K., Maekawa, M., Kawasuso, A., ... & Baba, Y. (2005). Polymeric Co-C_{60} compound phase evolved in atomistically mixed thin films. *Materials transactions, 46*(4), 765-768.
[138] Kurikawa, T., Nagao, S., Miyajima, K., Nakajima, A., & Kaya, K. (1998). Formation of Cobalt− C_{60} Clusters: Tricapped Co $(C_{60})_3$ Unit. *The Journal of Physical Chemistry A, 102*(10), 1743-1747.
[139] Nagao, S., Kurikawa, T., Miyajima, K., Nakajima, A., & Kaya, K. (1998). Formation and Structures of Transition Metal− C_{60} Clusters. *The Journal of Physical Chemistry A, 102*(24), 4495-4500.
[140] Avramov, P., Naramoto, H., Sakai, S., Narumi, K., Lavrentiev, V., & Maeda, Y. (2007). Quantum Chemical Study of Atomic Structure Evolution of Co_x/C_{60} ($x \leq 2.8$) Composites. *The Journal of Physical Chemistry A, 111*(12), 2299-2306.
[141] Lavrentiev, V., Naramoto, H., Abe, H., Yamamoto, S., Narumi, K., & Sakai, S. (2005). Chemically driven microstructure evolution in cobalt–fullerene mixed system. *Fullerenes, Nanotubes and Carbon Nanostructures, 12*(1-2), 519-528.
[142] Torrelles, X., Pedio, M., Cepek, C., & Felici, R. (2012). $(2\sqrt{3} \times 2\sqrt{3})$ R 30° induced self-assembly ordering by C 60 on a Au (111) surface: X-ray diffraction structure analysis. *Physical Review B, 86*(7), 075461.
[143] Chakrabarty, R., Mukherjee, P. S., & Stang, P. J. (2011). Supramolecular coordination: self-assembly of finite two-and three-dimensional ensembles. *Chemical reviews*, *111*(11), 6810-6918.
[144] Chai, Y., Guo, T., Jin, C., Haufler, R. E., Chibante, L. F., Fure, J., ... & Smalley, R. E. (1991). Fullerenes with metals inside. *The Journal of Physical Chemistry, 95*(20), 7564-7568.
[145] Caldwell, K. A., Giblin, D. E., Hsu, C. S., Cox, D., & Gross, M. L. (1991). Endohedral complexes of fullerene radical cations. *Journal of the American Chemical Society, 113*(22), 8519-8521.
[146] McElvany, S. W. (1992). Production of endohedral yttrium-fullerene cations by direct laser

vaporization. *The Journal of Physical Chemistry, 96*(12), 4935-4937.
[147] Goldberg, N., & Hoffmann, R. (1996). Hypothetical C_{60} Metal-Cluster Fullerides and General Aspects of Tetrahedral Cluster Bonding. *Inorganic chemistry, 35*(15), 4369-4377.
[148] Winter, J., Burger, B., Hulman, M., Kuzmany, H., & Soldatov, A. (1997). Experimental access to doped fullerene polymers. *Applied Physics A, 64*(3), 257-262.
[149] Chen, Z. Y., Zhao, J. P., Yano, T., & Sakakibara, J. (2000). Growth mechanism of diamond by laser ablation of graphite in oxygen atmosphere. *Physical Review B, 62*(11), 7581.
[150] Ager III, J. W., & Drory, M. D. (1993). Quantitative measurement of residual biaxial stress by Raman spectroscopy in diamond grown on a Ti alloy by chemical vapor deposition. *Physical Review B, 48*(4), 2601.
[151] Wang, H., He, Y., Li, Y., & Su, H. (2012). Photophysical and electronic properties of five PCBM-like C60 derivatives: spectral and quantum chemical view. *The Journal of Physical Chemistry A*, *116*(1), 255-262.

Chapter 3. Experimental Equipment and Techniques

3.1 Variable Temperature Scanning Tunneling Microscopy

3.1.1 The STM System

The most significant equipment used in this experiment is the VT-STM system in the NPRL laboratory of the University of Birmingham produced by Omicron. Fig. 3.1 (a) shows the main schematic diagram of this equipment. It consists of a main chamber that can maintain an internal ultra-high vacuum (UHV) of 10^{-10} mbar and a secondary chamber known as the Fast Entry Lock (FEL). Through the FEL chamber, the sample and probe can be transferred from the atmosphere into the vacuum chamber with keeping the ultra-high vacuum of the main chamber. In order to achieve this, the FEL can be rapidly pumped from atmosphere to a vacuum of 10^{-9} mbar, and vent from high vacuum to atmospheric pressure without any destructive effects by inflating liquid nitrogen [1].

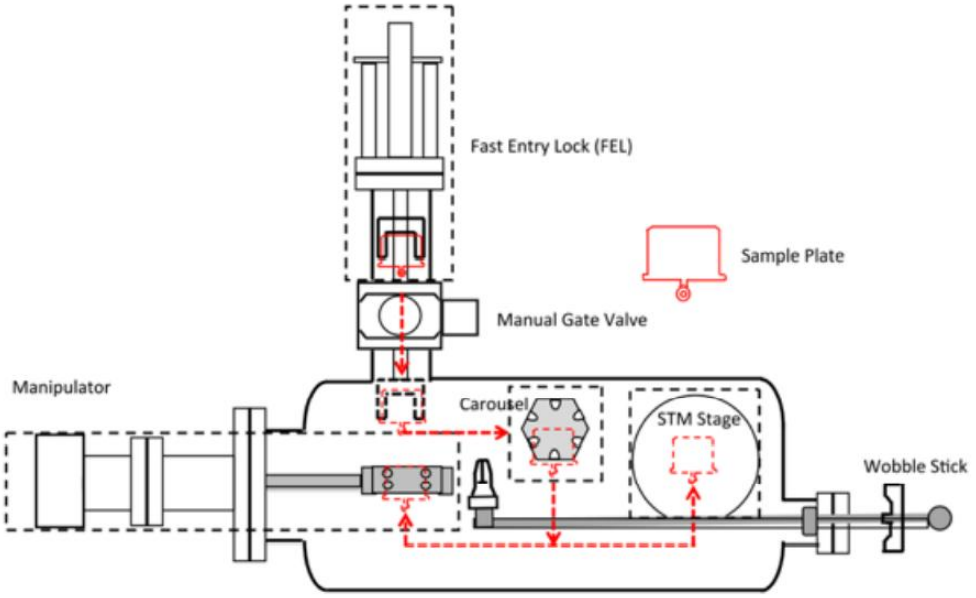

Fig. 3.1 Diagram of the VT-STM produced by Omicron. The manipulator is in the main chamber, which links the Fast Entry Lock. A carousel stage is put between STM and the manipulator, used for storing the samples and the tips. STM stage is mounted on the right side of the main chamber. [1]

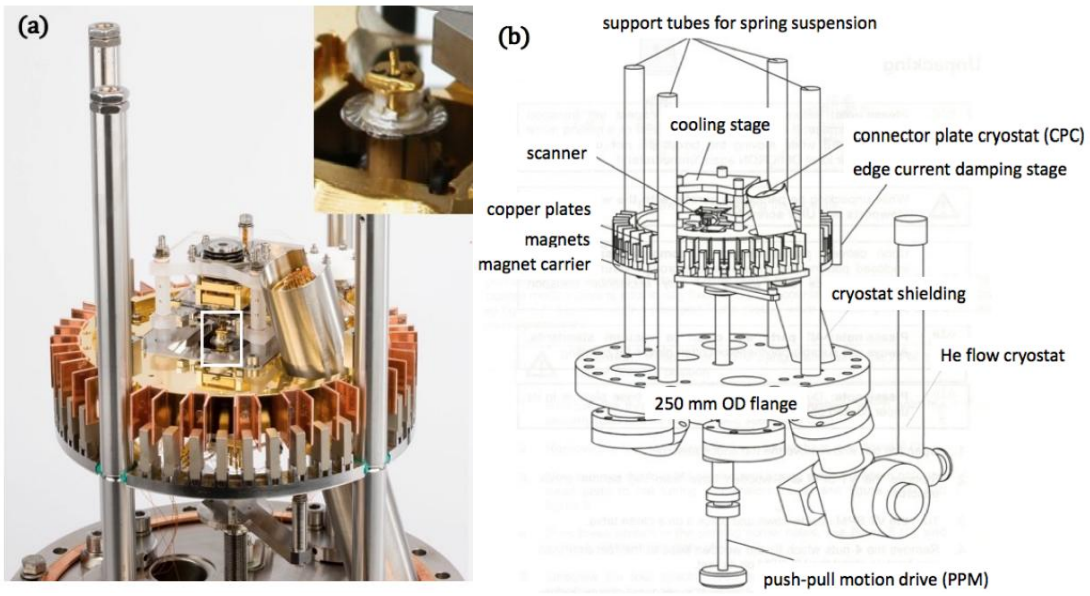

Fig. 3.2 (a) Product image of a variable temperature scanning tunneling microscope (VT-STM) with an eddy current vibration isolation system. The probe area is enlarged and shown in the inset. (b) Schematic diagram of the eddy current vibration isolation system. The whole STM stage is mounted on the main chamber with a 250 mm OD flange. Under the STM stage, there is a push-pull driver used to move the STM up and down. A helium flow cryostat is attached to a heat transfer that passes through the flange as well as the base stage. The cooling stage is set directly above the sample stage and is supported by three ceramic rods with a rectangular copper bar, called the cooling block. A connecting plate cryostat (CPC) is connected to the cooling block by a bundle of highly flexible copper braids. Liquid helium or liquid nitrogen can reach the cooling block via the cryostat. When the cooling block covers the sample, both the cooling block and the sample can be cooling down to low temperature. [1]

In addition to the STM stage, which is responsible for the tunneling function, the main chamber also contains a manipulator, a carousel for sample and probe storage, a wobble stick for sample transition, an argon ion sputtering system for cleaning the sample surface and two deposition sources, which are not shown in Fig. 3.1. On the manipulator, the sample can be heated by resistive heating to 750 K and by direct heating to 1500 K. It can also be used with argon ion gun sputtering to clean the

surface of precious metals such as gold and platinum, or to create atomic scale defects on the surface of samples such as HOPG. The rotatable hexagonal carousel with 12 slots at the top and bottom allows the sample and probe to be stored in ultra-high vacuum. Wobble stick is semi-inserted into the chamber and can rotate an angle while moving vertically in the normal direction. Together with the clamp on the top perpendicular to the rod, the wobble stick enables the transfer of samples or probes between the manipulator, the carousel and the STM stage.

The structure of the STM-stage is shown in Fig. 3.2. It consists of the sample stage with the accompanying variable temperature system, the scanning probe below the sample, and the vibration damping system. The cooling table is set above the sample table and is supported by three ceramic rods, one of which is a rectangular copper rod called the cooling block. The connecting plate cryostat (CPC) is connected to the cooling block by a bundle of highly flexible copper braid. Liquid helium and liquid nitrogen can reach the cooling block through the cryostat. When the cooling block covers the sample, both the cooling block and the sample can be cooled to low temperature. The scanning probe is placed on a piezoelectric ceramic tube, which can shift in the XYZ directions individually by voltages applied in corresponding directions to complete the nano-scale scanning. The whole tube is connected to a push-pull driver with three levels of slides which are independent of others in XYZ directions to ensure the independent movement of the probe relative to the whole stage.

The STM scan is very sensitive to noise. Therefore, it is equipped with its own damping and vibration isolation system. The STM scanner is fixed on an eddy current damping stage, which is surrounded by a series of copper plates and suspended by four springs. These copper plates are interval inserted into a series of magnets fixed to the cavity. The magnets reduce the movement of the plates according to the damping principle and increase the stability of the working system. The spring combined with

the eddy current damping stage significantly prevents external vibrations from the STM platform.

3.1.2 Heating and Cooling Systems

The main difference between a variable temperature STM and a room temperature or low temperature STM is that it allows for scanning over a very wide temperature range. The theoretical scanning temperature range of our VT-STM is 25 K to 1500 K[1]. To achieve the temperature variation of the sample, the STM is equipped with both heating and cooling systems. So, the VT-STM uses a special sample holder.

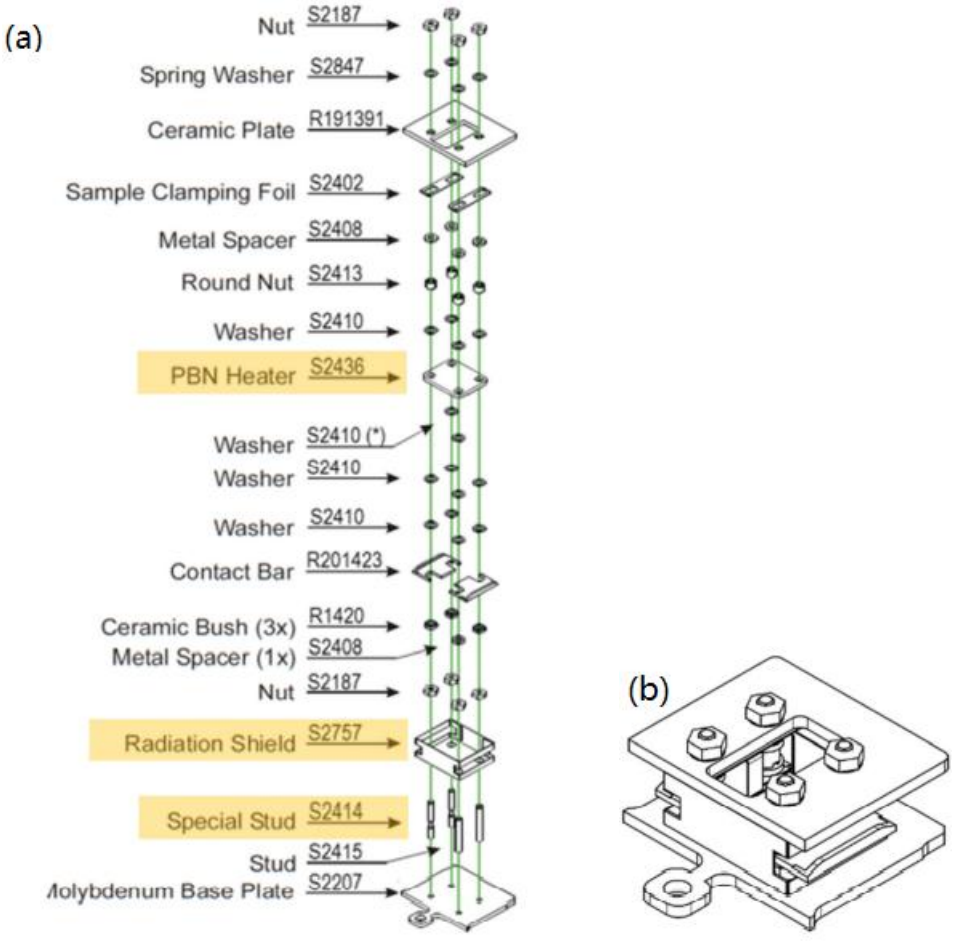

Fig. 3.3 (a) A disassembled structure diagram of the VT-STM sample holder. The position of the PBN heater and contact bar in relation to the radiation shield is shown. The sample is placed between the sample clamping foil and the Ceramic plate. (b) Diagram showing the completed assembly of the sample holder. [2]

Fig. 3.3 shows the sample holder made for radiative heating to different temperatures. It has two contact bars made of molybdenum on either side which make contact with the contact brushes on the STM stage and allow current to pass through the sample. It includes an additional ceramic plate which acts primarily as a fixation device for the test sample during the scanning process. Only one side of the ceramic plate is coated with metal to prevent it from being charged itself. Inside the metal slotted radiation shield there is a small PBN plate which is set just below the sample.

The Omicron VT-STM is available with two different types of heating system. One is radiant heating and the other is DC heating. Radiant heating is achieved by the PBN plate. When the sample is placed on the sample table, the sample holder is in close contact with the contact brushes on the sample table and this creates a closed loop circuit between the sample and the heater. The PBN is heated by the thermal effect of current and the sample above it is heated by thermal radiation. In this mode the upper temperature limit for the sample is 750 K. The direct current heating mode is suitable for samples with high electrical conductivity. In this mode, the PBN plate is removed and the current is passed directly through the conductive sample, in which case the sample can be heated to 1500 K.

There are many benefits to scanning samples at low temperatures. The low temperature inhibits thermal motion to ensure clearer and more stable images, while the low desorption temperatures of certain molecules dictate that they are only likely to be stable at low temperatures [1]. The sample cooling system works based on a clamping mechanism. The base plate of the sample holder is in contact with the sample through four spacers, while a cooling block is held on top of the base plate. The cooling block is connected to the cryostat (CPC) by a series of copper braids. When the cooling system is in operation, the block is pushed down to make tight contact with the sample. Heat transfers from the sample to the cooling block and out

through contact heat transfer. Liquid nitrogen or helium is usually chosen as the coolant, which flows through the cryostat tube, the CPC and finally the cooling block. By using liquid nitrogen, the sample can be cooling down to as low as 110 K. At the same time, the CPC can be adjusted to control the flow of liquid nitrogen to a temperature somewhere between the minimum temperature and room temperature. If liquid helium is used, 25 K can be achieved.

3.2 The Ultra-High Vacuum System

3.2.1 The Definition of Ultra-High Vacuum

The STM system has extremely high requirements for the vacuum of the work. That is because that the gas particle's free path in the chamber will increase and the sample surface will be polluted under high pressure. The particle flux falling on the unit monolayer surface in unit time can be calculated by the Hertz Knudsen equation [3].

$$Z_W = \frac{p}{\sqrt{2\pi m k_B T}} \tag{3.1}$$

Where m is the particle's mass, the chamber pressure is p and the temperature is T.

Approximately, a vacuum of 1×10^{-6} mbar at room temperature of 300 K can be considered as a complete molecular impact on the sample surface within one second [3]. At 1×10^{-10} mbar, this process is extended to more than one hour. Ultra-high vacuum is defined by pressures lower than 10^{-9} mbar (10^{-7} pascal or 10^{-9} torr).

3.2.2 Vacuum Measurement

In order to measure the true pressure inside an ultra-high vacuum chamber, we use a hot-filament ionization gauge. Fig. 3.4 is an image of the ionization gauge. It is a triode, with the filament being the cathode. A current (usually 10mA) is emitted from the heated filament onto the spiral grid. The gas molecules in between will be ionized. When the ionized gas is captured by a negative potential, the current is detected.

The number of these ions is proportional to the density of the gas molecules and the electron current from the filament. So that by measuring the strength of the collected ion current, the density of the gas molecules in the chamber can be calculated and thus the pressure can be given.

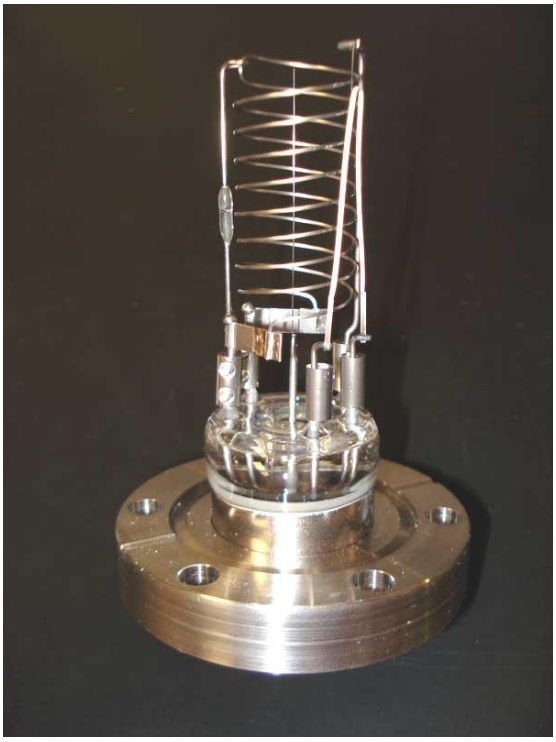

Fig. 3.4 Bayard-Alpert hot thoriated iridium filament ionization gauge on 2.75 in CF flange. [4]

3.2.3 Vacuum Attaining and Various Pump

For different vacuum pump, they have different working pressure range. It means that pumping a system from atmosphere to UHV needs a combination of kinds of pumps. The main pump of the system to pump it from atmosphere to high vacuum is a turbo pump which is pre-pumped by the rotary pump. The working vacuum of turbo pump is under 10^{-2} mbar and it can pump the system to 10^{-9} mbar, so it needs rotary pump to pre-pump the system first. The rotary pump has a circular rotor rotating inside a larger circular cavity with vanes on the rotor which can slide into or out of the rotor. The rotor and cavity are offset and tangency. The atmospheric pressure is provided by the

vanes to push the gas out. The turbo molecular pump consists of multiple stages of high-speed rotating blades to hit the molecular and transfer the energy to it. The gas molecules with high speed will be leaded to next stage through the transfer gas and finally outwards through the exhaust. The turbo pump will produce a lot of heat so it must always work under water cooling.

The ion pump and the titanium sublimation pump (TSP) work better at pressures below 10^{-7} mbar, so they need to be combined with rotary and turbo pumps to pump the chamber from high vacuum to ultra-high vacuum. Ion pump is basic on a penning trap. The anode and cathode produce an electromagnetic field and ionize the gas particles. Under the electromagnetic field, the gas ions will be attracted to the cathode and anode and adsorbed in cathode and anode. TSP is mainly used to pump the hydrogen atoms out which is difficult to be removed by other pumps. It consists of a titanium filament which can be sublimated by high current. During working, the Ti gas will be sublimated into the chamber and cooling down to form a Ti film on the inner wall of the chamber. Because clean Ti is reactive, the gas in chamber, especially hydrogen, will react with it and form a solid, stable product. The TSP can’t work long hours and must have a time interval between each work.

What’s more, the gas adsorbed on the wall especially the water molecule is also a problem. Under low pressure, the gas molecules adsorbed on the wall will be much more than those floating in the chamber. Water is the representative of them. Under room temperature, water evaporates slowly, so it’s necessary to heat the system to a high temperature to desorb these molecules. Because of that, before pumping the system from atmosphere to the UHV, we need to heat the system above 100 °C for 2 days to remove water and other molecules adsorbed on the wall of the chamber, which is called bake-out.

3.2.4 Pumping, Venting and Baking

As mentioned above, the multiple pumps of the STM ultra-high vacuum system have different conditions of use and therefore the sequence of start-up of the individual pumps will be important in pumping the chamber to ultra-high vacuum. For the four pumps mentioned above, the turbo pump, the ion pump and the TSP are all primary vacuum pumps, directly connected to the STM chamber, while the rotary pump is a secondary pump, connected to the turbo pump. Of the three primary pumps, TSP and the ion pump do not need to be connected to the outside and therefore do not leak even if they are closed, whereas the turbo pump will definitely leak if it is closed. So, there is a valve between the turbo pump and the chamber. If the pump system is to be used, the rotary pump must first be activated to pump the entire chamber to a pressure below 10^{-2} mbar. In this pressure range, the ion gauge does not work, so the vacuum in the chamber cannot be measured directly and can only be judged by the controller light of the turbo pump. After approximately 15 minutes of rotary pump operation, the chamber pressure will reach the operating range of the turbo pump and the turbo pump can then be switched on. After the turbo pump has been switched on, it will still take some time until the pressure drops to the point where the ion gauge could work. After approximately 2 hours, the vacuum in the chamber reaches below 10^{-5} mbar, at which point the ion gauge is switched on. When the pressure drops below 10^{-6} mbar, it is necessary to start baking to pump out the huge amount of water molecules that have been adsorbed by the chamber.

During the baking process the STM system is completely covered by a heat shield and all glass windows and ceramic parts need to be protected by a foil wrap to avoid uneven heating and breakage. All parts that cannot withstand high temperatures, such as plastic, rubber or magnetic parts, need to be removed. In addition, open electronic interfaces need to be protected with metal plugs in order to avoid harmful discharges. Baking is carried out by oven heating. The final baking temperature is 140-150°C. The whole heating process lasts 24-60 hours until all gases and moisture are desorbed

from the chamber and pumped out by the turbo pump. When the baking is complete, the pressure of the system drops to 10^{-7} mbar at 150°C. The ion pump and TSP has powerful adsorption so it need to be switched on for degassing before the chamber has completely cooled down. The initial degassing will cause a rapid increase of pressure in the chamber. Repeat degassing until the ion pump or TSP operates does not cause a radical change in pressure. Finally when the temperature drops back to room temperature, the vacuum will reach an UHV level of 2×10^{-9} mbar. With the turbo-pump valve closed, the pressure will eventually reach 10^{-10} mbar or even 10^{-11} mbar after approximately one night of pumping. By this process, the STM chamber is pumped from atmospheric pressure to the ultra-high vacuum level required for the experiment.

Similar to pumping, venting the whole system is also in order. As the pressure inside the chamber is much lower than the atmospheric pressure, opening the valve directly will cause physical damage to the instrument due to the strong airflow, while the high levels of oxygen and water in the air will also have a negative impact on the equipment. Therefor the entire chamber needs to be protected by nitrogen in the venting. In the experiments, the vent valves are connected directly to the liquid nitrogen via a tube. After all pumps have been switched off, the nitrogen is slowly and steadily pumped into the chamber by slowly opening the valve, thereby protecting the equipment from air contamination.

3.2.5 Leakage Detection

STM ultra-high vacuum systems are very sensitive to leaks and any slight leak can cause a pressure change of two orders of magnitude. At the same time, the complexity of the ultra-high vacuum system results in an extremely large number of possible leak locations. Therefore, STM equipment requires a systematic approach for leak detection. In our experiments, a mass spectrometer and the test helium gas are used for leakage detection. The mass spectrometer in use is connected to the vent valve of

the turbo pump and pumps the entire system via the built-in mechanical pump. It has an audible indicator which alerts when the helium concentration rises and the leak can also be observed from the mass spectrum of the helium. Helium is used because it is inert, harmless to humans and is rare in the air, making it a safe and clear marker of leaking. If helium is pumped through the leaking part, it is pumped into the chamber and detected by the mass spectrometer. The leaking is identified. During the leak detection process, the room will inevitably fill with helium, and as helium is less dense than air, it will gradually occupy the upper part of the room, so leak detection should be carried out in a top-to-bottom sequence. In order to avoid interference between adjacent interfaces, all other possible leak locations should be wrapped in aluminum foil when testing one location. Furthermore, as it takes time for the helium to be pumped from the leak into the mass spectrometer, it is important to wait enough time between each leak detection at two different locations to avoid interferences.

3.3 STM Tip Preparation

The resolution of the STM image is directly linked to the quality of the probe. Ideally, people would like the probe to be perfectly sharp, with only one atom present at the tip. However, this is difficult to achieve in practice, not only to ensure that the tip is absolutely sharp, but also to make visual observations of the sharpness of the tip. In experiments, STM probes are prepared mainly by mechanical cutting and electrochemical etching. The finished tip needs to be adjusted by subsequent treatment in order to achieve the best possible condition.

3.3.1 Electrochemical Etching of Tip

The mechanical cutting method uses an Ir/Pt alloy where the tip of the probe is mechanically cut with shears. The sharpness of the tip is directly relied on the angle of the shear. The properties of the tips prepared by this method are generally better than those of electrochemically etched tips. Electrochemistry, however, is a simpler and easier manipulated method of preparation. So, in this experiment, the STM probes

were all tungsten probes prepared by electrochemical etching.

The STM tips used are made from 0.38 nm thick tungsten wires etched in a 2M NaOH solution. As shown in Fig. 3.5, the tungsten wire is cut into 2-4 cm length to act as the anode, and there is another piece of tungsten wire that acts as the cathode. There is a voltage of 10 V between the anode and cathode. In order to control the tip length, the tungsten wire should only remain about 2 mm long at the top end of the solution page.

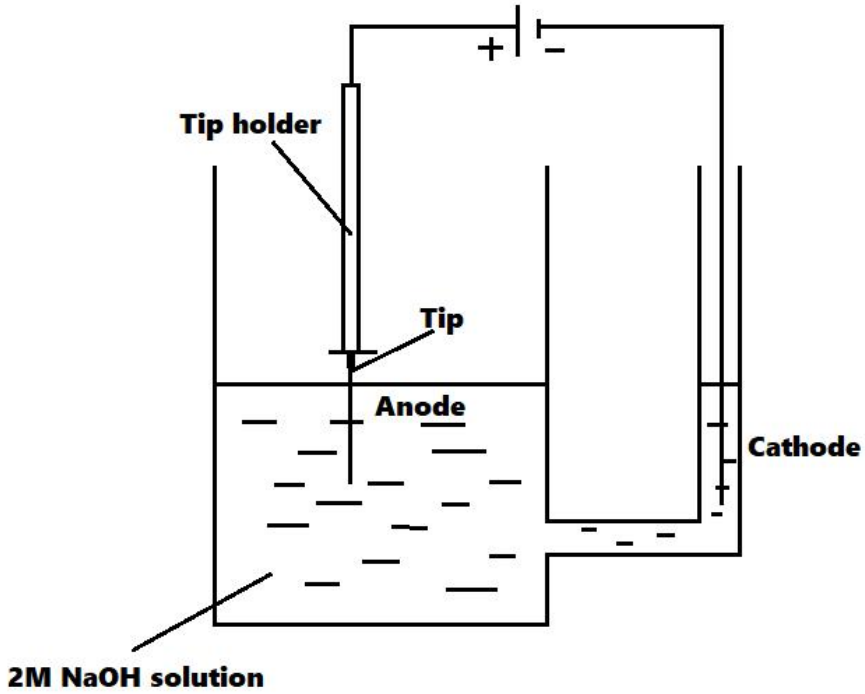

Fig. 3.5 Schematic diagram of electrochemistry etching. The W wire is located on the tip holder extended into the NaOH solution as the anode. There is another W wire extended into solution as the cathode. During etching, the hydrogen will emerge from the cathode.

The chemical reactions taken place on the cathode and anode is as following:

$$Cathode: \quad 6H_2O + 6e^- \rightarrow 3H_2 + 6OH^-$$

$$Anode: \quad W + 8OH^- \rightarrow WO_4{}^{2-} + 4H_2O + 6e^-$$

During the etching process, a current of approximately 1.0 A passes through the anode.

Hydrogen gas will be continuously emitted at the cathode. Because of the surface tension, the NaOH solution forms a small steep slope along the tungsten wire, so that the etching rate at the interface of the solution will be different for different heights of the tungsten wire. Eventually the tungsten filament at the interface will become thinner and thinner until it is completely disconnected from the lower half of the solution, at which point the tip is completed and the pathway is disconnected to stop etching. After etching, we will use an optical microscope to examine the general shape of the tip. A good tip is as sharp as possible. Its peak length should be twice as long as its width, and it should be consistent in all directions. If the tip is OK, it should be washed in distilled water in 3 beakers in turn, then dried by nitrogen and transferred into the UHV chamber.

3.3.2 Probe Treatment

Inside the ultra-high vacuum cavity, the probe is treated by annealing to obtain a better surface condition. This process can be divided into two main stages. At a temperature of 150°C, the gas and water molecules adsorbed in the probe are gradually desorbed. This is also the stage where the pressure in the ultra-high vacuum chamber changes most dramatically. If the probe has not been left in vacuum for a long time to slowly desorb, the pressure in the vacuum may instantly increase by 2-3 orders of magnitude. So, heating should be slow for probes newly placed in the UHV chamber. What's more, if the probe is heated above 1000°C, the tungsten oxide film on the surface of the probe can be removed. The melting point of tungsten is 3400°C while the tungsten oxide has a sublimation temperature of 800°C, so annealing in vacuum can be effective in removing the surface tungsten oxide[8]. These accessories can increase the resolution of the scan because they affect the stability of the tunneling current.

After annealing, the probe is mounted on top of the scanning tube and the final commissioning of the probe can be completed by scanning the sample. On the one

hand, gold surface reconstruction has been well studied and a comparison of the scanned images of the DLs on the gold surface gives a good insight into the working state of the probe. On the other hand, due to the softness of the Au surface compared to tungsten, the treatment of the probe can be carried out by inserting the probe shallowly into the gold surface[3]. On top of this, a sudden application of an electrical pulse of approximately twice with the scanning current to the tip during the scanning can slightly perturb the atoms on the tip. By this method the tip can be self-refined somewhat, thus obtaining a higher resolution.

3.4 Substrate Preparation and Cleaning

3.4.1 HOPG Substrate

In the experiments, it was necessary to prepare flat HOPG surface substrates, because the Au(111) substrates are grown on HOPG substrates based on the PVD method. Therefore, the most basic part of the experiment is to prepare flat HOPG substrates using the tape exfoliate method.

The highly oriented pyrolytic graphite (HOPG) is a synthetic graphite with high order. The HOPG is easily to spilt in vertical direction but has additional tensile stress in the basal-plane direction. It means that for the HOPG the adhesion of the top layer to its own bulk crystal is lower than the adhesion to the substrate, so mechanical exfoliation is possible. On experiment, I use adhesive tape to exfoliate the HOPG layer to get the atomic scale flat surface.

3.4.2 Evaporator System and Gold Deposition

The preparation of the gold substrates is carried out in an Edwards evaporator. The Edwards evaporator is a high vacuum system whose operating vacuum is about 10^{-7} mbar. What's more, the system uses 2 pumps and 2 gauges to approach this vacuum. The rotary pump provides an operating vacuum to the turbo pump which pumps the

chamber. Pirani gauge measures the operating vacuum of the turbo pump in the range of 10^{-4} mbar and above and the Penning gauge checks the vacuum of the chamber with an accuracy range of 10^{-7} mbar. The diagram of the vacuum system is shown in Fig. 3.6.

The HOPG substrate is placed in a copper holder with a thermocouple slot on one side for temperature detection and a holder sandwich with a tungsten wire held by a mica sheet to heat the substrate when the circuit is connected. The gold of the evaporation source, using 99.99% gold wire, is placed in a boat made of molybdenum, through which the current is heated directly. Inside the chamber, the boats are placed upwards, directly opposite the downward-facing substrate holders, which are approximately 7 cm apart. Between them, a rotating shutter is used to shield the substrate when required.

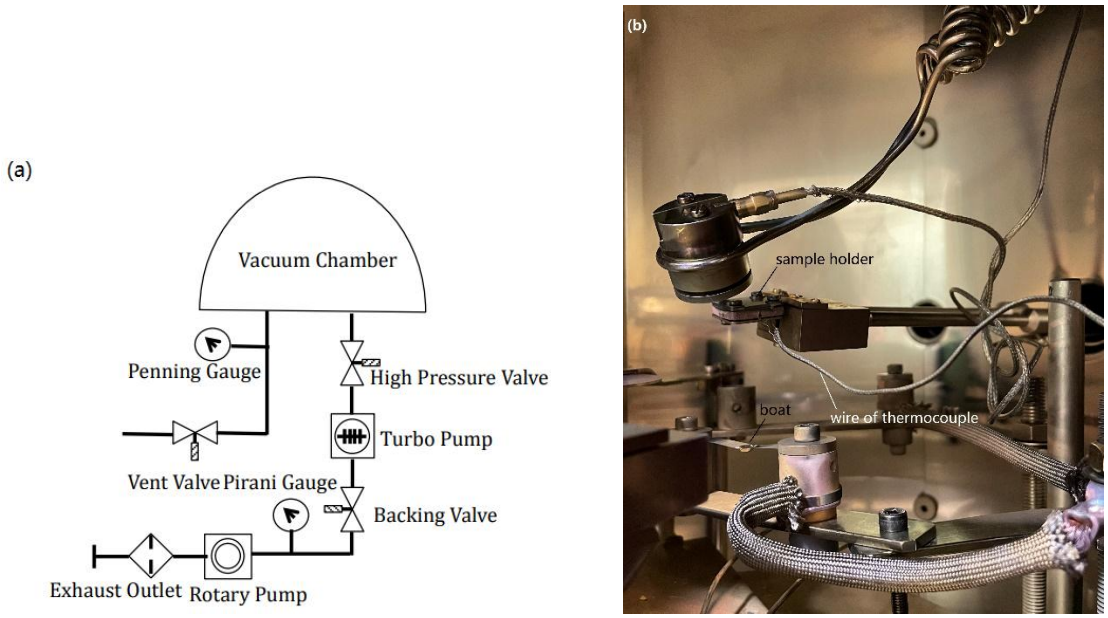

Fig. 3.6 (a) A diagram of the Edwards vacuum pumping system. The diagram shows the main valves, all stages of pumps and two vacuum gauges. [4] (b) A photograph of the inside of the evaporator with the sample holder facing the boat that holds the metal source. A thermocouple is attached to the sample to measure the temperature of the sample.

Before deposition begins, the HOPG substrate is degassed at 400 K and then heated

and kept at a temperature of 500 K. This is because the high substrate temperature enhances the diffusion rate of the gold atoms and facilitates the production of a flatter gold film. After the substrate has been heated, the shutter is switched off to shield the sample. The temperature is increased by applying a gradual increasing current with 5 A one time per 10 min from 10 A to 40 A. The thickness and the depositing rate of gold are measured using an inserted quartz crystal oscillator. After the deposition, the shutter will be switched off again and the heating of the substrate and boat will be stopped until the temperature cooling down to room temperature. For the experimentally prepared 200 nm thick gold film, the golden metallic luster can be observed by eyes, so visual observation can be the first step in checking the success of the sample.

3.4.3 Ion Gun Sputtering and Annealing

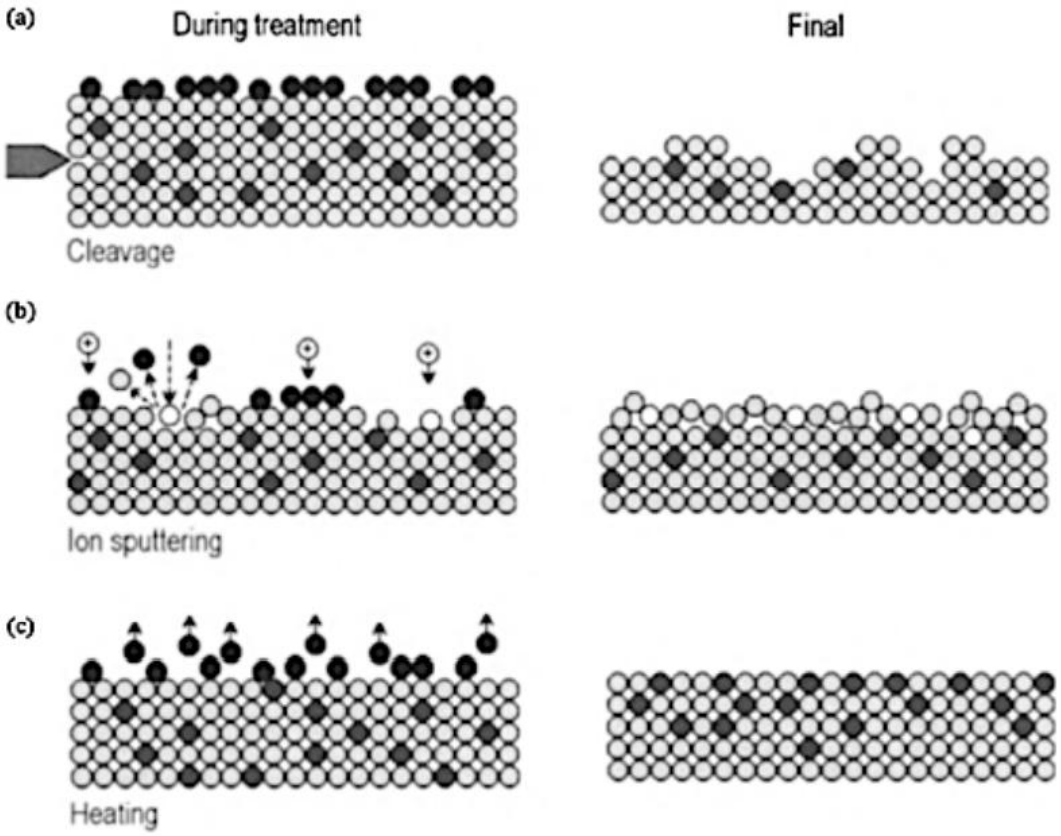

Fig. 3.7 Diagram of the process of cleaning gold surfaces using ion gun sputtering and annealing. Light color spheres are the gold atoms while the dark color spheres denote the impurity atoms

mixed in the bulk of sample or adsorbed onto the material surface. [5]

For gold films produced using PVD equipment, an ion gun sputtering and annealing process in the ultra-high vacuum chamber is required for a clean Au(111) substrate with atomic level flatness. Fig. 3.7 illustrates the process of cleaning the gold surface using ion gun sputtering and annealing. Argon gas is ionized by a magnetic field inside the ion gun with high energy and hits the Au (111) surface with high power. The ion beam current used in the experiments ranged is approximately 10-15 μA, while 15 μA was sufficient to completely strip a small area of gold from a 200 nm thick gold film within 5 minutes. The sample needs to be heated at 500°C to remove the remaining impurities from the surface. At the same time, the high temperature annealing accelerates the diffusion of atoms from the surface. This helps the sample surface to repair itself and smooth out.

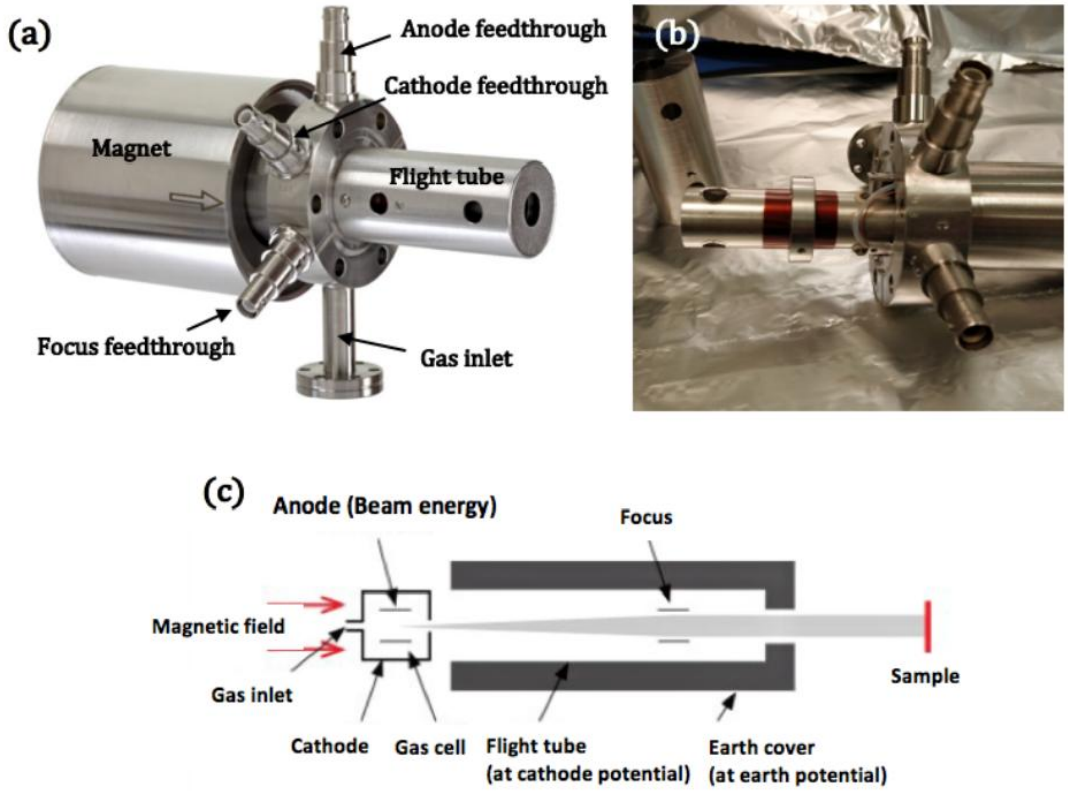

Fig. 3.8 (a) An external view of the ISE 5 cold cathode sputtering ion gun. It shows the main

components, including a permanent magnet covering the gas cell, the anode, cathode, beam focus and the gas inlet. (b) Internal structure of the ion gun. Argon gas flows through a white tube inside the hood and into the gas chamber. (c) Shows the principle of operation of the cold cathode source ion gun. The ion flight tube is at cathodic potential, while the outer ground hood is at ground potential [6].

Argon ion sputtering is achieved with the ISE 5 ion gun. An ISE 5 ion gun has an optimum working pressure between 5×10^{-6} mbar and 8×10^{-5} mbar. At this operating pressure it can deliver beam energies from 250 eV to 5 keV and a maximum current of 1 mA. Fig 3.8 (a)-(c) show the external view, the internal view and the operating principle of the ISE 5 ion gun respectively. The ion flight tube is at cathode potential, while the outside ground cover is at ground potential. Argon gas enters the ion gun through a leakage valve and is then ionized between the cathode and anode. Magnets cover the gas chamber for enhancing the ionization and a focusing plate is used to control the size of the ion beam [6].

3.5 Molecular Deposition System

3.5.1 C_{60} Deposition

In-suit deposition in the UHV-STM system is achieved by Knudsen cell (K cell). Knudsen cell is an effusion evaporator source for low particle pressure source in

crystal deposition. A typical Knudsen cell includes a crucible, heat shields, water cooling system, an orifice shutter and tantalum heating filaments. For C_{60} deposition, the C_{60} powder is stored in a pocket made by tantalum. As show in Fig. 3.9, the tantalum pocket is cut and welded from a piece of tantalum foil. The C_{60} deposition temperature is about 300 °C-400 °C and for this temperature an extra cooling water is unnecessary. In experiment there is a thermocouple thermometer to measure the heating temperature. At the first time putting the C_{60} source into the UHV, it needs a long time degas to remove the impurity. The metal pocket will be heating to 400°C for 5 minutes and at the beginning the pressure would increase to 1×10^{-7} mbar. After repeated degas, when the pressure of the chamber under 400 °C is lower than 5×10^{-8} mbar, it means that the C_{60} source is clean enough for deposition. Before every deposition, the C_{60} source is degassed under 400 °C for 10 minutes and then start deposit at a K cell temperature of 400 °C.

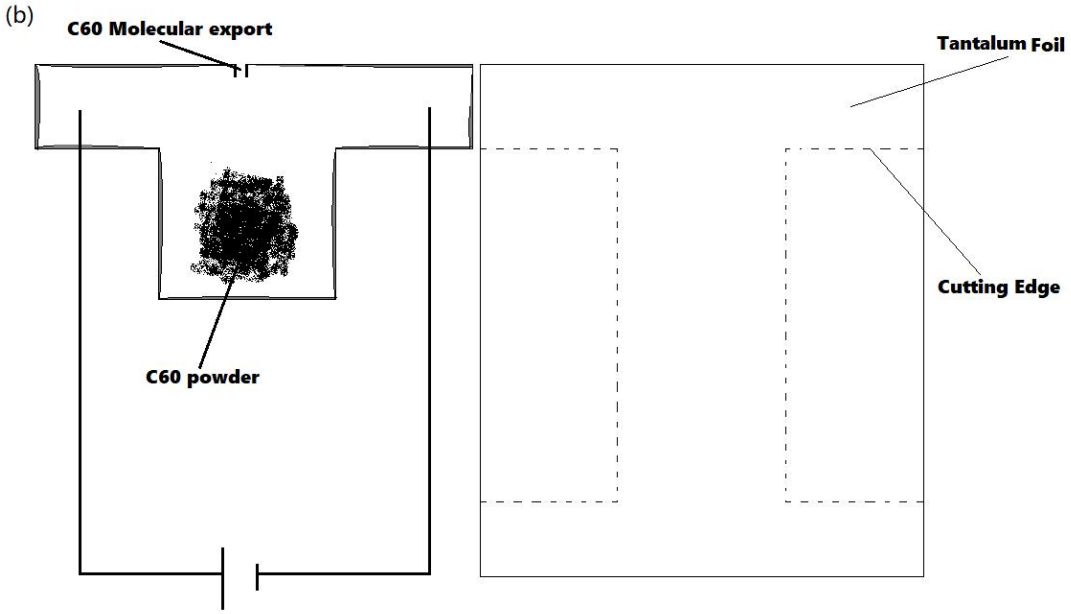

Fig. 3.9 (a) Picture of a homemade Knudsen cell. the C_{60} pack is connected to the copper column by a tungsten wire and tantalum foil contact with a thermocouple. (b)The schematic diagram of the T-type tantalum pocket which is cut from a tantalum rectangle foil. The foil is cut through the dotted line and folded into T-type. The circumference of the pocket is spot welded and left an export for C_{60} molecules.

3.5.2 Cobalt Deposition

The Knudsen cell of metal atom deposition was made by CreaTech as shown in Fig. 3.10. The Cobalt source is 99.99% purity Cobalt bar put in Al_2O_3 ceramic enamel. Any contact with other metal will pollute the Cobalt wire so metal pocket is unused. There is a controlled shutter in front of the cell which can stop impurities of Cobalt source to deposit on sample during degas [7]. K cell has a matching temperature control unit to accurately control the heating temperature. The Cobalt deposition temperature is over 1300°C so the cooling water is necessary. The Cobalt source needs a long time degas to remove the impurity at the first time.

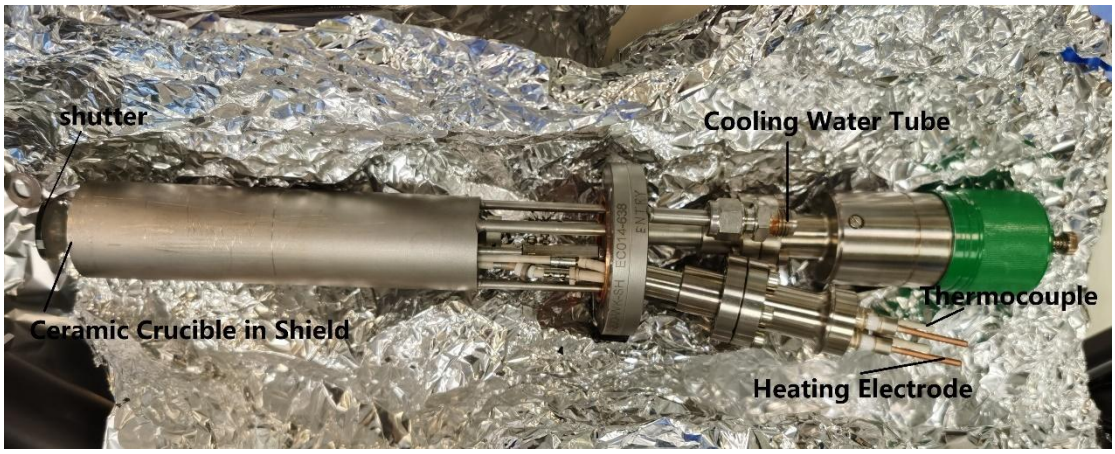

Fig. 3.10 Picture of a Knudsen cell made by CreaTech. The Al_2O_3 ceramic crucible with the cobalt source is inside the metal shield on top. Thermocouples and heating electrodes are connected to the controller to control the deposition of cobalt.

3.5.3 Coverage

The coverage of particles is measured with the help of STM and image processing software “Fiji”. Firstly, the coverage measurement is based on the premise that the number of particles evaporated per unit time from the same source at the same temperature without additional manipulation is approximately constant. For samples, this means the same coverage per unit evaporation time. After the STM has been

commissioned into operation, each evaporation source is subjected to a pre-evaporation on a gold substrate. This experiment is used to measure the coverage per unit time of this evaporation source. With STM, five different regions will be scanned and within each large region five 100 nm × 100 nm areas will be imaged. The percentage of the area covered by a particle per unit area is defined as the coverage of that particle. With the image processing software "Fiji", the percentage of certain areas of the whole image can be measured. Average of the particle coverage of these 25 STM images will be taken as the particle coverage of the whole sample. The evaporation time and temperature of the particles are combined to give the coverage per unit time at that temperature for the evaporation source. This value is considered to be constant without the STM vacuum cavity being opened. In this way, the particle coverage of this sample can be calculated from the evaporation time in subsequent experiments by simply controlling the evaporation temperature.

References

[1] Omicron’s product introduction (Electronics Technical Reference Manual).

[2] Spare Parts Catalogue SPM - Scienta Omicron

[3] Kolasinski, K. W. (2012). *Surface science: foundations of catalysis and nanoscience*. John Wiley & Sons.

[4] BOC EDWARDS. Instruction Manual AUTO 306 Vacuum Coater with Turbomolecular Pumping System. Issue G,1,5.

[5] Oura, K., Lifshits, V. G., Saranin, A. A., Zotov, A. V., & Katayama, M. (2013). *Surface science: an introduction*. Springer Science & Business Media.

[6] Omicron’s product introduction (Ion Sources Manual).

[7] Createc’s product introduction (High-Temperature Cell Manual).

[8] Chen, C. J. (2021). *Introduction to Scanning Tunneling Microscopy Third Edition* (Vol. 69). Oxford University Press, USA.

Chapter 4. Self-Assembly of Co-C_{60} Cluster on Au (111) Surface

4.1 Introduction

In this chapter, the investigation of the self-assembly of Co-C_{60} on Au (111) will be presented. On an atomically flat Au (111) surface, cobalt atoms with medium coverage prefer to form bilayer clusters at the elbow sites of the DLs of Au (111). When C_{60} molecules are deposited on the cobalt/Au (111) surface at room temperature, the C_{60} molecules do not preferentially wrap around the cobalt cluster surface as expected. The vast majority of C_{60} molecules preferentially grow into large islands along the edges of the C_{60} islands, while the smaller cobalt clusters even show an inability of C_{60} adsorption. If the sample is annealed at 320°C for 30 min, the disappearance of large C_{60} islands is observed and C_{60} molecules form magic-number-like clusters around the cobalt clusters. In this chapter, the stability of the Cobalt-C_{60} like-magic number clusters and the reproducibility of this self-assembly phenomenon will be analyzed. At the same time, an attempt will be made to analyze the mechanism of this self-assembly phenomenon.

4.2 Experimental Procedure

In this experiment, two sample are prepared. For both samples, the same method are used to prepare a flat, clean gold surface with the (111) termination. Freshly cleaved HOPG is the substrate on which a 300 nm thick gold film was deposited. The deposition lasted one hour and the HOPG was kept at 350°C during deposition. The Au film on HOPG was then removed from the evaporator and transferred to the UHV system where the samples were annealed for one hour at 500°C on a manipulator. The temperature of sample on manipulator is measured by the thermocouple connecting on the manipulator. A current of 1.5 A passed through the PBN heater and the voltage across the heater was measured as 21.8 V. Upon cooling down to room temperature, the sample was sputtered with argon ions at 1.5 keV and 10 μA. One annealing and

one argon ion sputtering were performed as one round, and after thirteen rounds of sample clean-up, three additional anneals were performed, resulting in a flat, clean Au (111) substrate sample. At the end of annealing, the gold substrate is scanned by STM to determine the cleanliness and flatness.

For the first sample, cobalt was deposited on the sample using a commercial PVD evaporator made by Createch. Co rods were loaded into Al_2O_3 crucible which was heated by conductive and radiative heating from a Mo cage. Deposition was conducted when the crucible was heated to 1300°C for 8 minutes with I=7.04 A and V=10.5 V. 0.1 ML of cobalt was deposited on the Au (111) surface after 4 minutes of deposition. C_{60} molecules were deposited on the sample using a home-made Knudsen cell. The cell was maintained at 407 °C for a total of three minutes at a current of 36.7 A, depositing 0.18 ML of C_{60} molecules on the Au (111) surface. Finally, the sample was annealed and heated at 317°C for 30 minutes with I=0.9 A, V=14.0 V.

For the second sample, the same experimental procedure was used, but the specific parameters were changed somewhat due to the fact that the STM UHV cavity was opened between sample preparations and certain adjustments were made to both deposition sources. The cobalt source was run for 8 minutes at 1300°C with I=7.10 A and V=10.7 V, depositing 0.04 ML of cobalt on the Au (111) surface. the C_{60} source was deposited for 4 minutes at 403 °C with a current of 7.2 A, depositing a total of 0.1 ML of C_{60} molecules on the Au (111) surface. The samples were finally annealed and heated at 320°C for 30 minutes with I=0.9 A and V=14.2 V.

The experimental results discussed in Section 4.3 are all based on Sample 1. In contrast, the experimental results used to verify the reproducibility of the experimental phenomena in section 4.4.1 are all based on sample 2.

4.3 Experimental Results

4.3.1 Cobalt Clusters on Au (111) Surface

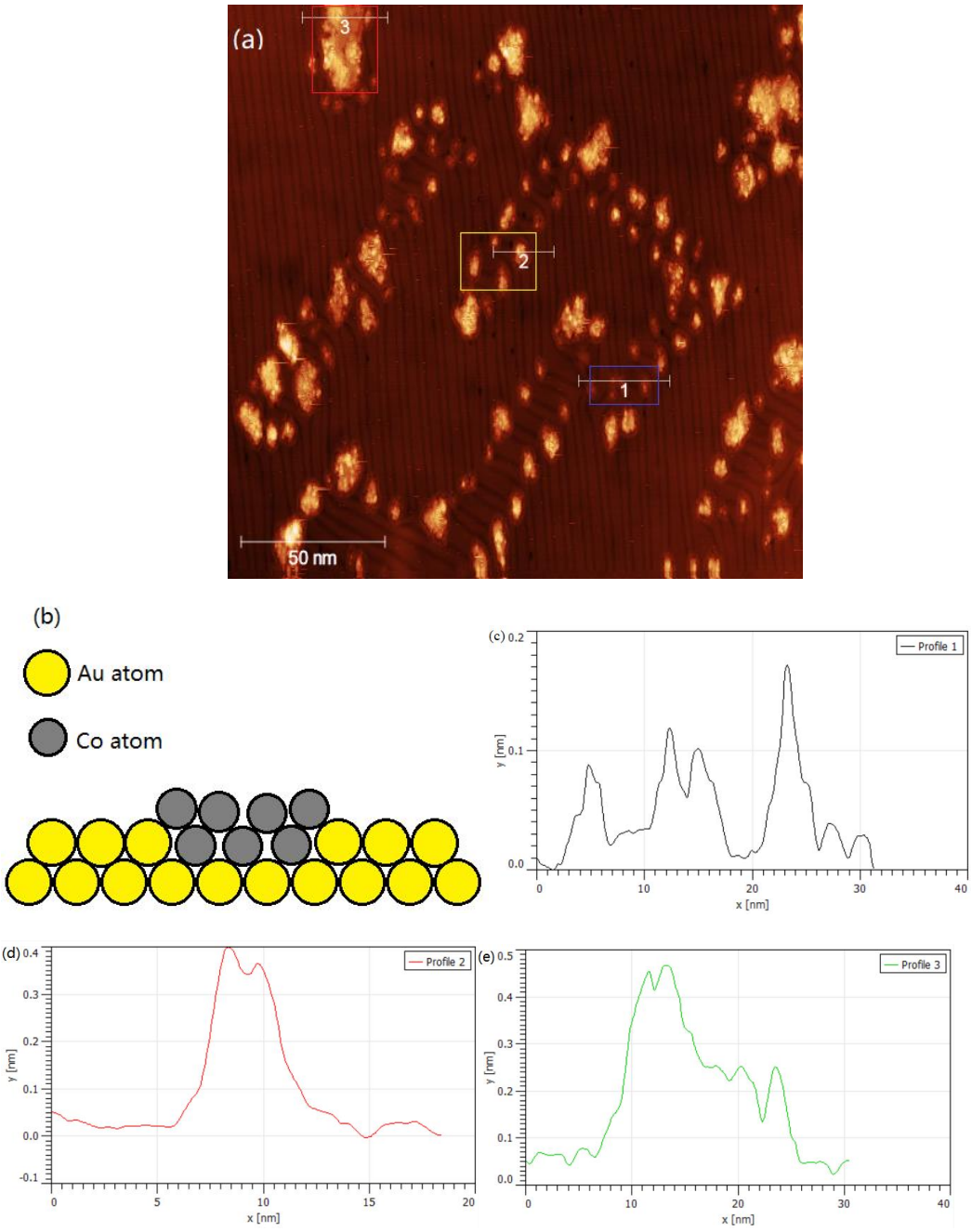

Fig. 4.1 (a) STM image of 0.1 ML cobalt on Au (111). 200 nm × 200 nm, I = 500 pA, V_{gap} = -2.0 V. The different sizes of cobalt clusters all fall on the elbow sites of the DLs. The top of the cobalt cluster shows as a rugged surface. (b) Ball model of the semi-embedded small-size cobalt cluster. (c) Height of profile 1. (d) Height of profile 2. (e) Height of profile 3. The x-axis represents distance and the y-axis represents height.

The basis for the manufacturing of Cobalt-C_{60} clusters on the Au (111) surface is the deposition of cobalt clusters nucleated at the elbow site. Therefore, the first thing for the analysis of the experimental results is to analysis the growth pattern of the cobalt clusters on the Au (111) surface. This part has already been studied in many studies [2][3] and the parts discussed below can be corroborated with these literatures.

Fig. 4.1 (a) shows an STM image of an Au (111) surface with 0.1 ML cobalt atoms. As mentioned in the literature, the cobalt atoms prefer to cluster on the elbow sites of Au (111) [1][2]. The cobalt clusters in Fig. 4.1 (a) can be classified into three types:

(1) Small-size cobalt clusters. This is represented by the cobalt cluster in the blue box in Fig. 4.1 (a). Fig. 4.1 (b) shows a simple model of this type of cobalt clusters. A small number of cobalt clusters have replaced the gold atoms at the elbow site and are embedded in the Au (111) surface. This is also consistent with the nucleation pattern of cobalt clusters growing on the Au (111) surface [4]. At this point the cobalt clusters are semi-embedded in the Au surface, as shown in the height information. The Au surface height of the cobalt clusters is less than 0.2 nm which is a single layer of cobalt atoms, as shown in Fig. 4.1 (c). These cobalt clusters correspond to the earliest nucleation stage of cobalt cluster nucleation growth.

(2) Medium-size cobalt clusters. These clusters are represented by the cobalt clusters in the yellow box in Fig. 4.1 (a). These cobalt clusters exhibit a 0.4 nm bilayer structure in terms of height information and have rugged tops, as shown in Fig. 4.1 (d). This is interpreted as a 14% lattice mismatch between cobalt and gold [3]. In the two-dimensional direction of the surface, 'medium-size' cobalt clusters are defined as those that are not interconnected with cobalt clusters nucleated at other elbow sites. These cobalt clusters correspond to the stage at which the cobalt cluster grows vertically into a stable bilayer structure.

(3) Large-size cobalt clusters, represented by the cobalt clusters in the red boxes in the figure. In parallel direction of the surface, the "large" clusters are represented by cobalt clusters that cover multiple HCP/FCC domains and incorporate multiple cobalt clusters with different nucleation sites. These clusters correspond to the stage where the cobalt clusters begin to expand in parallel directions as the cobalt atomic coverage increases. As shown in Fig. 4.1 (e), these cobalt clusters have both 0.2 nm and 0.4 nm peaks point to monolayer and bilayer structures in terms of height information, and as can also be seen in Fig. 4.1 (a), even the fraction of bilayer structures is larger than the medium-sized cobalt clusters of the second category. This illustrates that the 2D epitaxial growth of cobalt clusters is simultaneous with the atomic stacking at room temperature.

Several typical features of cobalt in the Au (111) plane can be seen in Fig. 4.1 (a): (1) Nucleate at either the bulged and pinched elbow sites. (2) Nucleation begins with the replacement of gold atoms by cobalt atoms embedded in the Au (111) surface. (3) The cobalt clusters are extremely rugged at room temperature. (4) The 2D epitaxial growth of cobalt clusters is simultaneous with atomic stacking at mid-coverages. These characteristics are in agreement with those described in the literature [1-4].

4.3.2 Deposition Growth of C_{60} on Co/Au (111)

C_{60} molecules form finger-like single molecule chains with steps on pure Au (111) surface at room temperature [14][15]. In contrast, the preliminary study of self-assembly Au-C_{60} magic number clusters [7] shows that at 110 K C_{60} molecules will nucleate at the gold clusters nucleated on elbow sites. Cobalt, as a metal that is more reactive than gold, has already shown a good affinity of C_{60} molecules in many other studies [5]. Therefore, it is expected that C_{60} molecules will nucleate surround cobalt clusters on elbow sites, as they have done in self-assembly experiments of Gold-C_{60} magic number clusters. However, in the actual analysis of the experimental data, I observed

a completely different result.

Fig. 4.2 shows an STM image of 0.18 ML C_{60} molecules deposited on an Au (111) sample with 0.1 ML cobalt atoms deposited at room temperature. Intuitively, although the interaction of C_{60} molecules with cobalt is stronger than that of C_{60} with gold [5], the vast majority of C_{60} molecules still choose to arrange with other C_{60} molecules to form large islands on Co/Au (111) sample, rather than arrange around the cobalt clusters. This is the most fundamental difference with the behavior of C_{60} on Au (111) substrates with gold clusters [6][7].

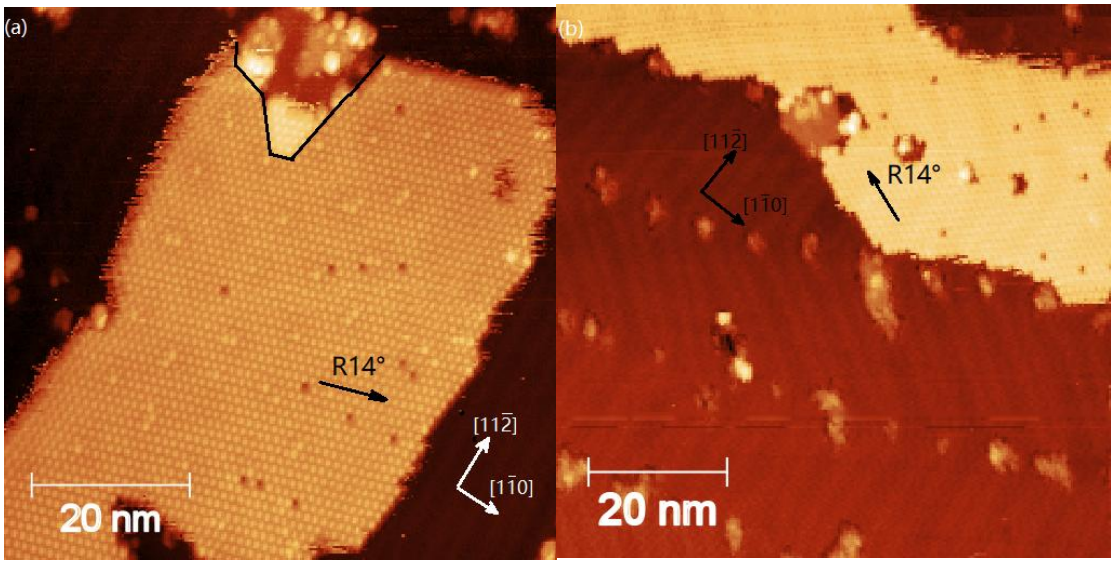

Fig. 4.2 STM image of 0.18 ML C_{60} deposited on Co-Au (111). (a) 70 nm × 70 nm, I=500 pA, V_{gap}=-2.0 V. The monolayer C_{60} grows along the step of the large-size cobalt cluster and partially covers the top of the monolayer. Arrangement direction of C_{60} is R14°. A pair of vertical vectors show the crystal orientation of the gold substrate. The edge of the cobalt cluster covered by the C_{60} island is marked by the black line. (b) 80 nm × 80 nm, I=500 pA, Vgap=-2.0 V. The monolayer C_{60} shows a clear low adsorption rate behavior towards the cobalt clusters. At the same time, this low adsorption rate behavior disappears around the larger cobalt clusters. Arrangement direction of C_{60} is R14°. A pair of vertical vectors show the crystal orientation of the gold substrate. Due to the instability of the STM equipment, there is a difference in the resolution of the two images.

On Au (111) substrate with Co cluster, C_{60} will aggregation into monolayer hexagonal close-packed island which cross the DLs. These can be seen in Fig. 4.2 and are similar to the behavior of C_{60} on pure Au (111) [18]. In contrast, two different modes of cobalt-C_{60} contact have been observed at the junction of C_{60} islands with cobalt clusters in Fig. 4.2. When the edges of the C_{60} islands are in contact with the small or medium size cobalt clusters, the clusters do not exhibit strong interactions with the C_{60}. The C_{60} islands do not change the arrangement extending from the step-edge and have very limited or no contact with the clusters. For small and medium-size clusters. When large size cobalt clusters are adjacent to C_{60} island, the C_{60} will be in full contact with the cluster. The C_{60} island will even extend across the step-edge to the top of the cluster, as shown in Fig. 4.2 (a). (The definition of 'large' and 'small' cluster sizes is given in Section 4.3.1).

Two credible explanations can be given for this phenomenon: (1) Due to the lattice mismatch between the cobalt clusters and the gold substrate, cobalt clusters are rugged. Unlike the highly regular steps and surfaces of the gold cluster on Au (111), the rough surface of the cobalt cluster results in only a part of sites being in sufficient contact with C_{60} molecules to adsorb C_{60}. Small or medium size cobalt clusters have fewer adsorption sites and therefore cannot adsorb C_{60} molecules. Large size clusters have more adsorption sites and are closer to the structure of cobalt crystals, so they can adsorb C_{60} with better efficiency. (2) Another possibility that the cobalt clusters are unable to adsorb C_{60} is that there may be some kind of barrier preventing C_{60} from diffusing around the clusters. Cobalt nucleation on the Au (111) surface is achieved by replacing gold atoms with cobalt atoms embedded at the elbow site. The nucleation of the cobalt cluster will therefore change the atomic arrangement of the gold surface surrounding it. If it is assumed that the nucleation of cobalt clusters will create a potential barrier around the clusters which cannot be crossed by C_{60} molecules at room temperature, then this hypothetical potential barrier would be a reason for the adsorption of C_{60} molecules to the clusters. The subsequent cobalt atoms grow on the

Au (111) surface along the step and don't cause more embedding. The large-size cobalt clusters therefore cover the area where the potential barrier exists, thus preventing the negative effects of potential barriers to C_{60} adsorption It should be noted that there will be no calculations based on first principles in this article to discuss whether this potential barrier is real and whether it will be crossed by C_{60} at room temperature. In the subsequent sections, the discussion of the experiment results based on STM will be the main means of confirming the validity of this hypothesis. The specific analysis and discrimination of the explanations will be discussed in subsequent sections.

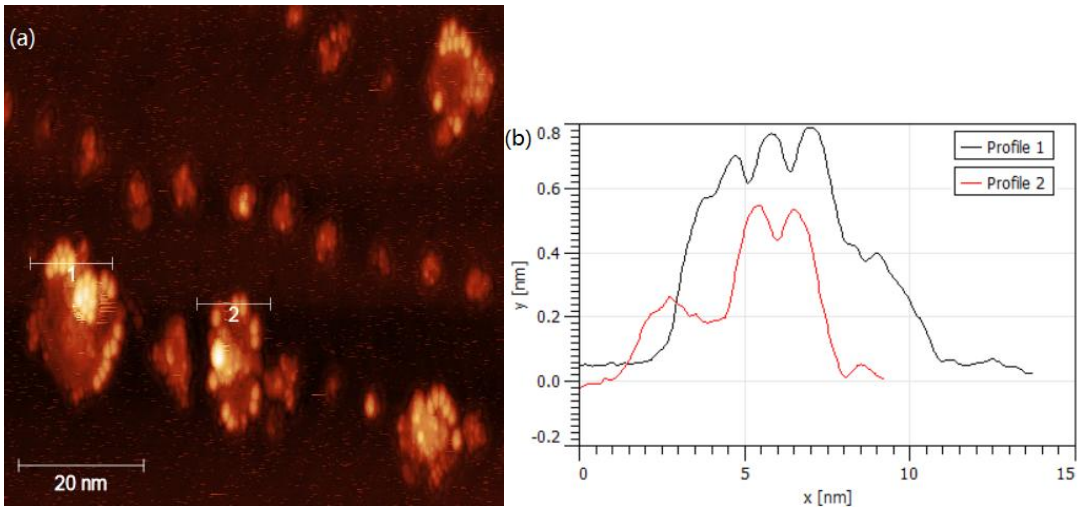

Fig. 4.3 (a) STM image of 0.18 ML C_{60} deposited on Co-Au (111). 80 nm × 80 nm, I=500 pA, V_{gap}=-2.0 V. Some C_{60} molecules are adsorbed on the large-size cobalt clusters and small-size clusters are all bare. (b) Black lines in the height information of the STM image correspond to profile 1 in (a) and red lines to profile 2. The height information shows that there is a 0.2 nm height difference between the C_{60} molecules at the edges and those on the top, indicating that both the top and the step of the cobalt cluster are possible C_{60} adsorption sites. The x-axis represents distance and the y-axis represents height.

In Fig. 4.3, another Cobalt-C_{60} binding pattern different with large islands of C_{60} is shown. A single or small number of C_{60} molecules are adsorbed around the cobalt cluster. As can be seen in Fig. 4.3(a), there is a clear adsorption of C_{60} molecules

around the large sized cobalt clusters. In Figure 4.3(b), a height difference of 0.2 nm between profile 1 and profile 2 can be seen. This proves that both the edge of the cobalt cluster and the top of the cobalt cluster are possible C_{60} adsorption sites. The small-size clusters in Fig. 4.3(a) are still bare, proving that the adsorption of C_{60} molecules only occurs on the large-size cobalt clusters. This phenomenon also indicates that the larger size cobalt clusters have a stronger adsorption ability for C_{60} molecules while the smaller and medium size clusters do not. This difference in adsorption capacity can also be explained by both of the models mentioned above.

It is worth noting that the height of monolayer C_{60} in Fig. 4.3 (b) is about 0.5 nm, which is a large deviation from the theoretical value of 0.7 nm for the C_{60} molecule [8-10]. In the STM scanning, the height of the molecule is directly linked to the material of the substrate. On HOPG substrates, the molecular height of C_{60} is much close to the theoretical value due to the close structure of graphite to C_{60}. And with metal substrates, the measured height of the C_{60} molecule is reduced to some extent [19]. Based on experimental experience, C_{60} molecules of 0.5-0.7 nm height have been observed on gold substrates. Considering that the sample is always in UHV, no other material is introduced into the surface besides C_{60}, and C_{60} is deposited at room temperature without any additional treatment, it can be assumed that 0.5 nm is a trustworthy figure for the molecular height of a monolayer of C_{60}.

4.3.3 Annealed Samples

Since direct C_{60} deposition did not form the expected Cobalt-C_{60} clusters, annealing the sample at 320°C is tried in order to observe some changes. 320°C was chosen arbitrarily and is not an accurate value. The only thing that worth to noted is the desorption temperature of C_{60} from the Au (111) surface. The critical temperature for desorption of the first layer C_{60} from Au (111) substrate is 500°C, while the second layer C_{60} desorb from the underlying C_{60} islands at 300°C. [20] Therefore, a temperature at which the C_{60} molecules could diffuse completely on the gold substrate

without desorption from the gold substrate is chosen in order to expect to observe a significant change.

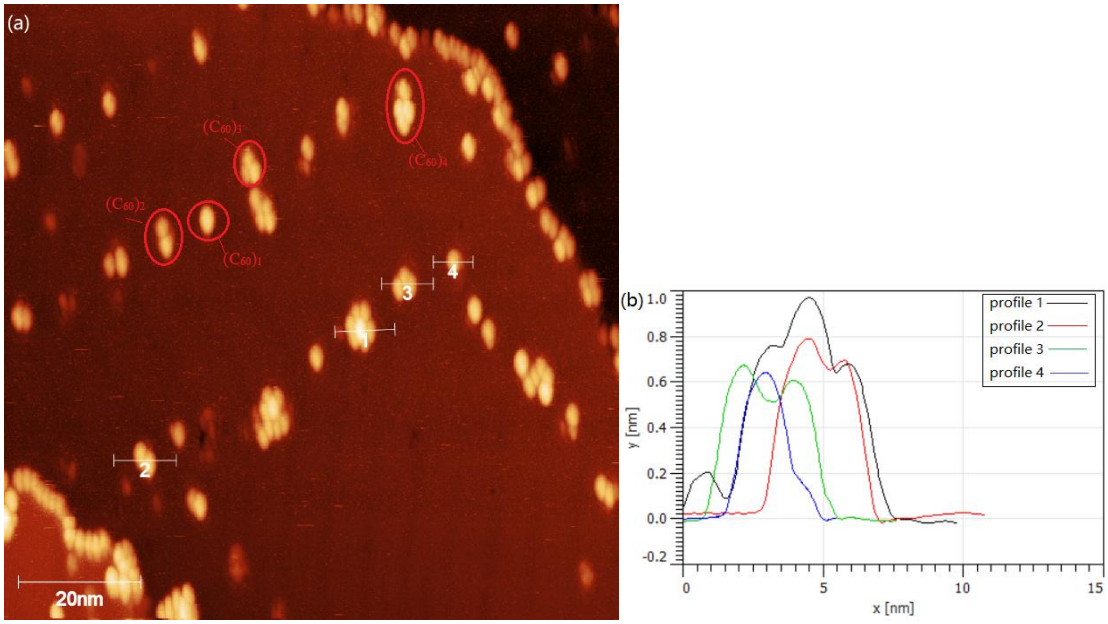

Fig.4.4 (a) STM image of 0.18 ML C_{60} deposited on Co-Au (111), Annealed at 320°C for 30 min. 100 nm × 100 nm, I=500 pA, V_{gap}=-2.0 V. After annealing, the large C_{60} monolayer has disappeared and forming many small Cobalt-C_{60} clusters. A structure very similar to the magic number $(Au)_{19}$-$(C_{60})_7$ can be observed in the figure, but mostly the Cobalt-C_{60} degree is more disordered. Cobalt-C_{60} clusters have various combination numbers and typical examples of $(C_{60})_1$ to $(C_{60})_4$ are marked in the diagram. (b) Height information of the STM image, where the black line corresponds to profile 1, the red line to profile 2, the blue line to profile 3 and the green line to profile 4 of the above figure. The x-axis represents distance and the y-axis represents height.

After annealing the sample in UHV at 320°C for 30 minutes and cooling back to room temperature, the structure of the Co-C_{60}/Au (111) sample changed significantly as shown in Fig. 4.4. The most intuitive change is the disappearance of the large C_{60} islands in the figure, with the C_{60} molecules no longer aggregated together but adsorbed by the individual cobalt clusters to form Cobalt-C_{60} combinations.

In Fig. 4.4, a structure very similar to the typical magic number Au-C_{60} combination

is shown [6][7]. From the height information of Fig. 4.4 (b), it can be seen that the six surrounding darker C_{60} molecules have a height of about 0.7 nm, while the brighter atom in the center is 0.2 nm higher than the surrounding C_{60} atoms, close to monolayer cobalt cluster. It indicates that these C_{60} molecules fall on the Au (111) surface and are in contact with the steps of the cobalt cluster, while the highlighting molecule is on the monolayer cobalt clusters. It points to an image that a C_{60} located on monolayer Co clusters wrapped by 6 C_{60} molecules. At the same time, however, as can be seen in Fig. 4.4, such a complete $(C_{60})_7$ structure is rare. Structures from $(C_{60})_1$ to $(C_{60})_4$ can be found in the diagram, and furthermore, those bare cobalt clusters in the figure can also be considered as $(C_{60})_0$. In Fig. 4.5, clusters aggregate more C_{60} molecules and have more irregular structure can also be found, indicating a high level of freedom in the structure of the Cobalt-C_{60} clusters. Larger size cobalt-C_{60} clusters are found in Fig. 4.5 (c), which indicates that after annealing, all sizes of cobalt clusters can adsorb C_{60} molecules. Meanwhile, as can be seen from Fig. 4.5(b), although the large C_{60} islands disappear after annealing, the one-dimensional C_{60} chains adsorbed on the edges of the gold steps still remain. This indicates that on the annealed sample the step-edge of Au (111) is still the C_{60} adsorption site.

It is also worth noting that in Fig. 4.5, many unusual steps of gold islands can be seen, such as the semi-circular protrusion in the red boxed region in Fig. 4.5(a), and the trapezoidal gold island in the blue boxed region in 4.5 (b). Both of which are structures rarely seen by PVD manufactured Au (111) film. This structure is similar to the gold islands re-formed by expelled gold atoms due to cobalt sinking into the gold surface after annealing [11]. 0.15 nm highly semi-embedded cobalt clusters can be observed in Fig. 4.5 (c) and the height information of Fig 4.5 (d), which also can be seen at the bottom left corner of Fig. 4.5 (a). These prove that during the annealing of the sample, some of the cobalt did sink into the gold surface and the expelled gold atoms were rearranged on the surface to grow into these small areas of gold islands. The area of the anomalously shaped gold island is large, suggesting that more cobalt

clusters may have sunk than remained on the gold surface. It is possible that many of the cobalt clusters were completely sunken. At the bottom of all three images, there are image stretching problems, which is a drift phenomenon caused by dragging the scanning probe in STM scanning. The lines elongated laterally around some C_{60} molecules and at the top of Fig. 4.5 (a) are due to erroneous movement of the probe caused by the dramatic change in height on the surface.

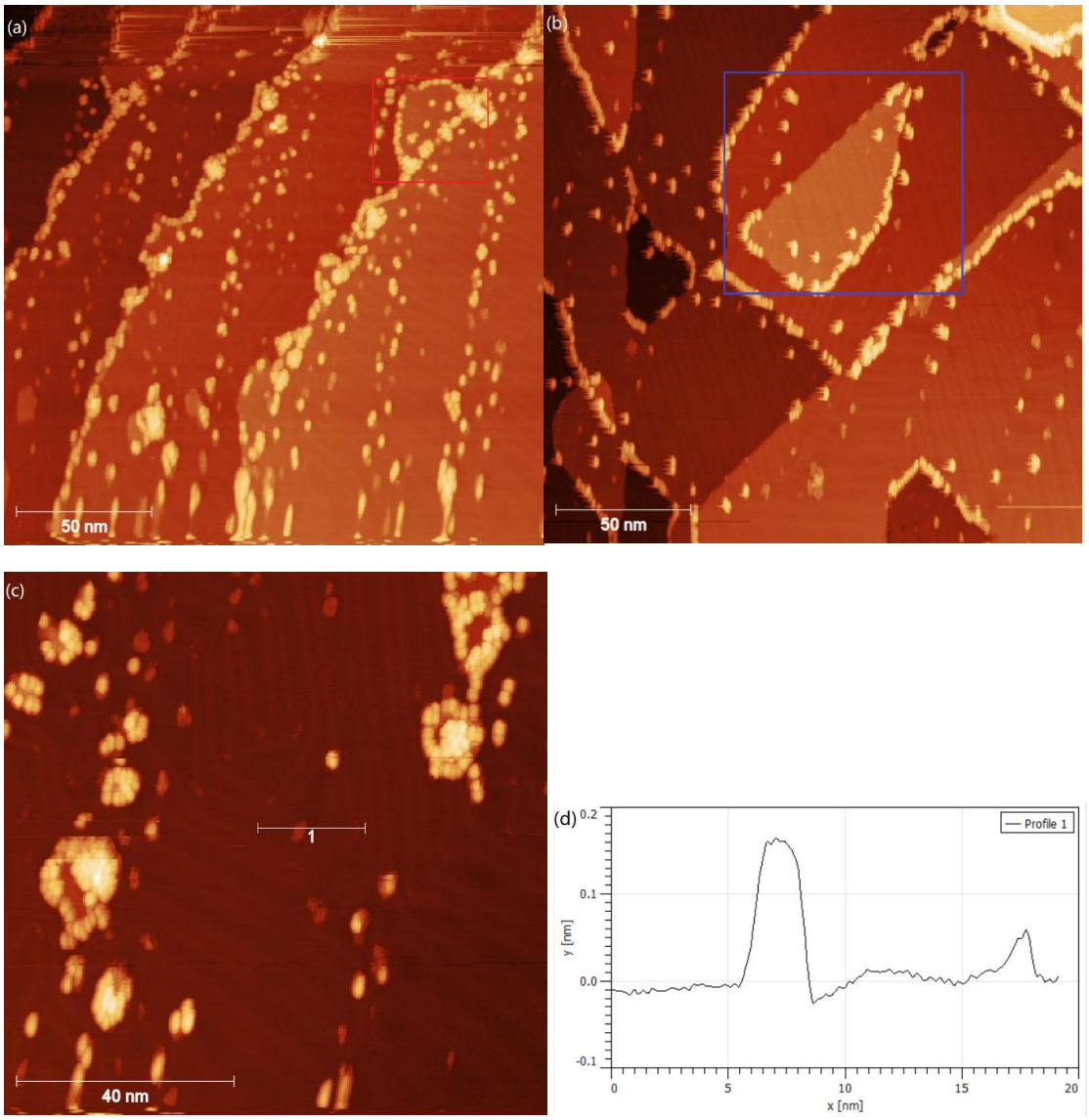

Fig. 4.5 (a)-(c) STM image of 0.18 ML C_{60} deposited on Co-Au (111), annealed at 320°C for 30 min. 200 nm × 200 nm, I=500 pA, V_{gap}=-2.0 V. (a) There is a distinct semicircular protrusion in the red boxed from the gold step, which is uncommon in PVD growth of gold films. There are also some bare cobalt islands found in the bottom left corner of the picture. (b) There is an unnatural trapezoidal gold island in the blue box region. The same semicircular protrusion as in (a) is due to

the fact that cobalt sinks into the gold surface upon heating and the expelled gold atoms re-form the gold island on the surface. (c) A region with bare cobalt clusters. (d) Height information of profile 1 in (c). The x-axis represents distance and the y-axis represents height.

4.4 Analysis and Discussion

As seen above, at room temperature, most of the C_{60} molecules remain part of extended C_{60} islands rather than adsorbed by cobalt. But after annealing at 320°C for 30 min, the large C_{60} islands disappear and form many small Cobalt-C_{60} clusters.

In the discussion below, the first concern is the reproducibility of this phenomenon and whether it is a general behavior rather than an accident. Secondly, there will be a discussion of the stability of this structure. Finally, an attempt will be made to explain the mechanism of these structure evolution occurring, based on the available experimental results.

4.4.1 Reproducibility Analysis

As a possible act of surface self-assembly, the first question is whether this is a reproducible phenomenon. Whether it is triggered by experimental manipulations that I'm cognizant of, rather than by some error or accidents that is not recorded. To do this, I re-prepared a gold substrate and deposited 0.04 ML of cobalt atoms on it, followed by depositing 0.1 ML C_{60} molecules on top. As can be seen by the STM images below, although the coverage of the cobalt and C_{60} molecules changed somewhat, the combination characteristics of the C_{60} molecules with the cobalt clusters did not change.

The behavior of the unannealed C_{60} molecules on Co/Au (111) surface can be seen very typically in Fig. 4.6 (a). The C_{60} molecules mostly arrange into C_{60} islands, with some individual C_{60} molecules bound to the large-size cobalt clusters. At the same time, there are many exposed small/middle-size cobalt cluster edges that are not

occupied by C_{60}. In Fig. 4.6 (b), two larger sized cobalt clusters can be seen with some C_{60} molecules adsorbed on their edges. In Fig. 4.6 (c), completely wrapped cobalt clusters by C_{60} molecules can be seen. As found in Section 4.3.2, this full coverage is closely associated with large islands of C_{60}. At the same time, defective vacancies in C_{60} islands appear in

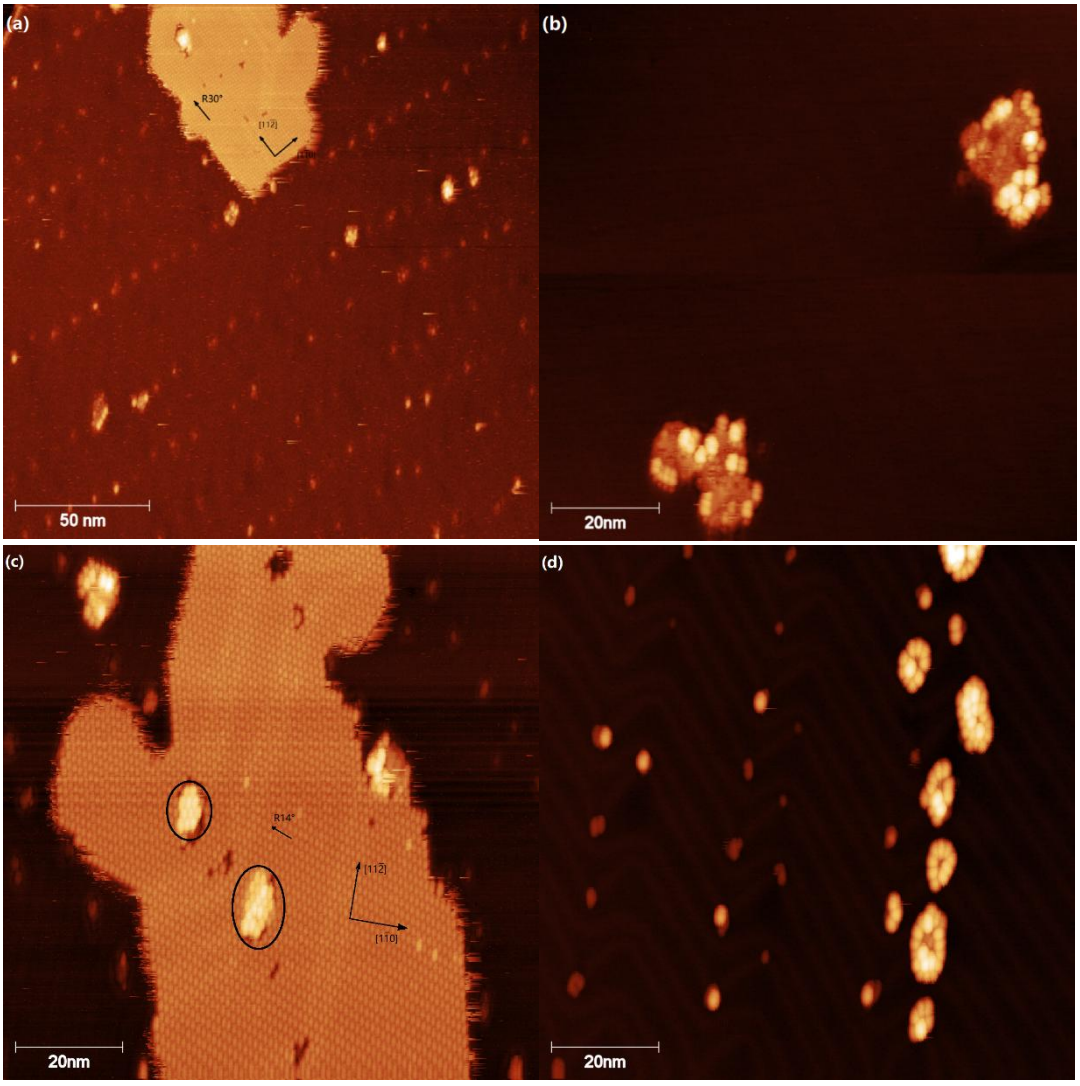

Fig. 4.6 STM image of 0.1 ML C_{60} deposited on Co/Au (111), I=500 pA, V_{gap}=-2.0 V. (a) The cobalt cluster forms a dotted array at elbow sites, with the majority of C_{60} molecules aggregating into large monolayer C_{60} islands. Arrangement direction of C_{60} is R30°. 200 nm × 200 nm. (b) Both of the larger size cobalt clusters in the figure have C_{60} molecules adsorbed on their edges. 100 nm × 100 nm. (c) The cobalt clusters can be seen completely covered by C_{60} molecules which are tightly attached to the C_{60} islands, while the separate cobalt clusters in the upper left corner

have only isolated C_{60} molecules adsorbed. Arrangement direction of C_{60} is R14°. 100 nm × 100 nm. (d) Annealed at 320°C for 30 min. On the left side of the image there are many bare cobalt clusters. Some clusters have single C_{60} molecule adsorbed. On the right side of the image, larger Cobalt-C_{60} clusters adsorbing more C_{60} molecules can be seen. 100 nm × 100 nm.

both Fig. 4.6 (a) and Figure 4.6 (c). These vacancies, arranged in a dotted pattern, are all at the elbow sites. These vacancies are the defects due to the inability of the cobalt clusters to adsorb C_{60} molecules. Meanwhile, the size of the vacancies suggests that they all belong to small or medium-sized cobalt clusters.

A comparison of these images with Section 4.3.2 shows that the behaviors of C_{60} molecules on the Co/Au (111) surface without annealing is highly likely to be reproducible. These behaviors include that C_{60} molecules are clustered into large islands, small and medium-size cobalt clusters are bare, and the edges of large-size cobalt clusters are partially attached or even completely covered by C_{60}.

After annealing at 320°C for 30 min, as shown in Fig. 4.6 (d), similar to the situation in 4.3.3, large islands of C_{60} disappear and all of the C_{60} molecules wrap around the cobalt clusters to form Cobalt-C_{60} clusters. Unlike in Section 4.3.3, in Fig. 4.6 (d), there are more cobalt clusters without the C_{60} molecules and the Cobalt-C_{60} clusters are also larger compared to the first sample.

The comparison in the figure shows that although the coverage varies, similar surface structure evolution occurs for the different samples after annealing at 320 °C for 30 min. It suggests that the phenomenon of C_{60} islanding alone on the unannealed Co/Au (111) samples and the self-assembly of Cobalt-C_{60} clusters after annealing at 320°C should be a stable phenomenon with repeatability.

4.4.2 Stability Analysis

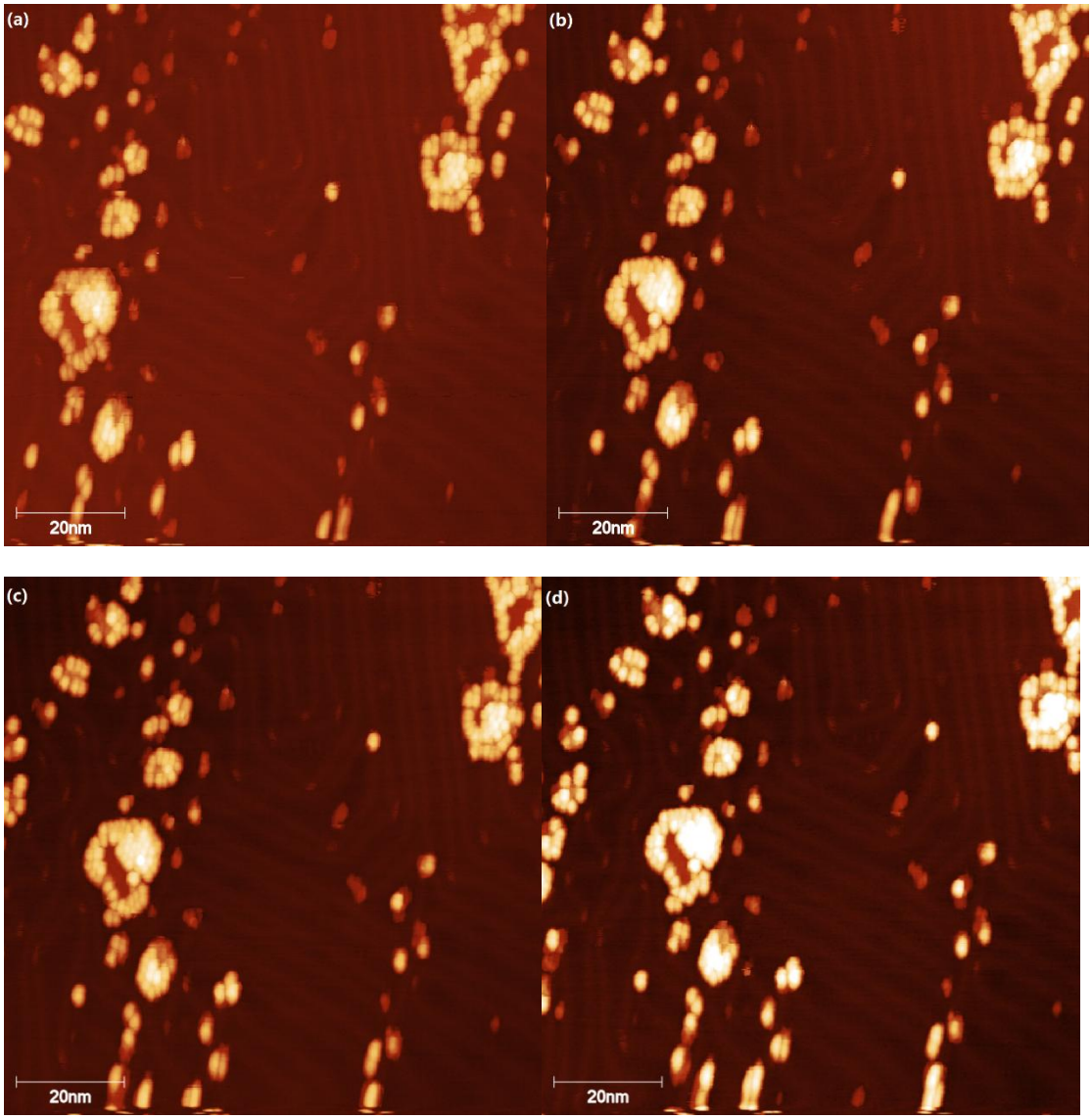

Fig. 4.7 STM image of sample 1, 0.18 ML C_{60} deposited on Co/Au (111), annealed at 320 °C for 30 min. 100 nm × 100 nm, I=500 pA, V_{gap}=-2.0 V. The above four images are obtained by successive scans of the same area. Each round of scanning takes 2 min, with no gaps between each scanning.

The interaction between 2 single C_{60} is not strong enough on Au (111) to refuse diffusion. At room temperature, C_{60} may diffuse from the edge of the island at any time which is represented as a blurring of the island edge in the STM images [12]. Whereas for the Co-C_{60} clusters, the C_{60} molecules at the edges of cobalt clusters are

clear as seen in the Fig. 4.7. Fig. 4.7 shows a series of successive scans of the annealed Co-C_{60} sample against the same location. It can be seen that with constant scanning of the surface, C_{60} molecules are not disturbed by the probe to deviate from its position. These illustrate the strength of the Cobalt-C_{60} bond and the stability of this structure at room temperature. Similar to Fig. 4.5, the stretching of the image below the image in Fig. 4.7 is also due to the drift effect of the probe.

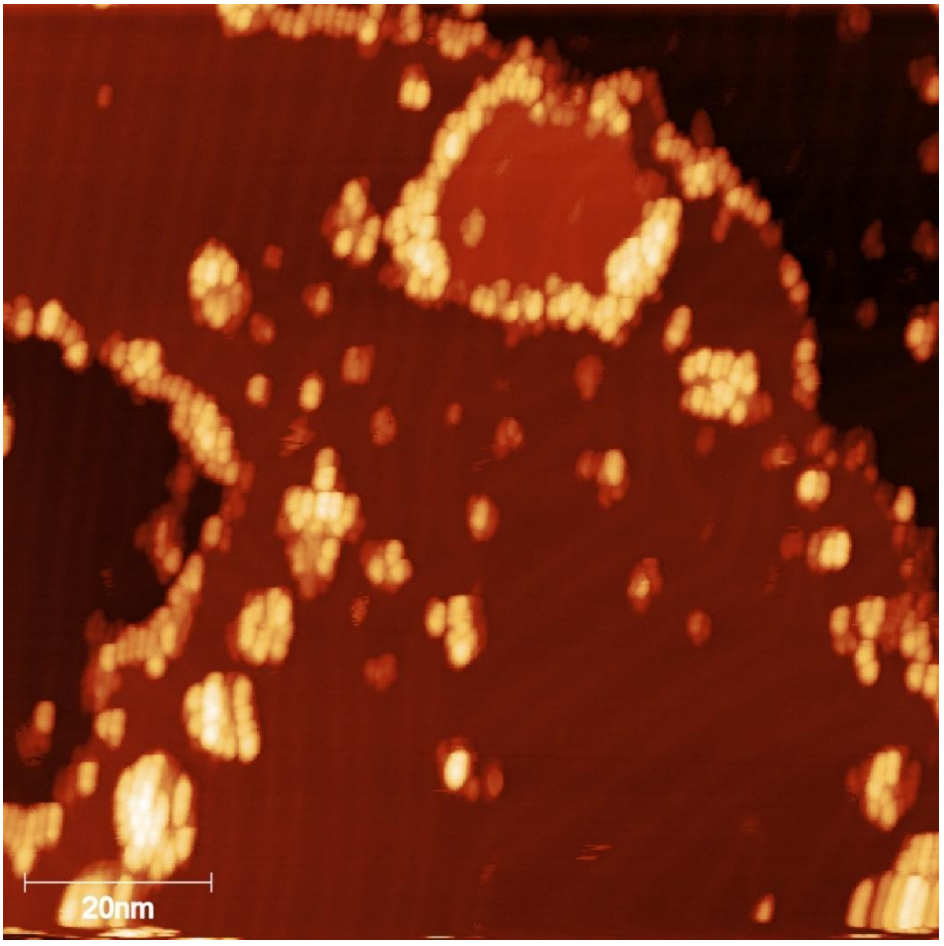

Fig. 4.8 STM image of 0.1 ML C_{60} deposited on Co/Au (111), annealed at 320°C for 30 min. 100 nm × 100 nm, I=500 pA, V_{gap}=-2.0 V. Sample has been left in UHV system for one week at room temperature.

While the above evidence suggests that the cluster structure is highly stable and does not change dramatically over each scanning lasting 2 min. However, additional evidence is required to support whether the Co-C_{60} structure will evolute over longer

time scale. Fig. 4.8 shows an STM image of Sample 1 which has been kept in UHV for one week at room temperature. A comparison with the STM image in Section 4.3.3 shows that although it can't prove that no little creep occurs over the long-time scanning, the overall characteristics of the Cobalt-C_{60} clusters are maintained. This indicates the long-range time stability of the Cobalt-C_{60} cluster.

In these experiments, it is possible to guarantee the stability of Cobalt-C_{60} clusters at room temperature based on current data. However, the experiments for stability at high temperatures, especially above 320 °C, are still lacking.

4.4.3 Mechanism Analysis

At beginning of the experiment design, the Cobalt-C_{60} combinations were expected to be obtained at room temperature, considering the high reactivity of cobalt. However, in experiments, the small/medium-size cobalt clusters show a reducing adsorption effect on C_{60}, while the adsorption of C_{60} for cobalt clusters is only partially shown on the large-size clusters. The largely expected Cobalt-C_{60} clusters are only observed after 320 °C annealing. Therefore, the low adsorption rate of C_{60} molecules by small/medium-size cobalt clusters at room temperature and the role played by annealing in the formation of cobalt-C_{60} clusters become the most worthwhile issues.

Simply, the key to the self-assembly of Au-C_{60} magic number clusters is lying in the fact that both the gold atoms and the C_{60} molecules have enough surface diffusion rate on the gold surface to self-refine. When the gold clusters are replaced with cobalt clusters, it's clear that the diffusion rate of C_{60} on the Au substrate does not change, and the interaction between cobalt atom and C_{60} molecule is stronger than that of Au-C_{60} even without the formation of a cobalt-carbon chemical bond [5]. It is simple to know by comparison that the difference in the nucleation patterns of C_{60} molecules at room temperature should be attributed to the different properties of cobalt and gold clusters on the gold substrate.

The differences between cobalt clusters and gold clusters at the elbow sites on Au (111) are mainly reflected in the following points: 1) The nucleation mode of cobalt clusters is that cobalt atoms replace gold atoms embedded in the elbow site [4], while gold clusters are formed by surface stacking. 2) Due to the lattice mismatch between gold and cobalt, gold clusters are ordered and densely arranged while cobalt clusters are loose and rugged. 3) The reactivity of cobalt is much higher than that of gold and is more likely to adsorb gas molecules. Based on these three points, three possible explanations for the reducing adsorption effect of cobalt clusters on C_{60} molecules at RT are proposed. These are two hypotheses already mentioned above: (1) Potential barrier due to the local reconstruction caused by the embedding of the cobalt clusters. (2) Inefficient contact between the cobalt clusters and the C_{60} molecules due to the rugged surface of the cobalt clusters. The other explanation is more commonplace which is not mentioned above: (3) The cobalt cluster is polluted with gas.

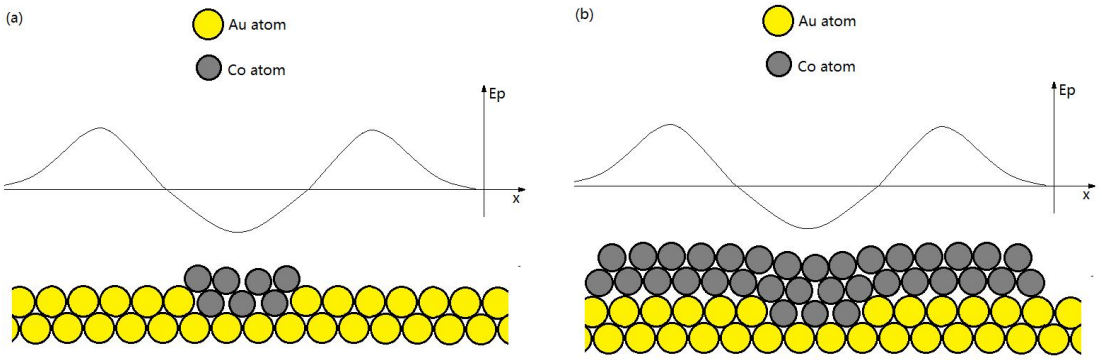

Fig. 4.9 A simple ball model of cobalt cluster on Au (111) surface and the approximate trend of the surface potential energy. The diagrams are only schematic while the atomic arrangements, potential barrier heights and other values are all inaccurate. (a) Small-size Co cluster and the potential barrier. (b) Large-size Co cluster and the potential barrier covered by cobalt.

For the first explanation, since the atom size of the cobalt cluster is slightly smaller than that of the gold atoms, the cobalt atoms replace Au atoms at elbow sites may cause a local reconstruction of the gold atoms around the cobalt atoms. This local

reconstruction may lead to a new potential barrier around the cobalt cluster, as shown in Fig. 4.9 (a). It should be noted that no calculations will be made in this part, and I will not calculate the existence and height of the potential barriers from first principles, but will attempt to analyze the validity of this hypothesis from the images obtained by the STM technique. Assuming that the embedding of cobalt clusters does lead to a potential barrier that cannot be crossed by C_{60} diffusion at room temperature, the low adsorption rate of C_{60} molecules by small and medium-size clusters at room temperature can be explained. If, on the other hand, the cobalt cluster size increases further, as shown in Fig. 4.9 (b), further cobalt atom growth is accomplished in the form of surface stacking. The increase in cluster size is not accompanied by an increase in the C_{60} potential range. In other words, the larger-size clusters will cover the potential barriers and thus re-express their adsorption capacity to C_{60}. In contrast, during annealing, C_{60} molecules at high temperatures gain higher kinetic energy to cross the potential barrier which explains the appearance of Cobalt-C_{60} clusters.

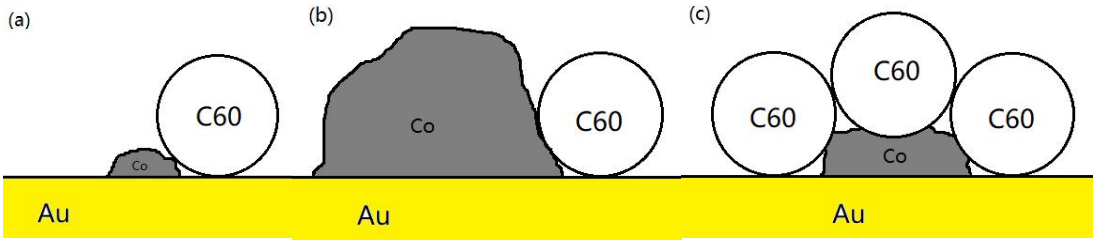

Fig. 4.10 A diagram of the inefficient contact model. (a) For small cobalt clusters, the contact between cobalt and C_{60} is limited and the interaction is weak. (b) For large cobalt clusters, the cobalt cluster has more sites for adsorption of C_{60} molecules. (c) At high temperatures, the thermal motion of the cobalt atoms is enhanced and the cobalt clusters are able to fit more closely to the C_{60} molecules.

For the second explanation, at room temperature, the gold atoms have a very high diffusion speed on the gold surface, so it is extremely difficult to form gold clusters independently [13], while at low temperatures, the gold clusters at the elbow sites are close-packed [6]. This means that when a gold cluster adsorb a C_{60} molecule, the C_{60}

molecule will interact with multiple gold atoms and the edges of the cluster are more easily self-refining at RT. This will not happen on the cobalt clusters. Cobalt clusters are loose and rugged on the Au (111) surface due to the 14% lattice mismatch between cobalt and gold. On the other hand, the strong interaction between cobalt atom result in no self-refinement. In a large number of previous experiments on Cobalt-C_{60} aggregates [16][21], when both are vaporized by the laser, the cobalt and C_{60} were mixed through the gas phase, which meant that the cobalt and C_{60} could be in full contact with each other. Whereas for loose cobalt clusters on gold surfaces, the contact efficiency between the cobalt and C_{60} molecules is very low when the C_{60} molecules diffuse to the edges of the cobalt clusters. At this time, the stronger interactions between cobalt atoms and C_{60} can't lead to a strong interaction between cobalt clusters and C_{60} molecules. What's more, C_{60} never acts as an η5- or η6- ligand but only η2 and η'2 ligands exist in Co-C_{60} clusters [16][17]. This may indicate that the cobalt adsorption may also have a requirement for the orientation of C_{60} molecule. This asks higher demands on the cluster shape. In contrast, for the larger multilayer cobalt clusters, as the size of the clusters increases, their structure becomes closer to an ordered arrangement and some suitable surfaces may exist to adsorb C_{60} molecules. Thus, large-size Co clusters re-express their adsorption capacity to C_{60}. At high temperatures, the enhanced thermal motion of the cobalt atoms allows for a self-refinement to adsorb C_{60} molecules, thus improving the adsorption capacity for C_{60} molecules. Figure 4.10 briefly represents the low contact efficiency of small cobalt clusters, the adsorption capacity of certain sites of large-size cobalt clusters, and the self-refinement of cobalt clusters after annealing.

For the third explanation, since the deposition of cobalt clusters is not done at the same time with the deposition of C_{60}, there is often an interval of several hours between them. Considering that cobalt clusters are much more reactive than gold, they may adsorb residual gas molecules in the vacuum chamber and thus passivate the surface. This passivation is likely to be incomplete considering the very low gas

density in the ultra-high vacuum system. So, there is a higher probability of large cobalt clusters to retain the bare, unpolluted atoms and thus retain an adsorption capacity for C_{60}. Under high temperature annealing, the gas molecules desorb from the cobalt clusters, leading to a reactivity rising and the formation of Cobalt-C_{60} clusters.

As can be seen from the above parts, all the three hypotheses can be used to explain the low adsorption rate of C_{60} by the small cobalt clusters and the self-assembly behavior after annealing. Therefore, all three hypotheses should be considered as possible optional theories, if only consider the experimental data covered in this chapter. In the following chapters, further analysis of these hypotheses will be discussed through a series of extended experiments.

4.5 Summary

Based on studies related to the self-assembly of Au-C_{60} magic number clusters, I hoped to manufacture similar Cobalt-C_{60} clusters. However, in this chapter, it's shown that, at room temperature, the C_{60} molecules do not wrap around the cobalt clusters as expected, but rather aggregate more into large C_{60} islands. After annealing at 320°C for 30 minutes, the C_{60} islands will dissipate and the C_{60} molecules will wrap around the cobalt clusters to form Co-C_{60} clusters. By reproducible experiments, the reproducibility of this phenomenon and the stability of the Cobalt-C_{60} clusters on the time scale have been demonstrated. For the low adsorption rate of C_{60} molecules by cobalt cluster and the self-assembly of Cobalt-C_{60} cluster, three possible hypotheses to explain the experimental phenomena have been given: the potential barrier model, the inefficient contact model and the gas pollution model. All the three hypotheses can explain the present experimental phenomena. Therefore, the analysis and selection of these hypotheses will be discussed in detail in the next chapter.

References

[1] Meyer, J. A., Baikie, I. D., Kopatzki, E., & Behm, R. J. (1996). Preferential island nucleation at the elbows of the Au (111) herringbone reconstruction through place exchange. *Surface science*, *365*(1), L647-L651.

[2] Voigtländer, B., Meyer, G., & Amer, N. M. (1991). Epitaxial growth of thin magnetic cobalt films on Au (111) studied by scanning tunneling microscopy. *Physical Review B, 44*(18), 10354.

[3] Speckmann, M., Oepen, H. P., & Ibach, H. (1995). Magnetic domain structures in ultrathin Co/Au (111): on the influence of film morphology. *Physical review letters, 75*(10), 2035.

[4] Oviedo, O. A., Leiva, E. P. M., & Mariscal, M. M. (2008). Diffusion mechanisms taking place at the early stages of cobalt deposition on Au (111). *Journal of Physics: Condensed Matter, 20*(26), 265010.

[5] Avramov, P., Naramoto, H., Sakai, S., Narumi, K., Lavrentiev, V., & Maeda, Y. (2007). Quantum Chemical Study of Atomic Structure Evolution of Co_x/C_{60} ($x \leq 2.8$) Composites. *The Journal of Physical Chemistry A, 111*(12), 2299-2306.

[6] Kaya, D., Gao, J., Fard, M. R., Palmer, R. E., & Guo, Q. (2018). Controlled Manipulation of Magic Number Gold–Fullerene Clusters Using Scanning Tunneling Microscopy. *Langmuir, 34*(28), 8388-8392.

[7] Xie, Y. C., Tang, L., & Guo, Q. (2013). Cooperative assembly of magic number C 60-Au complexes. *Physical Review Letters, 111*(18), 186101.

[8] Dresselhaus, M. S., Dresselhaus, G., & Eklund, P. C. (1996). *Science of fullerenes and carbon nanotubes: their properties and applications*. Elsevier.

[9] Yannoni, C. S., Johnson, R. D., Meijer, G., Bethune, D. S., & Salem, J. R. (1991). Carbon-13 NMR study of the C_{60} cluster in the solid state: molecular motion and carbon chemical shift anisotropy. *The Journal of Physical Chemistry, 95*(1), 9-10.

[10] Curl, R. F., & Smalley, R. E. (1991). Fullerenes: the third form of pure carbon. *Sci. Am*, 265, 54.

[11] Padovani, S., Scheurer, F., & Bucher, J. P. (1999). Burrowing self-organized cobalt clusters into a gold substrate. *EPL (Europhysics Letters), 45*(3), 327.

[12] Guo, S., Fogarty, D. P., Nagel, P. M., & Kandel, S. A. (2004). Thermal diffusion of C_{60} molecules and clusters on Au (111). *The Journal of Physical Chemistry B, 108*(37), 14074-14081.

[13] Lang, C. A., Dovek, M. M., Nogami, J., & Quate, C. F. (1989). Au (111) autoepitaxy studied by scanning tunneling microscopy. *Surface Science Letters, 224*(1-3), L947-L955.

[14] Gardener, J. A., Briggs, G. A. D., & Castell, M. R. (2009). Scanning tunneling microscopy studies of c 60 monolayers on au (111). *Physical Review B, 80*(23), 235434.

[15] Altman, E. I., & Colton, R. J. (1992). Nucleation, growth, and structure of fullerene films on Au (111). *Surface science, 279*(1-2), 49-67.

[16] Kurikawa, T., Nagao, S., Miyajima, K., Nakajima, A., & Kaya, K. (1998). Formation of Cobalt−C_{60} Clusters: Tricapped $Co(C_{60})_3$ Unit. *The Journal of Physical Chemistry A, 102*(10), 1743-1747.

[17] Avramov, P., Naramoto, H., Sakai, S., Narumi, K., Lavrentiev, V., & Maeda, Y. (2007). Quantum Chemical Study of Atomic Structure Evolution of Co_x/C_{60} ($x \leq 2.8$) Composites. *The Journal of Physical Chemistry A, 111*(12), 2299-2306.

[18] Gardener, J. A., Briggs, G. A. D., & Castell, M. R. (2009). Scanning tunneling microscopy studies of c 60 monolayers on au (111). *Physical Review B*, *80*(23), 235434.
[19] Cummings, M., Gliga, S., Lukanov, B., Altman, E. I., Bode, M., & Barrera, E. V. (2011). Surface interactions of molecular C_{60} and impact on Ni (100) and Co (0001) film growth: A scanning tunneling microscopy study. *Surface science*, *605*(1-2), 72-80.
[20] Altman, E. I., & Colton, R. J. (1992). Nucleation, growth, and structure of fullerene films on Au (111). *Surface science*, *279*(1-2), 49-67.
[21] Nagao, S., Kurikawa, T., Miyajima, K., Nakajima, A., & Kaya, K. (1998). Formation and Structures of Transition Metal− C_{60} Clusters. *The Journal of Physical Chemistry A*, *102*(24), 4495-4500.

Chapter 5. The Role of Temperature on the Self-Assembly of Co-C_{60} Clusters

5.1 Introduction

In the discussion in Chapter 4, small or medium size cobalt clusters have a very weak adsorption capacity for C_{60} at room temperature. Only after annealing at 320 °C for 30 minutes, the C_{60} molecules will wrap around the cobalt clusters to form Cobalt-C_{60} clusters. The most critical part for this phenomenon is how the effect of annealing, or heating, acts on the sample. The surface diffusion of C_{60} molecules at high temperatures, desorption of gas molecules, enhanced thermal motion of C_{60} molecules, the structure evolution of cobalt clusters, and the formation of carbon-cobalt bonds are all possible effect leading to the formation of Cobalt-C_{60} clusters. In order to clarify the role of thermal treatment in this phenomenon, new experiments are designed. It includes to observe the effect of thermal treatment when applied alone to cobalt clusters by switching the order between annealing and C_{60} deposition; and perform multiple annealing by continuously increasing the annealing temperature in order to find the critical temperature for Cobalt-C_{60} cluster formation.

5.2 Experiment Procedure

In this experiment, the same method as in Chapter 4 is still used to prepare Au (111) substrates. The 300 nm thick gold film was grown on a freshly cleaved HOPG substrate by PVD method. The Au film on HOPG was then removed from the evaporator and transferred to the UHV system where a current of 1.5 A passed through the PBN heater and the voltage across the heater was measured as 21.8 V. Upon cooling to room temperature, the sample was sputtered with argon ions at 1.5 keV and 10μA. One annealing and one argon ion sputtering were performed as one round, and after thirteen rounds of sample clean-up, three additional anneals were performed, resulting in a flat, clean Au (111) flat substrate sample.

Cobalt was deposited on the Au (111) surface using a commercial PVD evaporator made by Createch. Deposition was carried out at 1300°C for eight minutes at I=7.15 A and V=10.9 V, depositing 0.2 ML of cobalt on the Au (111) surface. The samples were then annealed three times at 85°C, I=0.2 A, V=5.1 V; 204°C, I=0.4 A, V=8.7 V and 340°C, I=0.8 A, V=13.4 V, each lasting 30 minutes. Each time the sample is imaged by STM. 0.5 ML C_{60} molecules were then deposited on the Co/Au (111) sample using home-made Knudsen cells at 402°C for a total of 4 minutes at a current of 7.0 A. The sample was then annealed 5 times at 84°C, I=0.2 A, V=4.8 V; 198.4°C, I=0.4 A, V=8.2 V; 321°C, I=0.7 A, V=12.4 V; 348°C, I=0.8 A, V=13.2 V and 381°C, I=0.9 A, V=14.5 V, each lasting thirty minutes. Image the sample after each treatment.

5.3 Experimental Results

5.3.1 Temperature-dependent Structure Evolution of Cobalt Clusters

Fig. 5.1-Fig. 5.4 show STM images of the same Cobalt/Au (111) sample after different temperature annealing. Figure 5.1 (a) shows the unannealed Co/Au (111) sample. The obvious irregularities in the edges of the cobalt clusters from the image can be seen. From Figure 5.1 (b), it can be seen that the cobalt clusters show typical bilayer behaviors of the cobalt clusters deposited and grown on the Au (111) surface. These are consistent with what is documented in Section 4.3.1 and in the literatures [1][2].

In contrast, in Fig 5.2 (a), after annealing at 80°C for 30 minutes, it can be seen that the shape of the cobalt clusters becomes significantly more regular compared to Fig 5.1 (a). As can be seen in Fig 5.2 (b), the majority of the clusters remain in a 2-layer structure. However, in Figure 5.2 (b), clusters of cobalt at a height of 0.2 nm are also observed, indicating that monolayer cobalt clusters are also starting to appear at this stage.

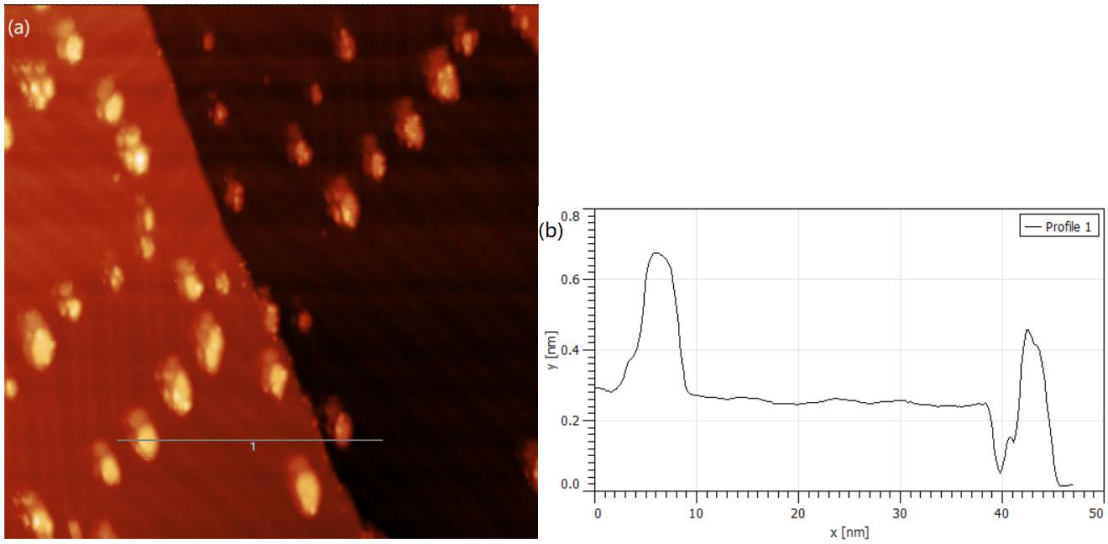

Fig. 5.1 (a) STM image of 0.2 ML cobalt atoms deposited on Au (111) substrate, unannealed. I=500 pA, V_{gap}=-2.0 V, 100 nm × 100 nm. (b) Height information for linear region 1. The x-axis represents distance and the y-axis represents height.

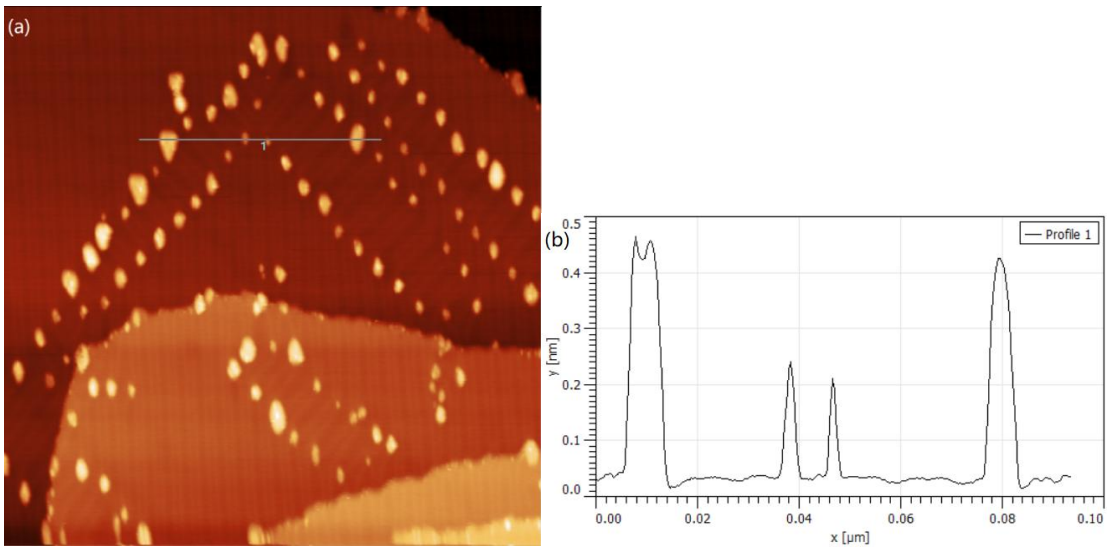

Fig. 5.2 (a) STM image of 0.2 ML cobalt atoms deposited on Au (111) substrate, annealed at 80°C for 30 min. I=500 pA, V_{gap}=-2.0 V, 100 nm × 100 nm. (b) Height information for linear region 1. The x-axis represents distance and the y-axis represents height.

In Fig. 5.3 (a), after annealing at 200 °C for 30 minutes, more small-size cobalt clusters appear compared to Fig. 5.2 (a). As can be seen in Fig. 5.3 (b), after annealing at 200 °C for 30 minutes, clusters with the height lower than 0.2 nm, which is lower

than monolayer cobalt atoms in height, have appeared. As described in Section 4.3.1, this height means that some cobalt clusters that are half submerged in the gold surface. At the same time, as can be seen in Fig. 5.3 (c), there are still many cobalt clusters that retain their bilayer structure.

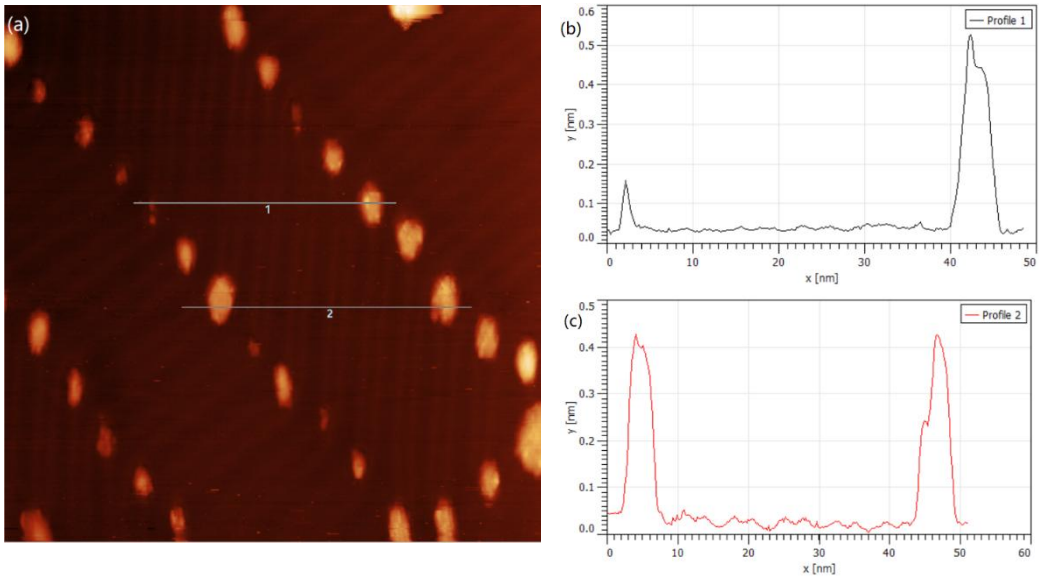

Fig 5.3 (a) STM image of 0.2 ML cobalt atoms deposited on Au (111) substrate, annealed at 200 °C for 30 min. I=500 pA, V_{gap}=-2.0 V, 100 nm × 100 nm. (b) Height information for linear region 1. (c) Height information for linear region 2. The x-axis represents distance and the y-axis represents height.

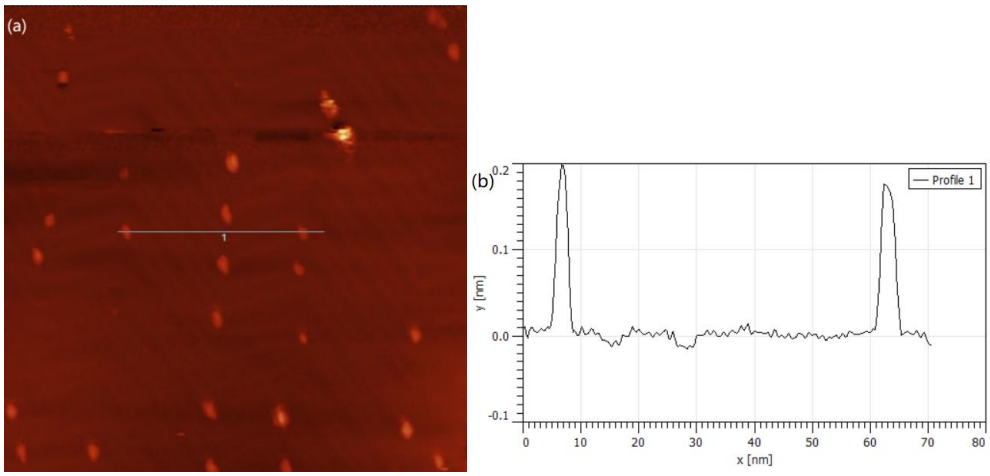

Fig. 5.4 (a) STM image of 0.2 ML cobalt atoms deposited on Au (111) substrate, annealed at 340 °C for 30 min. I=500 pA, V_{gap}=-2.0 V, 100 nm × 100 nm. (b) Height information for linear

region 1. The x-axis represents distance and the y-axis represents height.

After annealing at 340°C for 30 min, it can be seen in Fig. 5.4 that the vast majority of the cobalt clusters on the surface of the sample are small single layer clusters. Even only by visual inspection, it can observe that there is a significant decrease of cobalt coverage as the annealing temperature increases.

	Unannealed	80°C	200°C	340°C
Coverage/ML	0.210	0.139	0.080	0.040
Standard deviation of Coverage/ML	0.0127	0.0197	0.0228	0.0238
Co Cluster Average Height /nm	0.292	0.383	0.276	0.214
Standard deviation of Average Height /nm	0.0521	0.0456	0.0025	0.020

Table 5.1 Table about the variation of cobalt cluster coverage and average cobalt cluster height on the Au (111) surface with annealing temperature increasing.

Fig. 5.1-5.4 show representative areas of the sample surface at different annealing temperatures. In order to show more generally the effect of annealing on the whole sample, under every annealing temperature, five 100 × 100 nm regions were selected to calculate their surface coverage and the average height of the cobalt clusters, each with a mm scale distance difference between them. Within these regions, under each temperature, roughly 150 cobalt clusters are contained. The average height of cobalt clusters is counted instead of the number of monolayer and bilayer cobalt clusters because of the large number of irregular cobalt clusters. It is difficult to distinguish between monolayer and bilayer cobalt clusters. The average values of these five areas are used to represent the mean value of the whole sample. The evolution of the coverage and average height of cobalt clusters with increasing annealing temperature are shown in Table 5.1 and Fig. 5.5. Considering that the desorption of cobalt from the gold surface does not occur at an annealing temperature of 300°C based on many references [3][5][16], the decrease in surface cobalt coverage is explained by the fact that

the cobalt clusters sink into the gold surface at high temperatures, which is also consistent with the literature [5]. What's more, the rising and then falling of the average height of cobalt clusters deserves attention. After annealing at 80°C, the average height of the cobalt clusters rises closer to the 0.4 nm height, suggesting a transition from more monolayer to bilayer structure at lower annealing temperatures, which is also consistent with the more regular structure of the clusters in Fig. 5.1 to 5.2. At higher annealing temperatures, the average height of the cobalt clusters gradually decreases towards 0.2 nm, suggesting that the overall sinking of the cobalt clusters is the main change of the clusters at this stage.

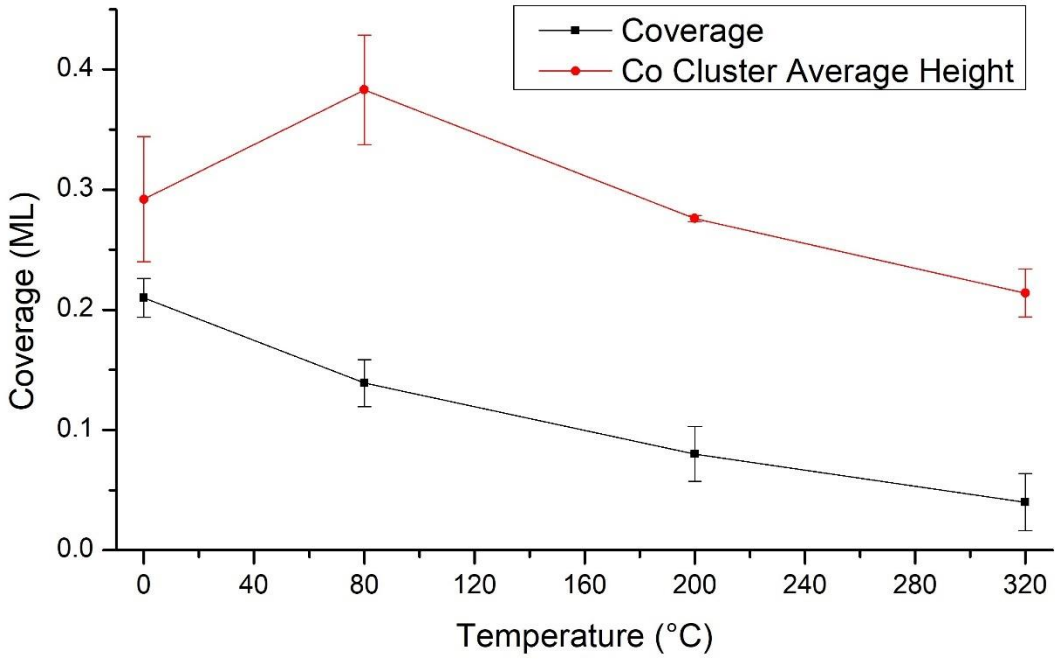

Fig. 5.5 Graphs about the evolution of cobalt cluster coverage on the Au (111) surface versus the average cobalt cluster height with increasing annealing temperature.

The changes in the cobalt clusters on Au (111) after annealing can be seen as two parts. On the one hand, annealing can cause the cobalt cluster reconstruction and become more regular, which is consistent with the property of the large cobalt film covering the gold substrate after annealing [3]. On the other hand, the coverage of

cobalt clusters gradually decreases with increasing annealing temperature, which can be explained by the sinking of cobalt clusters into the Au (111) surface at high temperatures [4][5].

5.3.2 The Aggregation of Post-deposition C_{60}

0.5 ML C_{60} molecules were deposited on the pre-annealed samples. As can be seen in Fig. 5.6 (a) and 5.7 (a), there is a clear difference between the pre-annealed sample and the sample deposited C_{60} firstly and then annealed (e.g. Fig. 4.9). The C_{60} molecules behaved closer to the unannealed Co-C_{60}/Au (111) sample, with most of the C_{60} molecules aggregating into large islands rather than surrounding the cobalt clusters. However, unlike the unannealed Co-C_{60}/Au (111) sample, the cobalt clusters on the Au (111) surface are mostly 0.2 nm high monolayer clusters after a 340°C, 30-minute pre-annealing, rather than the 0.4 nm high bilayer clusters in the unannealed sample.

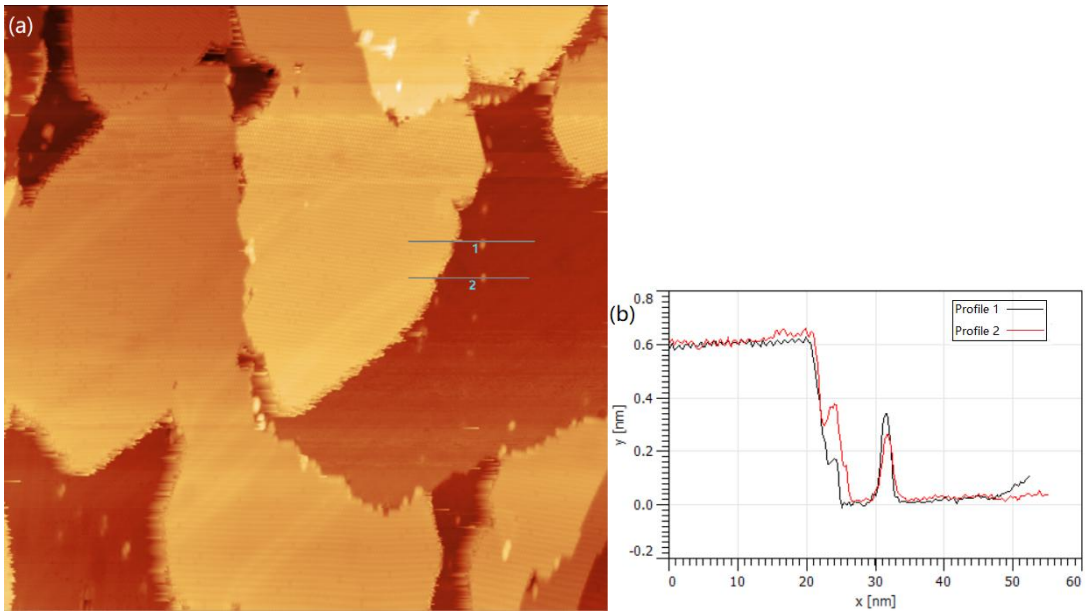

Fig. 5.6 (a) STM image of 0.5 ML C_{60} molecule on Co/Au(111) sample annealed at 340°C, unannealed. I=500 pA, V_{gap}=-2.0 V, 100 nm × 100 nm. A large number of C_{60} molecules are clustered into monolayer islands. (b) Height information for profile 1 is in black. Profile 2 is in red. The x-axis represents distance and the y-axis represents height.

As shown in Chapter 4. For the other exposed small-size cobalt clusters, in Fig. 5.7(a), unlike the unannealed sample, C_{60} molecules adsorbed onto the small size cobalt clusters are exist, but the number of adsorbed C_{60} is very low. In Fig. 5.7 (b), the 0.6 nm peak in profile 1 points to this being an adsorbed C_{60} molecule, but these bright dots in Fig.5.7 (a) or peaks in Fig.5.7 (b) is rare.

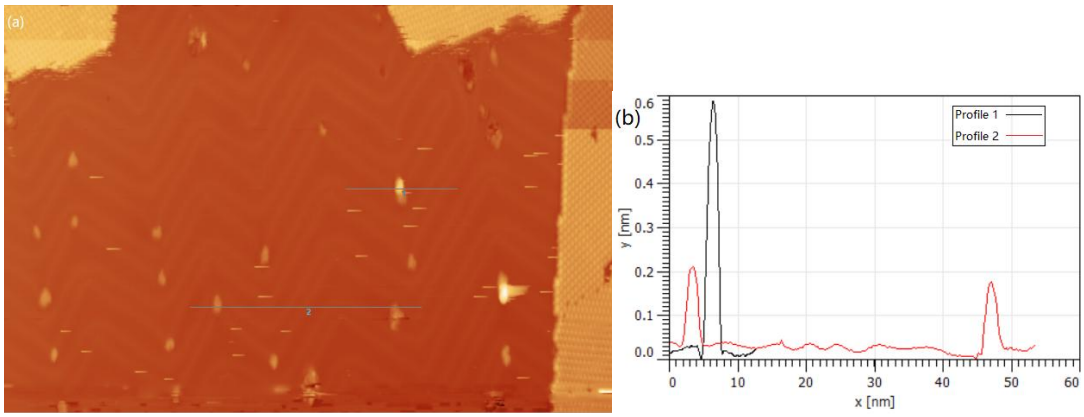

Fig. 5.7 (a) STM image of 0.5 ML C_{60} molecules on Co/Au (111) sample has been annealed at 340 °C, not annealed. I=500 pA, V_{gap}=-2.0 V, 100 nm × 100 nm. The vast majority of the cobalt clusters are bare, but clusters of adsorbed C_{60} are also present. (b) Height information for profile 1 is in black. Profile 2 is in red. The x-axis represents distance and the y-axis represents height.

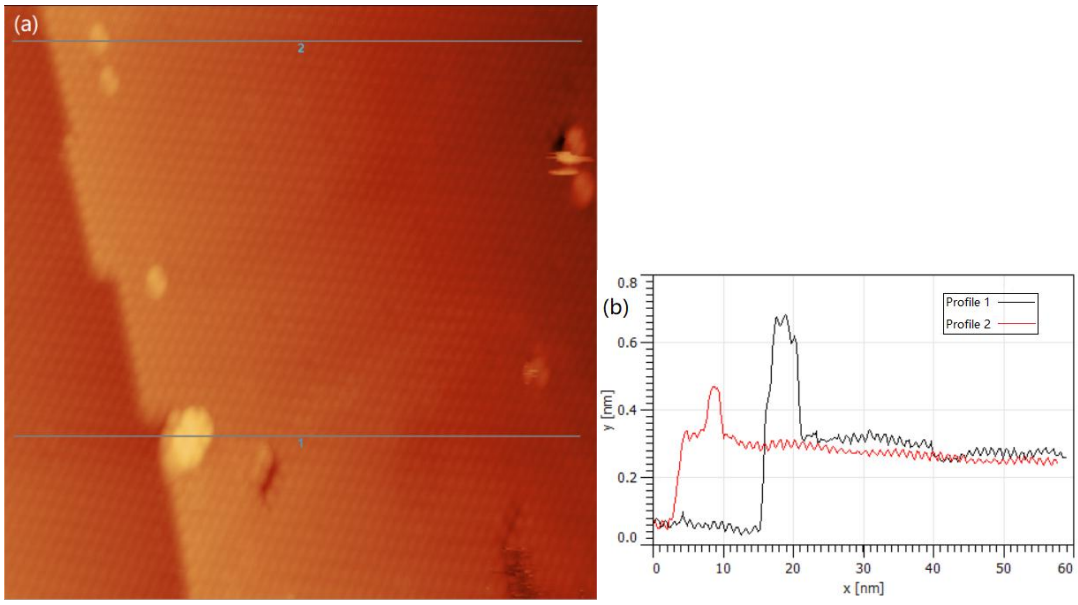

Fig. 5.8 (a) STM image of 0.5 ML C_{60} molecule on Co/Au (111) sample has been annealed at

340 °C, not annealed. I=500 pA, V_{gap}=-2.0 V, 100 nm × 100 nm. Small cobalt cluster completely covered by C_{60}. (b) Height information for profile 1 is in black. Profile 2 is in red. The x-axis represents distance and the y-axis represents height.

At the same time, as can be seen in Fig. 5.8, C_{60} is close-packed and no defects are present. Whereas the seven brighter molecules in Fig. 5.8 (a) show a height difference of 0.2 nm from the others in Fig. 5.8 (b). This points out that the annealed cobalt clusters can be completely covered by C_{60} molecules instead of forming defects. These phenomena suggest that pre-annealing does reduce small-size cobalt clusters' low adsorption rate of C_{60}, but the edge of C_{60} island instead of small cobalt cluster is still the first adsorbed site for the C_{60} molecules. For the phenomenon that small cobalt clusters can be fully covered by C_{60} after annealing, this can be explained by the fact that the semi-sunken cobalt clusters provide suitable sites for interactions between C_{60} molecules. This will be discussed in detail in section 5.4.1.

5.3.3 Adsorption of C_{60} on Cobalt after Re-annealing

As described in the previous sections, the arrangement of C_{60} on Au (111) changed significantly after exchanging the order of annealing and deposition of C_{60} molecules. For further investigating the effect of temperature on the Co-C_{60} interaction, the sample was subjected to further annealing. Fig. 5.9 (a)-(d) correspond to the STM images of the C_{60} depositing Co-Au (111) sample pre-annealed after annealing at 30 minutes, 80°C, 200°C, 320°C and 340°C respectively. Most intuitively, re-annealing did not make any significant difference to the samples. Whether annealed at 80°C, 200°C, 320°C or 340°C, the cobalt clusters remain overwhelmingly bare and the C_{60} islands remain clustered into large islands. The relationship between the cobalt clusters and C_{60} is not significantly changed from the Co-C_{60}/Au (111) sample without secondary annealing as represented in Fig. 5.6 (a). It is particularly noteworthy that in Chapter 4, the C_{60} islands disappeared after annealing at 320 °C whereas on this sample, the C_{60} islands were still present after annealing at 340 °C. This is because

annealing below 400°C is not sufficient to desorb C_{60} from Au (111). [17] The disappearance of the C_{60} islands in Chapter 4 is actually the result of the C_{60} molecules being partly adsorbed by a large number of cobalt clusters, rather than leaving the surface. The reduction in cobalt cluster adsorption sites after annealing on this sample resulted in the continued aggregation of C_{60} molecules.

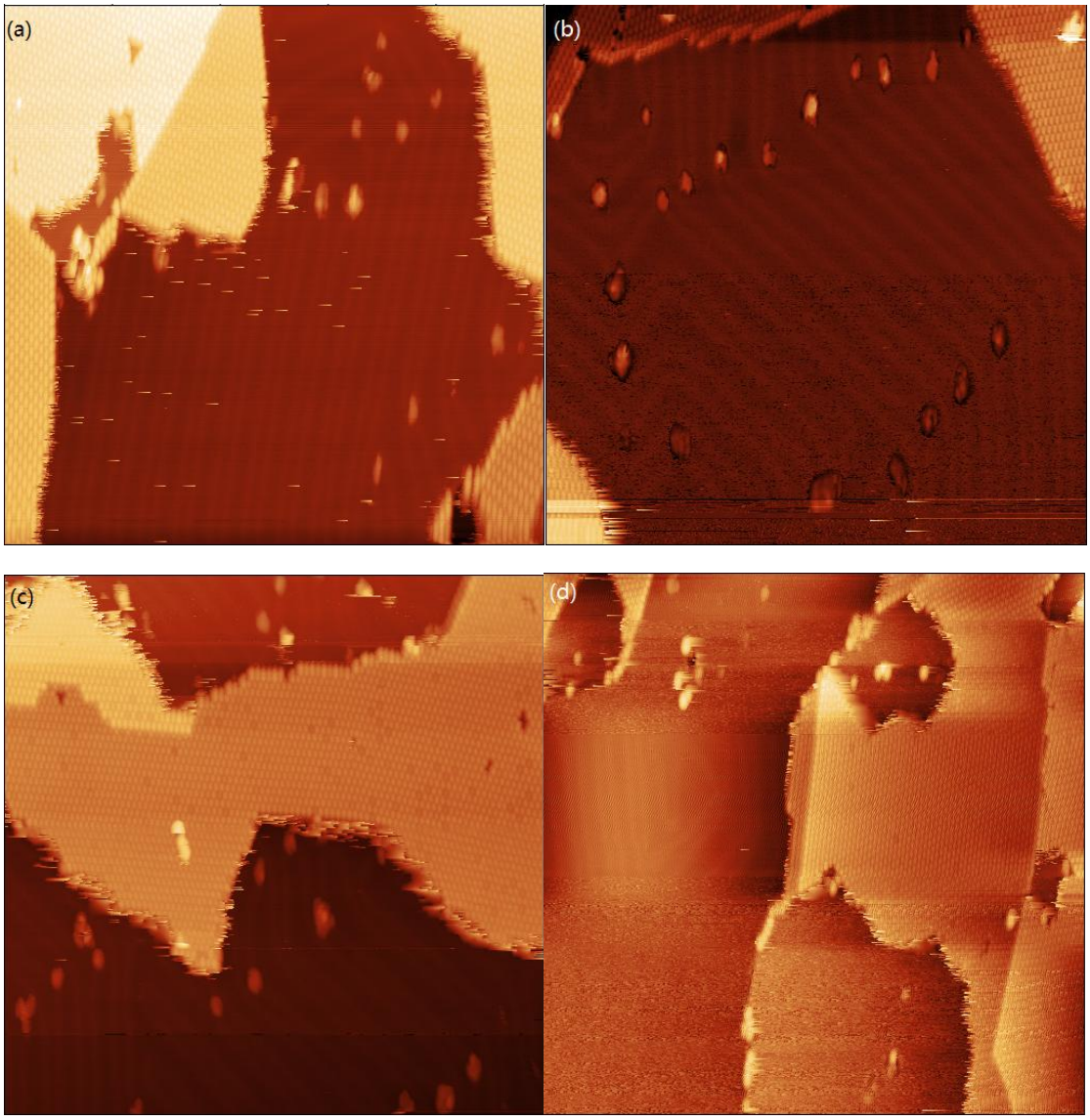

Fig. 5.9 (a) STM image of Co-C_{60}/Au (111) sample re-annealed at 80°C for 30 min. I=500 pA, V_{gap}=-2.0 V, 100 nm × 100 nm. (b) STM image of sample annealed at 200°C for 30 min. I=500 pA, V_{gap}=-2.0 V, 100 nm × 100 nm. (c) STM image of 0.5 ML C_{60} molecules on Co/Au (111) sample annealed at 320°C for 30 min. I=500 pA, V_{gap}=-2.0 V, 100 nm × 100 nm. (d) STM image of 0.5 ML C_{60} molecules on Co/Au (111) sample annealed at 340°C for 30 min. I=500 pA, V_{gap}=-2.0 V.

100 nm × 100 nm.

However, if the average number of C_{60} molecules adsorbed by the cobalt clusters on the samples is counted, it can be seen that the average number of C_{60} molecules adsorbed by the cobalt clusters changes with the annealing temperature increasing as shown in Table 5.2 and Fig. 5.10. By the average number of C_{60} molecules adsorbed by the cobalt clusters from six 100 × 100nm regions and above 200 clusters, it can be seen that on the one hand, as mentioned above, the average number of adsorbed C_{60} molecules is never greater than 1. So, it can be said that the expected cobalt-C_{60} clusters never appear. On the other hand, the rate of C_{60} adsorption did increase as the annealing temperature slowly. And there is a relatively large improvement after 320°.

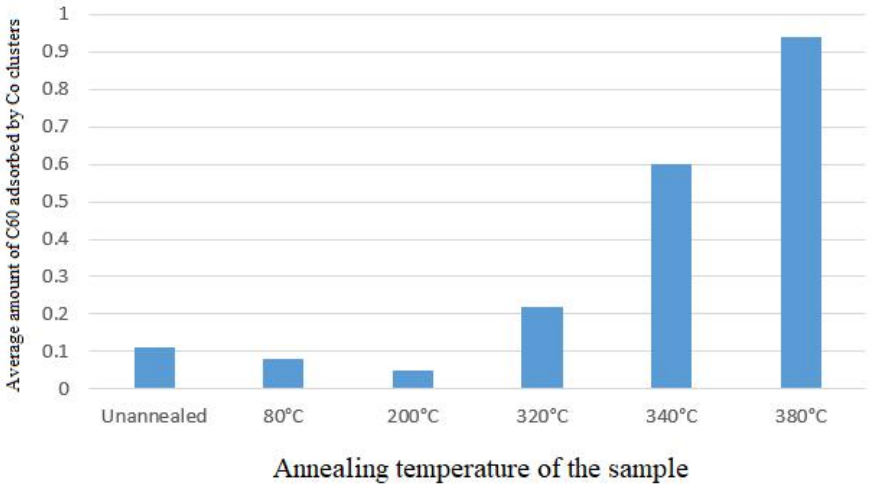

Fig. 5.10 Bar chart about the evolution of the average amount of C_{60} adsorbed by cobalt clusters with increasing annealing temperature.

	Unannealed	80°C	200°C	320°C	340°C	380°C
Adsorbed C_{60} per Co Cluster	0.11	0.08	0.05	0.22	0.6	0.94

Table 5.2 Table of the variation of the average amount of C_{60} adsorbed by cobalt clusters with increasing annealing temperature.

5.3.4 Diffusion of Cobalt Clusters and the Collapse of C_{60} Island Edges

If continue to anneal the sample at an annealing temperature of 380 °C, further changes in the surface structure of the sample are observed in addition to the further increase in

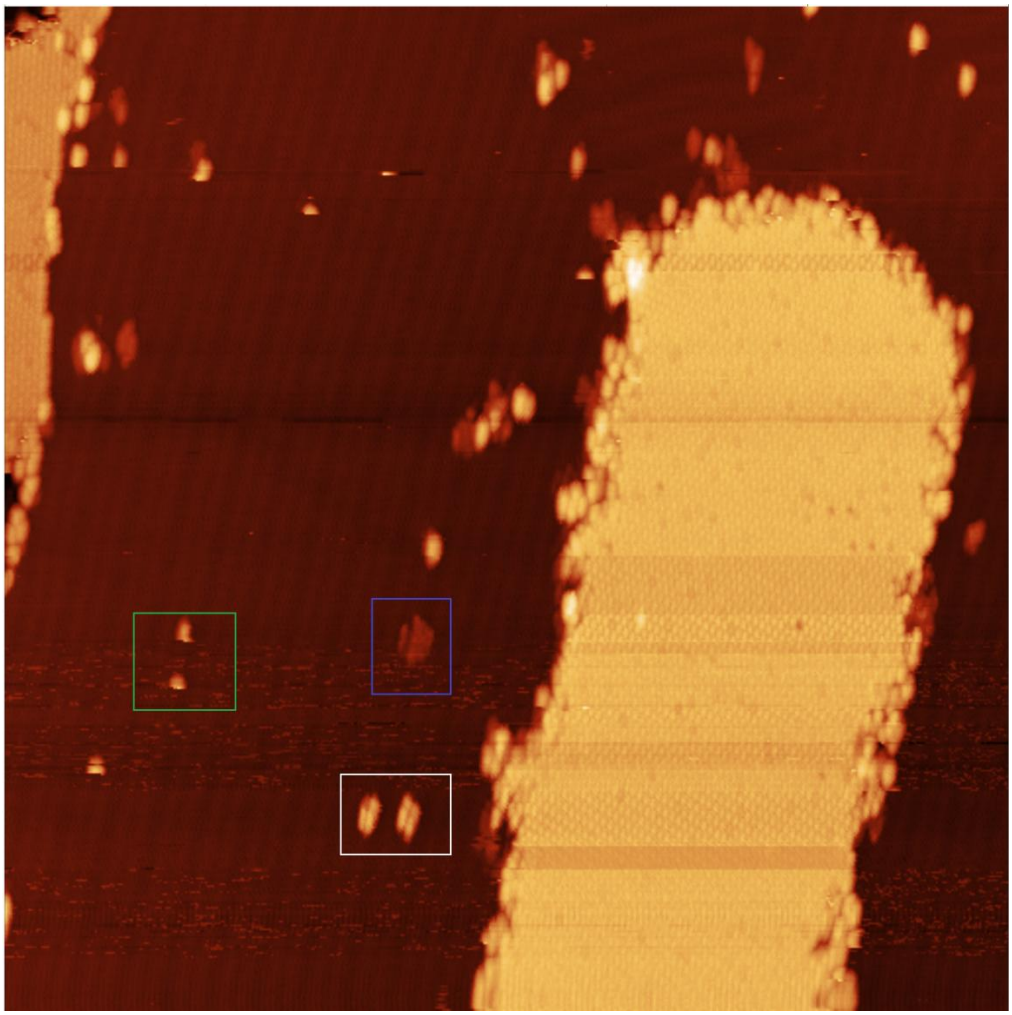

Figure 5.11 STM image of 0.5 ML C_{60} molecules on Co/Au (111) sample annealed at 340 °C, secondary annealed at 380°C for 30 min. I=500 pA, V=-2.0 V, 100 nm × 100 nm.

the average number of adsorbed C_{60} molecules demonstrated in Fig. 5.10. As shown in Fig. 5.11, the most significant change is that the boundaries of the C_{60} islands collapse. The edges of the C_{60} islands are no longer close-packed arrangement of C_{60} molecules, but more resemble a disordered stacking of C_{60} molecules. Furthermore, the C_{60} molecules are also heavily adsorbed by cobalt clusters at the edges of the C_{60}

islands. At the same time, both the cobalt clusters and the C_{60} molecules are observed at the location out of the elbow sites on the 380 °C annealed sample. In the green frame region of Fig. 5.11, the C_{60} molecules are on parallel reconstructed DLs, whereas in the STM images both C_{60} molecules are incomplete. It indicated that these C_{60} molecules are dragged across the Au (111) surface by the STM probe in scanning. In the blue frame region, a cobalt cluster can be seen, also on the parallel DLs, which is an unusual located position not seen on any other samples. In the white frame region, there is also two stable C_{60} clusters on the surface adsorbed by the cobalt cluster on the parallel DLs.

At the same time, it needs to be discussed that, due to the widespread presence of C_{60} molecules diffusing on the Au (111) surface [7], C_{60} molecules that deviate from their original position are easily understood. Even if the plausibility that those structures that deviate from their original position are C_{60} molecules is high when considered from an image perspective only. In the case of cobalt atoms, the diffusion of cobalt atoms on the Au (111) surface is extremely rare at room temperature, which could also be interpreted to mean that these structures may not be simply identified as cobalt. Furthermore, considering that the samples have undergone multiple annealing, and that structure evolution of C_{60} molecules in the presence of cobalt does occur [8][9], there are more possibilities for the composition of these structures. These possibilities will be discussed in more detail in the next section.

5.4 Analysis and Discussion

5.4.1 Compounding Effect of Annealing on Cobalt-C_{60} Clusters

A comparison of what is discussed in Section 5.3.2, Section 5.3.3 with Section 4.3.3 shows that for the Co/Au (111) sample, depositing the C_{60} molecules firstly and annealing afterwards produces completely different results with depositing the C_{60} molecules after annealing firstly. The difference in results caused by the swapping of

annealing and deposition order illustrates that annealing of the cobalt clusters alone is not enough to raise their adsorption capacity for C_{60} to the desired level. And furthermore, even when the pre-annealed sample is annealed again at 320°C for 30 min, no expected Co-C_{60} clusters are produced on the surface. This result suggests that although annealing at 320°C to both C_{60} and Co is an important condition for the formation of Cobalt-C_{60} clusters, annealing for Co alone has a negative effect on cluster forming.

At the same time, as shown in Section 5.3.2 based on experimental data, although the cobalt clusters are still not the first-choice sites for C_{60} molecules on the pre-annealed cobalt/Au (111), the defects of the unannealed small cobalt clusters on C_{60} islands disappears. Many small cobalt clusters completely covered by C_{60} monolayers can be observed on the samples. This indicates that after pre-annealing, the adsorption capacity for C_{60} island edges close to cobalt clusters is enhanced. the changes in the adsorption capacity of the various adsorption sites for C_{60} after pre-annealing are shown in Table 5.3.

Adsorption sites	C_{60} adsorption capacity after pre-annealing	Gas Pollution model	Potential Barrier model	Inefficient Contact model
C_{60} island edges close to Co clusters	↑	√	×	√
Bare Co Cluster	—	×	√	√
Co clusters in annealing	↓	×	√	√

Table 5.3 Table about changes in the adsorption capacity for C_{60} at different sites after pre-annealing and the suitability to different models.

In Chapter 4, three models for the low adsorption rate of C_{60} by small cobalt clusters on Au (111) surface are presented: the Potential Barrier model where the cobalt clusters are embedded in the gold surface causing a potential barrier; the Inefficient

Contact model where irregular surface of the cobalt cluster results in a very low contact efficiency with the C_{60} and the Gas Pollution model where the cobalt clusters adsorb gas molecules cause surface passivation. In these three models, the gas pollution model is the worst fit with the experimental results. In the above experiments, the interval between the pre-annealing of the sample and the deposition of C_{60} is only 1h. At a vacuum of 10^{-9} mbar, such a short time is not enough for the cobalt clusters to adsorb enough gas molecules. It may be possible that the structural changes to the cobalt clusters as a result of annealing may improve the gas adsorption capacity of the clusters. However, unlike the situation in the atmosphere, in UHV environment where gas molecules are extremely rare, the factor that directly affects the adsorption efficiency of gas molecules is the number of gas molecules that fall on the sample. It is unlikely that the gas adsorption efficiency can be increased significantly under ultra-high vacuum and shorter placement times, no matter how much the shape of the cobalt clusters is improved. Therefore, under the gas adsorption model, the adsorption capacity of the pre-annealed cobalt clusters for C_{60} should be increased in this case. This is contrary to the lack of change in bare cobalt clusters' adsorption capacity and contrary to the decrease in the adsorption capacity of the cobalt clusters during annealing, which is shown in Table 5.3.

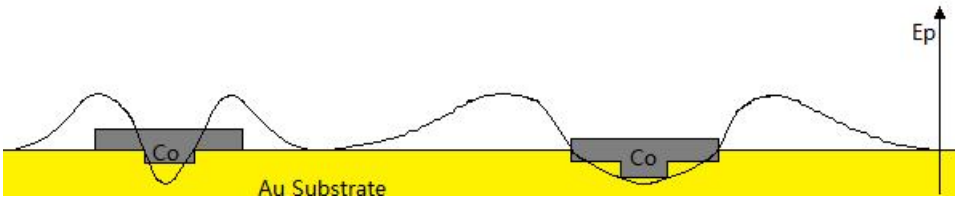

Fig. 5.12 Diagram of why the potential barrier model is incorrect. If the assumption is made that the nucleation of cobalt atoms embedded in the gold surface will change the surface disposition of the gold atoms and form a potential barrier that is not crossed by C_{60} molecules at RT, then the cobalt clusters that sink into the gold surface after annealing will form a more extensive potential barrier.

The case of the potential barrier model is similar to that of the gas pollution model. If

the reconstruction potential barrier due to the embedding of the cobalt atoms on the gold surface is the reason for the low adsorption rate of C_{60} molecules by cobalt clusters on the unannealed sample, a more complete embedding of the cobalt clusters on the gold surface after pre-annealing should increase this potential barrier, as shown in Fig. 5.12. Therefore, the low adsorption rate of C_{60} molecules by the cobalt clusters at the edges of the C_{60} islands should be greater in this case, which is contrary to the experimental results.

The Inefficient Contact model, on the other hand, is the model that best matches the experimental results. As described in Section 5.3.1, by annealing the cobalt clusters, the clusters firstly transform into a more stable bilayer structure as the temperature increases, followed by another transformation from a bilayer to a monolayer structure. The complex effect of cobalt clusters' surface flatting and overall sinking is consistent with the complex effect of C_{60} adsorption on different sites. The number of cobalt atoms of the pre-annealed clusters above surface is limited due to the cluster sinking, whether at RT or high temperatures. It determines that the clusters, no matter how they refine themselves, are unable to achieve sufficient contact efficiency after annealing. This results in a reduction of the C_{60} adsorption capacity of the pre-annealed cobalt clusters. The situation is different for C_{60} islands edges close to the cobalt clusters. Although the monolayer clusters do not have sufficient adsorption capacity, the flatter surface of the pre-annealed clusters results in better contact with the C_{60} islands and higher adsorption capacity for C_{60} molecules fallen on them. This is reflected in the increased adsorption capacity of C_{60} island edges close to the cobalt clusters. This increase in adsorption capacity is simply illustrated in Fig. 5.13.

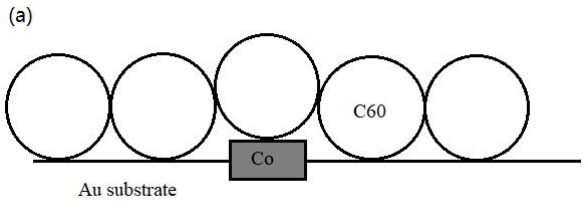

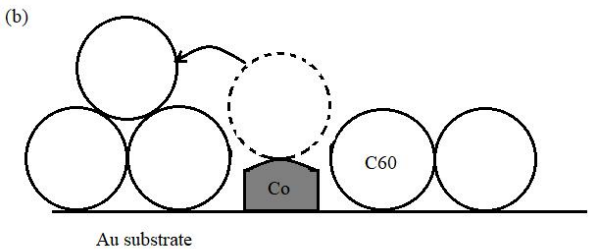

Fig. 5.13 Diagram of the difference in adsorption capacity of different cobalt clusters for C_{60} molecules at the edge of C_{60} islands. (a) The C_{60} covering the pre-annealed cobalt clusters is polymerized by C_{60}-C_{60} interactions. (b) The C_{60} molecules on the unannealed cobalt clusters are unable to make contact with the C_{60} islands. Therefore, migrating due to insufficient interactions.

It is therefore clear from the above analysis that in the three models for the low adsorption rate of C_{60} by cobalt clusters, only the Inefficient Contact model for cobalt clusters can explain all of the experimental phenomena. The other two models all have unexplained experimental phenomena. Therefore, although it cannot be said that the gas adsorption of cobalt clusters or the reconstruction potential barriers around cobalt clusters are completely absent, it should be considered that these two mechanisms do not play a dominant role in the Cobalt-C_{60} cluster formation.

5.4.2 Formation of Cobalt-Carbon Bonds at High Temperatures

As can be seen in Fig. 5.10, the adsorption capacity of the cobalt cluster to C_{60} increases gradually with annealing temperature. However, for the Inefficient Contact model, the increase in adsorption capacity at high temperatures is achieved by the thermal motion and self-refinement of the cobalt atoms. In this model, then, the temperature dependence of the adsorption capacity should not be linear but jumpy. Therefore, there should be another mechanism by which the adsorption capacity of the cobalt cluster to C_{60} increases with temperature. In general, two explanations can be found for this phenomenon: 1) Due to the higher diffusion rate of C_{60} molecules at high temperatures, there is a greater probability of C_{60} molecules to meet the cobalt clusters and be adsorbed. 2) At high temperatures, the reaction rate for the formation of cobalt-carbon bonds between cobalt and C_{60} molecules increases with temperature,

resulting in more C_{60} bonded by cobalt-carbon bonds.

However, since the C_{60} molecules have a high diffusivity on the gold surface at room temperature[12], it can be assumed that the contact between the cobalt clusters and the C_{60} molecules would have been quite sufficient, even if not at such a high temperature of 320°C. Especially considering that the annealing in the experiment lasted for half an hour, the increase in diffusion efficiency of the C_{60} molecules with temperature should play a rather limited role in the C_{60} adsorption effect of the cobalt clusters in this case. It should therefore assume that the formation of cobalt-carbon bonds at high temperatures is a reasonable speculation. For samples without thermal treatment, at a certain temperature, the cobalt clusters will firstly adsorb C_{60} molecules via van der Waals forces and then open the C_{60} cage at high temperature to form a cobalt-carbon bond. For the pre-annealed samples, the cobalt clusters do not have enough adsorption capacity, so at high temperatures, C_{60} should diffuse on the gold surface and not stay on the cobalt clusters. This determines an extremely short time window for the chemical reaction between cobalt and C_{60} to occur. The production rate of the Cobalt-C_{60} polymer will therefore be directly linked to the reaction rate. In the experimental results, this is also reflected in the gradually increasing of the average number of adsorbed C_{60} molecules with increasing temperature.

5.4.3 Segment Formation of Cobalt-C_{60} Clusters

In the two sections above, two adsorption forms of cobalt clusters onto C_{60} molecules are discussed: van der Waals force adsorption of C_{60} molecules by bilayer cobalt clusters that do not contain chemical reactions and cobalt-carbon bonding at high temperatures. Combining these two modalities then shows the process of Cobalt-C_{60} cluster formation in Chapter 4.

For the untreated cobalt clusters on the gold surface, they are not ideal adsorption sites for C_{60} molecules. So, when C_{60} molecules are deposited onto the sample surface,

they aggregate into large islands of C_{60} rather than being adsorbed by the cobalt clusters.

When the sample is heated, if the annealing temperature reaches a certain temperature, the C_{60} adsorption capacity of the cobalt clusters is enhanced. At this stage, the cobalt clusters do not extensively sink into the gold surface and become better C_{60} adsorption sites than before. So, a large number of C_{60} molecules with a high diffusion rate on the gold surface are rapidly adsorbed by clusters and the cobalt clusters are completely wrapped up. These C_{60} molecules surrounding the cobalt clusters will protect the clusters from further sinking, thus retaining them to higher temperatures. Then, when the temperature continues to rise, cobalt-carbon bonds between the cobalt and C_{60} molecules will form.

5.4.4 Interpretation of Co Cluster Diffusion and C_{60} Island Edge Collapse

In Fig. 5.11, the collapse of the C_{60} islands is a very unique phenomenon. Most obviously, if all the C_{60} molecules fall on the Au (111) surface, this disordered arrangement of C_{60} molecules cannot exist in a stable state. There must be some additional interaction holding the C_{60} molecules in place. It is easy to think that the most likely identity of this should be the interaction between the cobalt and C_{60} molecules. According to the explanation provided above, at sufficient annealing temperature, the C_{60} cage would open to form a cobalt-C bond thereby holding the C_{60} molecule in place. At 380°C, the rate of Co-C bond formation increases and all C_{60} molecules just diffusing out from the C_{60} island edges will be captured by the cobalt cluster, forming an irregular C_{60} boundary thereby preventing the molecules inside from continuing to diffuse out. This results in a phenomenon similar to the collapse of the C_{60} island edge in Fig. 5.11.

Another question is why the cobalt clusters appear outside the elbow sites in Fig. 5.11. Because of lacking sufficient experimental data to support this phenomenon, I can only offer a few guesses at present. The first possibility is that it is not a cobalt cluster,

but some kind of structure transformed from a C_{60} molecule that has opened cage in the presence of cobalt and high temperature. This is an unusual explanation, which lacks unusual evidence to support it, so I do not want to adopt this hypothesis at this stage. The second explanation is that at high temperature, most of the cobalt clusters that had already embed into the gold surface which would diffuse inside the gold interface at 380 °C and thus left the elbow site. The cobalt clusters are located at the elbow sites of the Au (111) surface because the elbow site is the lowest energy point on the surface [13]. When most of the cobalt clusters are below the Au interface, surface energy is clearly not the only reason for the choice of cobalt cluster location. A third explanation is that the cobalt cluster did not actually move relative to the whole gold crystal, but the embed cobalt clusters changed the stress distribution on the gold surface thereby changing the surface reconstruction DLs, as reported in some other experiments [14][15]. In other words, it is not the cobalt clusters that leave the elbow sites but the elbow sites that leave the cobalt clusters. Both the second and third explanations seem possible, but again, neither can be directly proven on the basis of the available evidence, so these doubts can only be reserved for discussion in the next section.

5.5 Summary

In this chapter. the role that annealing plays in the manufacturing of cobalt-C_{60} clusters has been investigated by series experiments. These include swapping annealing with C_{60} deposition to order, as well as multiple annealing of pure Co/Au (111) samples and Co-C_{60}/Au (111) at gradually rising temperatures. Through these experiments, a clearer understanding of the multiple effects of temperature on the samples has been given, and have developed a model for the segmental formation of Cobalt-C_{60} clusters where C_{60} molecules wrap around the cobalt clusters at low temperature heating to prevent them from sinking, and form Cobalt-Carbon bonds at higher temperatures. And some possible explanations are given for the phenomenon of cobalt clusters leaving the elbow sites observed at high temperatures.

References

[1] Renard, D., & Nihoul, G. (1987). Crystal structure of a magnetic cobalt layer deposited on a (111) gold surface determined by transmission electron microscopy. *Philosophical Magazine B, 55*(1), 75-86.

[2] Chado, I., Padovani, S., Scheurer, F., & Bucher, J. P. (2001). Controlled nucleation of Co clusters on Au (111): towards spin engineering (vol 164, pg 42, 2000). *Applied Surface Science*, *172*(1-2), 190-190.

[3] Haag, N., Laux, M., Stöckl, J., Kollamana, J., Seidel, J., Großmann, N., ... & Aeschlimann, M. (2016). Epitaxial growth of thermally stable cobalt films on Au (111). *New Journal of Physics, 18*(10), 103054.

[4] Trant, A. G., Jones, T. E., Gustafson, J., Noakes, T. C. Q., Bailey, P., & Baddeley, C. J. (2009). Alloy formation in the Au {1 1 1}/Ni system–An investigation with scanning tunnelling microscopy and medium energy ion scattering. *Surface science, 603*(3), 571-579.

[5] Padovani, S., Scheurer, F., & Bucher, J. P. (1999). Burrowing self-organized cobalt clusters into a gold substrate. *EPL (Europhysics Letters), 45*(3), 327.

[6] Gardener, J. A., Briggs, G. A. D., & Castell, M. R. (2009). Scanning tunneling microscopy studies of c 60 monolayers on au (111). *Physical Review B, 80*(23), 235434.

[7] Guo, S., Fogarty, D. P., Nagel, P. M., & Kandel, S. A. (2004). Thermal diffusion of C_{60} molecules and clusters on Au (111). *The Journal of Physical Chemistry B, 108*(37), 14074-14081.

[8] Chen, Z. Y., Zhao, J. P., Yano, T., & Sakakibara, J. (2000). Growth mechanism of diamond by laser ablation of graphite in oxygen atmosphere. *Physical Review B, 62*(11), 7581.

[9] Ager III, J. W., & Drory, M. D. (1993). Quantitative measurement of residual biaxial stress by Raman spectroscopy in diamond grown on a Ti alloy by chemical vapor deposition. *Physical Review B, 48*(4), 2601.

[10] Meyer, J. A., Baikie, I. D., Kopatzki, E., & Behm, R. J. (1996). Preferential island nucleation at the elbows of the Au (111) herringbone reconstruction through place exchange. *Surface science, 365*(1), L647-L651.

[11] Xie, Y. C., Tang, L., & Guo, Q. (2013). Cooperative assembly of magic number C 60-Au complexes. *Physical Review Letters, 111*(18), 186101.

[12] Altman, E. I., & Colton, R. J. (1992). Nucleation, growth, and structure of fullerene films on Au (111). *Surface science, 279*(1-2), 49-67.

[13] Meyer, J. A., Baikie, I. D., Kopatzki, E., & Behm, R. J. (1996). Preferential island nucleation at the elbows of the Au (111) herringbone reconstruction through place exchange. *Surface science, 365*(1), L647-L651.

[14] Schaff, O., Schmid, A. K., Bartelt, N. C., de la Figuera, J., & Hwang, R. Q. (2001). In-situ STM studies of strain-stabilized thin-film dislocation networks under applied stress. *Materials Science and Engineering: A*, 319, 914-918.

[15] Hasegawa, Y., & Avouris, P. (1992). Manipulation of the reconstruction of the Au (111) surface with the STM. *Science, 258*(5089), 1763-1765.

[16] To, C., Zeppenfeld, P., Krzyzowski, M. A., David, R., & Comsa, G. (1997). Growth and stability of cobalt nanostructures on gold (111). *Surface science*, *394*(1-3), 170-184.

[17] Altman, E. I., & Colton, R. J. (1992). Nucleation, growth, and structure of fullerene films on Au (111). *Surface science*, *279*(1-2), 49-67.

Chapter 6. Experiment Design and Theoretical Prediction

6.1 Introduction

In Chapters 4 and 5, the mechanisms for the formation of the Cobalt-C_{60} cluster are discussed. However, due to the limited experimental conditions, these arguments are all based on STM images and height information but are not supported by experimental data from other experimental techniques. Judgements based on STM images and logical analysis alone is clearly not sufficiently robust, in questions such as the real composition of the "C_{60}" and "cobalt" clusters, the internal structure of the Cobalt-C_{60} interface, the way in which cobalt-C_{60} bonds, and the mixture of the cobalt clusters with the gold substrate. If objective conditions are ignored, experimental techniques such as ultra-low temperature scanning of STM, X-ray Photoelectron Spectroscopy (XPS) [1], Raman Spectroscopy [2] or Low Energy Electron Diffraction (LEED) [3] are all needed. Unfortunately, due to the limited experimental conditions, only VT-STM images can be relied upon in this experiment.

Therefore, in this chapter some of the unresolved parts will be listed of what has been discussed in the previous two chapters. Further, experiments will be designed to verify them and to make predictions about the possible results of these problems. It is worth noting that these experimental designs will all be based on the limited experimental techniques mentioned and used in this experiment. In other words, all of the designed experiments could be done independently by author and become a part of this thesis, if have infinite experiment time.

6.2 Analysis of Corollaries Requiring Proof

In Chapter 4 the phenomenon is reported that when C_{60} molecules are deposited onto a cobalt/Au (111) sample, the C_{60} molecules tend to arrange more into large C_{60} islands rather than be adsorbed by cobalt clusters. In contrast, after annealing at

320°C for 30 min, the large cobalt islands disappear and Cobalt-C_{60} clusters form on the surface. In Chapter 5, based on the analysis of experiments, the explanation for the formation of Cobalt-C_{60} clusters is given: (1) The cobalt clusters on the Au (111) surface are irregular and rugged due to lattice mismatch. This irregularity leads to the fact that the contact efficiency of C_{60} on cobalt clusters is low. Therefore, the cobalt clusters do not have sufficient interactions to adsorb C_{60} molecules at room temperature. (2) At a certain annealing temperature, the cobalt atoms enhance the thermal motion and self-refinement to adsorb C_{60} molecules, resulting in the formation of cobalt clusters wrapped by C_{60} molecules. (3) Cobalt clusters on Au (111) substrates will sink into the gold surface at high temperatures. However, the C_{60} molecules wrapped around the cobalt clusters can play a protective role to prevent the cobalt clusters from sinking. (4) At higher temperature, the C_{60} molecular cage will open and form a Co-C bond to make the adsorption of Cobalt-C_{60} clusters more stable.

How this explanation is derived from the experimental images is introduced at Chapter 5 in detail. However, there are still some questions left to be resolve: (1) If the sinking of the cobalt clusters is not considered, can the adsorption capacity improvement of the clusters by high temperatures be preserved after annealing? (2) Whether there is protection of the cobalt cluster by the C_{60} molecule from heat sinking. To what extent does this protection work? (3) Is the cobalt-carbon bond formed in C_r adsorption? Whether there are two individual stages of adsorption, both the adsorption of C_{60} molecules and the bonding of C_{60} molecules after cage opening.

In addition to this, in Section 5.3.4, the cobalt clusters left the elbow sites have been observed in experiments which is a very unusual phenomenon. This phenomenon is also worthy for further discussion.

6.3 Experimental Designs

6.3.1 The Principle of Cobalt Cluster Adsorption on C_{60} Molecules

In Chapter 5, it's found that the monolayer cobalt clusters pre-annealed at 340°C can be fully wrapped by C_{60}, but are still not the first site of C_{60} adsorption. This is explained as a combined result of the self-refinement and the sinking of the cobalt clusters into the gold surface after annealing. As shown in Section 5.3.1, the threshold temperature for the flattening of the cobalt clusters is lower than the sinking temperature. This implies the possibility that by annealing at a lower temperature, cobalt clusters with a flattened surface which have not completely sunk into the gold surface can be obtained. A key question then is whether the sample can adsorb C_{60} to form Cobalt-C_{60} clusters at room temperature. Another way of expressing this question is that for the experimental procedure of manufacturing Cobalt-C_{60} clusters by annealing at 320°C, whether the high thermal motion at high temperatures or the self-refined cobalt clusters after annealing become excellent adsorption sites for C_{60}.

For a static explanation, the increasing in adsorption capacity of C_{60} molecules should remain after the sample cooling down to room temperature. So, it is feasible to prepare Cobalt-C_{60} clusters at room temperature by pre-annealing at an appropriate temperature. For a dynamic explanation, this increasing in adsorption capacity can only exist at a certain temperature. When the sample is cooling down to room temperature, the thermal motion rate of the cobalt atoms is greatly reduced and the adsorption capacity of the C_{60} molecules will revert to the unheated state. So, pre-annealing will not help to produce Cobalt-C_{60} clusters.

At the same time, there is a problem that needs to be resolved. In Section 5.3.1, the annealing temperature is chosen as an approximation. Although the data in Table 5.2 indicates that 80°C is the peak of the average height of the cobalt clusters, it is impossible to say that 80°C is the theoretical optimum. So, the optimum

pre-annealing temperature for the formation of Cobalt-C_{60} clusters is also a matter of experimental investigation. The exact temperature range is difficult to predict without experimentation. However, a general prediction can be made based on the current experimental results and some literatures. 500 K and 550 K is the cut-off point for cluster sink rates in the study by S. Padovani et al [6]. What's more, according to the experiments on the effect of annealing on cobalt clusters in Chapter 5, cobalt clusters pre-annealed at 80°C have the highest average cluster height. It can therefore be expected that the optimum pre-annealing temperature (if it exists) should be in the neighborhood of 80°C, and a wide search in the range below 200°C is required to confirm this.

The experiment can therefore be designed as follows.

Firstly, similar to the experimental procedure in Chapter 4, an Au (111) surface substrate A is prepared and a certain number of cobalt atoms are deposited on it (based on previous experiments, a coverage of around 0.2 ML of cobalt atoms ensures that the cobalt clusters are in a more even bilateral structure), followed by the deposition of C_{60} molecules with 2 times the cobalt coverage. Based on experimental experience, the coverage of the cobalt:C_{60} 1:2 contributes to the complete adsorption of C_{60} molecules by the cobalt clusters. It is now known that Cobalt-C_{60} clusters form on the surface of the sample annealed at 320°C for 30 min. Then for annealing temperatures below 320°C, there will be a threshold temperature. At the temperature below the threshold temperature, annealing will not result in significant changes to the surface structure of the sample, while annealing temperatures above that will result in Cobalt-C_{60} cluster formation. In the experiment, sample A would be repeatedly annealed at increasing temperatures in 20°C intervals and the surface structure would be observed at room temperature using STM. Then at a certain temperature point T_C, the appearance of Cobalt-C_{60} clusters will be observed. The temperature T_C can be considered as the threshold temperature of the C_{60} adsorption on cobalt clusters.

Afterwards, prepare an identical Au (111) substrate B and the cobalt atoms with same coverage are deposited on it. For sample B, a 30 minutes annealing at T_C is then performed, followed by the deposition of the same number of C_{60} molecules as A at room temperature. Then under STM scanning, two different situations may occur: (1) Sample B is identical to A with the Cobalt-C_{60} clusters appearing on both of them. (2) No Cobalt-C_{60} clusters are observed on B.

If case (2) is observed, it would indicate that the adsorption of C_{60} by the cobalt cluster only occur at high temperature, meaning that the dynamic thermal motion model of the cobalt cluster to adsorb C_{60} is confirmed. Whereas if case (1) had been observed, it would indicate that as soon as the cobalt cluster ever reaches the threshold temperature T_C, its adsorption capacity on the C_{60} molecule would be substantially increased, and then the static self-refined model of C_{60} adsorption would be confirmed.

In fact, it would probably have been simpler if the C_{60} deposition had been carried out while the sample was being heated. However, considering the design of the STM used in this experiment, it is not feasible to deposit C_{60} while heating the sample. Therefore, this more complex experimental design would have to be used if the experiments were to be continued under the same conditions as in this thesis.

6.3.2 The C_{60} Protection of Cobalt Custers from Thermal Sinking

In the model of Cobalt-C_{60} cluster generation presented in Chapter 5, it's mentioned that the wrapping of the C_{60} molecules has the effect of protecting the sinking of the cobalt clusters at high temperature. It seems to be easily proved. A comparison can be made simply by comparing the change in coverage of cobalt clusters before and after annealing with the change in coverage of pure cobalt clusters without C_{60} molecules. In specific experiments, however, difficulties exist. The annealed cobalt is covered by

C_{60} molecules and it is difficult to image the cobalt atoms by STM scanning only. In practice, therefore, the statistics for the Cobalt-C_{60} cluster should be more intuitive and accurate than for the cobalt atoms.

The experiment can therefore be designed as follows.

Two identical Au (111) substrates, A and B, are prepared and deposited with the same coverage of cobalt atoms, followed by the deposition of C_{60} molecules with 2 times the cobalt coverage on both. For sample A, annealing is first carried out at T_C for 30 min and then again at 320°C for 30 min after cooling down to room temperature. For sample B, on the other hand, a one-time annealing at 320°C for 30 min is carried out directly. If the C_{60} molecules did protect the cobalt clusters from sinking, for sample A, there will have more cobalt clusters protected by the wrapped C_{60}. For sample B, the sinking of the cobalt clusters and the diffusion of C_{60} are simultaneous. Therefore, some of the cobalt clusters will sink into the gold surface before being wrapped by C_{60}. Thus, less cobalt clusters will be left on the surface to form the Cobalt-C_{60} clusters. In other words, by comparing the STM images of sample A with those of sample B, if the percentage of Cobalt-C_{60} clusters forming at the elbow sites is the same, the C_{60} molecules have no particular protective effect on the sinking of cobalt clusters at high temperature. Conversely, if the Cobalt-C_{60} clusters' formation rate at the elbow sites of sample A is significantly higher than that of sample B, it can be assumed that the wrapping of C_{60} molecules has a protective effect on the sinking of cobalt clusters at high temperature.

There is also one possibility beyond this that the cobalt clusters are not completely sunk into the gold surface, but partially sunk, under the wrapping of the C_{60} molecules. In this case, the percentage of cobalt-C_{60} clusters will not change significantly. For this possibility, considering the absence of C_{60} in the case of annealing at 340 °C can basically make the cobalt clusters completely sunk, only partially sunk cobalt clusters

itself is an indication of the protective effect of C_{60} molecules on the cobalt clusters. On the other hand, the change in the average height of the cobalt clusters can be monitored to determine whether partial sinking of the clusters has occurred.

6.3.3 The Presence or Absence of Cobalt-Carbon bonds

Another important part of the Cobalt-C_{60} cluster generation model that remains to be resolved is whether a cobalt-carbon bond is formed. If a Co-C bond does exist, a further question is at which stage it forms. In Section 5.3.4, a rapid increasing in the number of C_{60} molecules adsorbed by cobalt clusters is found from 320°C to 380°C. In the discussion in Section 5.4.2, this phenomenon was attributed to the formation of cobalt-carbon bonds. Based on the known experimental data, this assumption should be reasonable, but not definitive. If considered from an ideal perspective, electronic state changes in Cobalt-C_{60} bond by STM scanning should be the optimal choice, as has been done in some literatures [7][8]. Unfortunately, for the VT-STM used, the resolution of it is unattainable. Therefore, experiments must be designed from other perspectives

For the difference between van der Waals force interactions and cobalt-carbon bonds between cobalt and C_{60} molecules, the most significant difference is in strength between the two interactions [9][10]. Intuitively, if T_0 is the desorption temperature of C_{60} molecule adsorbed by cobalt cluster under van der Waals forces, the desorption temperature must be greater than T_0 for a C_{60} molecule that has formed a Co-C bond.

Therefore, we can design an experiment as follows.

Two identical Au (111) substrates A and B are prepared and deposited with the same coverage of cobalt atoms, followed by the deposition of C_{60} molecules with 2 times the cobalt coverage on both. Sample A will be annealed at T_C which is the threshold temperature mentioned in Section 6.3.1 and sample B will be annealed at 320°C.

Afterwards, scan the sample A and B with temperatures continuously increasing during scanning using the variable temperature in-situ scanning function of the VT-STM. Increasing the temperature will increase the rate of thermal motion. So that, in scanning of the VT-STM, a continuous movement of the Cobalt-C_{60} cluster should be observed, similar to that mentioned in this article by Q.GUO [11]. Then if the cobalt atoms are bound to the C_{60} molecules differently between samples A and B, the C_{60} diffusion and creep should be observed on sample A but not on B at a certain temperature. If there is indeed a temperature threshold for the cobalt-carbon bond formation, the creep of C_{60} on sample A will disappear when the scanning temperature is increased to this temperature. This phenomenon, contrary to the intuition that thermal motion becomes more active at higher temperature, would be evidence for the existence of cobalt-carbon bonds.

However, it is also important to note that unlike in-situ scanning at low temperatures, in-situ scanning at high temperatures is much more difficult to achieve, and based on the stronger thermal motion it may be difficult to obtain any stable and clear images. Therefore, it may be more feasible to resort to other experimental equipment rather than STM. For determining the bonding pattern between cobalt and C_{60} and whether C_{60} cage is opened, using of XPS or Raman spectroscopy might be a reasonable approach.

6.3.4 Discussion of Cobalt Cluster Migration

In Section 5.3.4, cobalt clusters that move away from elbow sites are suspected to be observed. In response, in Section 5.4.4, two possible explanations are given for this: (1) The cobalt clusters that sink into the gold surface diffuse within the gold crystal interface. (2) The surface stress imbalance caused by the sinking of cobalt clusters leads to a new reconstruction.

To discuss the cause of those structures, the first thing to confirm is whether the

structures are cobalt clusters. Therefore, a repeated experiment on a cleaner Au (111) surface is required. A piece of Au (111) sample with only cobalt atoms deposited needs to be annealed at 380°C for 30 min. It's expected to observe similar structures on the annealed sample surface using STM scanning. It should be noted that the sinking of the cobalt clusters at 380°C annealing is already quite pronounced. So, the cobalt coverage of the sample should be large enough to ensure that a sufficient number of cobalt clusters remain on the surface after annealing, which is slightly larger than the 0.2 ML sample in Chapter 5.

So, if assume that these structures are really cobalt clusters, the method used to determine the cause of cobalt cluster diffusion should be selected. Considering the two causes of cobalt clusters leaving elbow sites mentioned above, using the heated in-situ scanning function of the VT-STM should be effective. By continuously scanning the same area while heating the sample, it is possible to distinguish between migration of cobalt clusters away from elbow sites and a change in the surface reconstruction structure.

Similarly, as discussed in section 6.3., such in situ scanning is likely to be difficult to achieve. Perhaps using the LEED technique, observing the top few layers of the whole sample rather than just the clusters above the surface would be helpful in understanding the phenomenon. But the more likely result is that for single cobalt clusters, this diffusion is not reproducible. These structures are not simply diffused cobalt clusters, but rather a combination of cobalt and C_{60} molecules. In this case, further experiment design is required. In such cases, the results cannot simply be predicted and further judgements must be made based on the results of subsequent experiments.

6.4 Summary

In this chapter, some of the remaining issues of the Cobalt-C_{60} cluster self-assembly

model presented in the previous chapters are discussed: (1) Whether the adsorption capacity improvement of the clusters by annealing can be preserved after cooling down? (2) Whether the C_{60} molecules wrapping cobalt clusters protect the cobalt clusters from thermal sinking? (3) Whether the double segmented adsorption of cobalt clusters on C_{60} exists and whether Co-C bonds are formed in the Cobalt-C_{60} clusters? (4) Whether there is migration behavior of the cobalt cluster away from elbow sites? To deal with these questions, a series of validation experiments are designed based on existing experimental conditions and predicted possible experimental results.

References

[1] Hansen, P. L., Fallon, P. J., & Krätschmer, W. (1991). An EELS study of fullerite—C60/C70. *Chemical physics letters*, *181*(4), 367-372.

[2] Lavrentiev, V., Naramoto, H., Abe, H., Yamamoto, S., Narumi, K., & Sakai, S. (2005). Chemically driven microstructure evolution in cobalt–fullerene mixed system. *Fullerenes, Nanotubes and Carbon Nanostructures*, *12*(1-2), 519-528.

[3] GE, R. (1974). Adsorption and surface alloying of lead monolayers on (111) and (110) faces of gold.

[4] Pai, W. W., Jeng, H. T., Cheng, C. M., Lin, C. H., Xiao, X., Zhao, A., ... & Tsuei, K. D. (2010). Optimal electron doping of a C 60 monolayer on Cu (111) via interface reconstruction. *Physical review letters, 104*(3), 036103.

[5] Tang, L., Zhang, X., Guo, Q., Wu, Y. N., Wang, L. L., & Cheng, H. P. (2010). Two bonding configurations for individually adsorbed C 60 molecules on Au (111). *Physical Review B, 82*(12), 125414.

[6] Padovani, S., Scheurer, F., & Bucher, J. P. (1999). Burrowing self-organized cobalt clusters into a gold substrate. *EPL (Europhysics Letters), 45*(3), 327.

[7] Rossel, F., Pivetta, M., Patthey, F., Ćavar, E., Seitsonen, A. P., & Schneider, W. D. (2011). Growth and characterization of fullerene nanocrystals on NaCl/Au (111). *Physical Review B, 84*(7), 075426.

[8] Kollamana, J., Wei, Z., Laux, M., Stöckl, J., Stadtmüller, B., Cinchetti, M., & Aeschlimann, M. (2016). Scanning tunneling microscopy study of ordered C_{60} submonolayer films on Co/Au (111). *The Journal of Physical Chemistry C, 120*(14), 7568-7574.

[9] Yang, P., Li, D., Repain, V., Chacon, C., Girard, Y., Rousset, S., ... & Lagoute, J. (2015). C_{60} as an Atom Trap to Capture Co Adatoms. *The Journal of Physical Chemistry C, 119*(12), 6873-6879.

[10] Li, G., Zhang, F. F., Chen, H., Yin, H. F., Chen, H. L., & Zhang, S. Y. (2002). Determination of Co–C bond dissociation energies for organocobalt complexes related to coenzyme B12 using photoacoustic calorimetry. *Journal of the Chemical Society, Dalton Transactions*, (1), 105-110.

[11] Xie, Y. C., Tang, L., & Guo, Q. (2013). Cooperative assembly of magic number C 60-Au complexes. *Physical Review Letters, 111*(18), 186101.

Chapter 7. Summary and Future Work

In this thesis, I present my research work on self-assembled clusters of Cobalt-C_{60} on Au (111) surfaces. Self-assembled Au-C_{60} magic number clusters on Au (111) surfaces were successfully manufactured in the work at the NPRL laboratory of the University of Birmingham in 2013. However, for this work, there are two key issues for Au-C_{60} magic number clusters. (1) The STM technique is unable to image the interfacial structure and there is a lack of direct means to observe the structure of gold clusters covered by C_{60}. (2) The chemical stability of gold makes it difficult to expect further structure evolution of Au-C_{60} clusters. In response to these concerns, the further experiments plan to use cobalt as a substitute for gold in the manufacturing of Cobalt-C_{60} clusters. Based on the fact that cobalt is more reactive than gold and the large number of examples of Cobalt-C_{60} complexes in the experiments, the formation of Cobalt-C_{60} clusters was thought to be easy in the extreme of the experimental design. However, the experimental results were the opposite of what was expected.

If C_{60} molecules are deposited on the Au (111) surface with C_{60} molecules, the C_{60} molecules are not adsorbed by the cobalt clusters but instead arranging in large islands. The small cobalt clusters show a low adsorption rate of C_{60}, while only the large clusters adsorb single C_{60} molecules. Only after annealing the sample at 320°C for 30 min, the large C_{60} islands disappear and Cobalt-C_{60} clusters are observed. Based on the experimental phenomena observed above, three explanations have been proposed. The first explanation is that the nucleation of cobalt clusters causes the local reconstruction of the gold surface, forming a ring of energy barriers to resist C_{60} adsorption. At high temperature, C_{60} molecules can cross the energy barriers to be adsorbed by the cobalt clusters. The second explanation is that, due to the 14% lattice mismatch between cobalt and gold, the cobalt clusters on the gold surface are irregular. This irregularity leads to inefficient contact between the C_{60} molecules and the cobalt clusters, resulting in low interactions to adsorb C_{60} molecules. At high temperature, the thermal motion of the cobalt clusters is enhanced, and the interaction strength is

increased by the self-refinement of the C_{60} molecules to adsorb C_{60} molecules. The third explanation is that the cobalt clusters are polluted by gas molecules in the vacuum chamber. At high temperature, the gas desorbs and the cobalt cluster regains its reactivity towards C_{60}.

In order to determine these three different explanations and to further investigate the mechanism of cobalt-C_{60} cluster formation, further experiments are designed. The Au (111) sample with cobalt clusters is first annealed at 320°C, while the C_{60} molecules are then deposited. The sample is annealed with a second time. The experimental results are that swapping the annealing order will lead to different results. On the pre-annealed samples, the C_{60} molecules still form large islands and most of the cobalt clusters are still bare. However, the small cobalt clusters can be fully wrapped by C_{60} islands after pre-annealing compared to the unannealed Cobalt-C_{60} sample. After the re-annealing of the sample at 320°C or even higher, the cobalt-C_{60} clusters still do not extensively appear, but the average number of C_{60} adsorbed by the cobalt clusters gradually increase with the annealing temperature. Bare cobalt clusters after pre-annealing reject the gas adsorption model, as the very short time interval between pre-annealing and C_{60} deposition dictates that secondary pollution does not occur. What's more, the fully wrapping of small cobalt clusters by C_{60} after pre-annealing rejects the energy barrier model. This is due to the fact that the cobalt clusters will gradually sink into the gold surface at high temperature and pre-annealing will only enhance this barrier rather than weaken it. Therefore, the irregular cobalt cluster model due to lattice mismatch would be the correct explanation. The inability to form Cobalt-C_{60} clusters on pre-annealed samples is due to the sinking of the cobalt clusters after annealing. The gradual increase in the average C_{60} adsorption amounts of cobalt clusters with annealing temperature is explained by the Co-C bond formation rate increase with temperature.

In the case of the formation of Cobalt-C_{60} clusters, there are still a number of issues

that are left to be resolved. However, due to the finite experimental time available for PhD studies, experiments to validate these issues could not be carried out. So, in Chapter 6, I just give the experimental designs of these issues and make predictions about the results of the experiment. These questions are: (1) Whether the enhanced C_{60} adsorption capacity of the cobalt clusters brought about by heating can be remained after cooling down? For the C_{60} adsorption by cobalt clusters, whether C_{60} adsorption at room temperature can be achieved by self-refined Co clusters? (2) Whether there is protection of the cobalt cluster by the C_{60} molecules from thermal sinking. To what extent does this protection work? (3) Is the cobalt-carbon bond formed in C60 adsorption? Whether there is a double segmented adsorption of van der Waals bonds and chemical bonds? (4) How to explain the migration of cobalt clusters from the elbow sites.

The first part of the future work to be completed is to answer those questions presented in Chapter 6. The threshold temperature for C_{60} adsorption by cobalt clusters, and whether C_{60} protects the clusters from thermal precipitation, are the most important parts that should be done immediately and can be done directly using STM. Secondly, the bonding between cobalt clusters and C_{60} is a question that must be answered for the study of cobalt-C_{60} clusters. Based on STM, XPS and Raman spectroscopy studies should be carried out. Afterwards, the preparation of self-assembly magic-number-like cobalt-C_{60} clusters, which was the original aim of this experiment, remains a worthwhile topic. Based on the investigation of the mechanism of adsorption of C_{60} molecules by cobalt clusters in this thesis, the study of self-assembly magic-number-like cobalt-C_{60} clusters will be further advanced. Finally, if all goes well, the catalytic study of C_{60} by cobalt clusters on gold surfaces should also be carried out. The characterization of new carbon nanostructures based on STM will be a breakthrough. Also, combining such carbon nanostructures with surface self-assembly techniques may lead to some valuable breakthroughs in the field of semiconductor materials.